



**University of
Zurich**^{UZH}

Understanding the recent dynamics of glacier lake outburst floods at Baralmos Glacier, Tajikistan

GEO 511 Master's Thesis

Author

Varvara Kharlamova
23-742-406

Supervised by

Dr. Evan Miles
Dr. Simon Allen

Faculty representative

Prof. Dr. Christian Huggel

31.01.2025

Department of Geography, University of Zurich

Acknowledgments

This Master's thesis would not have been possible without many people's guidance, support, and encouragement.

First and foremost, I would like to express my gratitude to my supervisor, Dr. Evan S. Miles, for not only support, insightful feedback, and constant motivation throughout the research process but also for proposing this fascinating topic and providing data. I also thank Prof. Christian Huggel and Dr. Simon Allen for their feedback and thoughtful insights.

I am especially thankful to the Department of Geography of the University of Zurich for providing the necessary facilities and resources and their supportive academic environment, which immensely helped me during this work. I extend my gratitude to the PAMIR and GLOFCA projects for providing crucial data and materials that were integral to the success of this research.

Furthermore, I would like to thank Roman Menialshchikov for his support, especially in reviewing countless lines of code, and for always being by my side throughout this journey. I also thank Julia van Leeuwen (UZH) and Valentina Lisak for proofreading my thesis.

To my family and friends, your unwavering support has been my anchor during the challenging times of studying and living abroad in Switzerland. Your motivational words of encouragement, understanding, and belief in my abilities have strengthened me and kept me motivated, even when the journey felt overwhelming.

Abstract

Glacial lake outburst floods (GLOFs) represent an extreme threat to high mountain areas and their infrastructure, especially in Central Asia, where glacier retreat is accelerated and new lakes are formed. This research examines the recent history of GLOFs from Baralmos glacier in Tajikistan, concentrating on its supraglacial pond systems. This research pays great attention to the high-resolution PlanetScope imagery and Landsat data, which improves the assessment accuracy for seasonal and yearly dynamics of pond area and volume changes.

Using the NDWI and thresholding techniques, the study identifies patterns of pond evolution and drainage, highlighting critical outburst events. Water scale area-volume relationships were utilized to estimate the amount of water, which can help to define the possible flood size. Moreover, the Pleiades stereo DEMs will be used to examine the channel erosion and deposition of the sediments after outburst events.

Key findings reveal substantial increases in pond areas and volumes from 2017 to 2024. Significant drainage events, particularly during mid-to-late summer, were identified as critical periods for potential GLOF occurrence. The research highlights complex hydrological interconnections between supraglacial ponds during some drainage events, emphasizing the need for advanced monitoring to predict these hazards. Additionally, geomorphological analysis of DEMs reveals extensive erosion and sediment deposition along drainage channels, underscoring the destructive downstream impacts of outburst floods. The long-term effects of glacier retreat and surges on supraglacial pond dynamics are demonstrated by contrasting historical and recent period data. Even though the 1998 surge event drastically decreased the amount of water that could be stored on the glacier surface, the glacier's subsequent rebound and the emergence of new ponds show its increased GLOF potential.

Table of Contents

List of Abbreviations	iv
List of Figures	v
List of Tables	vii
1. Introduction	1
1.1. Research context and relevance	1
1.2. Objectives.....	2
2. Scientific background	3
2.1. GLOFs characteristics and lake types	3
2.2. Factors influencing glacial lake formation.....	7
2.3. Distribution and frequency of GLOFs.....	8
2.4. Socio-economic impacts of GLOFs	11
3. Study area	13
3.1. Location and glaciation characteristics	13
3.2. Weather and climate.....	15
4. Data and Methods	18
4.1. Approach.....	18
4.2. Remote sensing data.....	19
4.2.1. Satellite images	19
4.2.2. DEM.....	20
4.3. NDWI.....	20
4.4. Area and volume estimations of Baralmos ponds.....	22
4.5. Interconnectivity analysis.....	23
4.6. DEM analysis	24
5. Results	27
5.1. Temporal dynamics of supraglacial ponds	27
5.1.1. Seasonal and multi-year dynamics for the recent period.....	27
5.1.2. Historical period.....	34
5.1.3. Kyzylsu glacier.....	35
5.1.4. Interconnectivity of pond areas changes	36
5.2. Drainage events and geomorphological changes	38
6. Discussion	44
7. Conclusion	48
8. References	50
9. Appendices	59
Personal declaration	68

List of Abbreviations

AWS	Automatic Weather Station
DEM	Digital Elevation Model
EWS	Early Warning System
GLOF	Glacial Lake Outburst Flood
GLOFCA	Glacier Lake Outburst Floods in Central Asia
HMA	High Mountain Asia
IPCC	Intergovernmental Panel On Climate Change
LIA	Little Ice Age
NDWI	Normalized Difference Water Index
RGI	Randolph Glacier Inventory
UNESCO	United Nations Educational, Scientific and Cultural Organization
UZH	University of Zurich

List of Figures

Figure 1. Supraglacial ponds on Baralmos glacier, August 2024 (photo by Evan S. Miles).	4
Figure 2. Representation of a glacial lake outburst flood and its downstream impacts (Adopted from Mergili et al., 2011).....	4
Figure 3. Schematic representation of a hazardous moraine-dammed glacial lake, illustrating potential triggers, conditioning factors, and key stages of a GLOF event. Stages of GLOF include: (1) displacement or seiche waves propagating in the lake and/or piping through the dam; (2) breach creation and commencement; and (3) the propagation of the resulting flood wave or waves down-valley (Adopted from Westoby et al., 2014).	5
Figure 4. Post-disaster landscape and flow pathways, Kedarnath catastrophe (2013). (1) The main component turned south to follow the Mandakini River directly towards Kedarnath; (2) A second large component (Allen et al., 2016).....	6
Figure 5. The mass balance trend in the Pamir region is represented as cumulative mass balance (m w.e.) and as standardized values (Khromova et al., 2006).....	8
Figure 6. The annual number of articles on GLOFs published in the WOS Core Collection database (Adopted from Emmer, 2018).....	9
Figure 7. Spatial distribution of GLOF danger in HMA at basin scale from high (red) to low (blue) risk (Adopted from Taylor et al., 2023).	10
Figure 8. Consequences of an outburst flood and mudflow from Baralmos Glacier, July 2023. The image shows the geomorphological impacts downstream, including sediment deposition and flooding of the area, including automobile road.....	10
Figure 9. Closure of the Surkhob riverbed after the event (left) and the destroyed international road in the Lyakhsh region (right) (photos from Baralmos field report 2023).....	11
Figure 10. Baralmos Glacier. Photo from the study site, August 2024 (photo by Evan S. Miles).....	13
Figure 11. Kyzylsu glacier viewed from the eastern side, 2023 (photo by Jason Klimatsas).	13
Figure 12. Map of study site in Tajikistan with the indication of Baralmos and Kyzylsu glaciers. Glaciated areas were delineated using the RGI dataset, and the background elevation data and hillshade were derived from the SRTM DEM (USGS), upper map, and water objects were obtained from OpenStreetMap.	14
Figure 13. Moraine-covered tongue area of Baralmos glacier. Photo from the study site, August 2024 (Evan S. Miles).	15
Figure 14. Change in the average annual temperature (1970-2023) in the study area based on hourly multi-variable downscaled and bias-corrected meteorological data	16
Figure 15. Workflow for NDWI calculations. This diagram illustrates the step-by-step process for extracting water bodies from satellite imagery.	21
Figure 16. Results of NDWI analysis on Baralmos Glacier (8 th of July 2021). From left to right: (1) NDWI values, (2) NDWI histogram, (3) binary water mask generated by Otsu's threshold, and (4) the original image in true colors.	21
Figure 17. NDWI analysis with iterative refinement for Baralmos Glacier (8th of July 2021). Histogram (3) presents the distribution of NDWI values with the optimized threshold value.	22
Figure 18. The data of the Watson et al. study combined with the compiled dataset of Cook and Quincey (2015). The scatter plot shows a strong correlation between pond area and volume.	23
Figure 19. The satellite image shows the spatial locations of analyzed ponds ([1], [2], [3], and [4]) on Baralmos glacier, which can be also seen on the lake-frequency map (Figure 32).	24
Figure 20. DEM Analysis Workflow. The procedure for examining Digital Elevation Models (DEMs) in order to identify elevation variations and other geomorphological changes is described in this diagram.	24
Figure 21. Bare ground (left) and slope (right) masks. The function <code>xdem.terrain.slope</code> was used to calculate the slope from the input DEM to create the slope mask. The slope mask finds areas with slopes below a specified threshold (30°) to guarantee the stability of the terrain; the bare ground mask was applied to isolate	

non-glacierized stable terrain. These masks were employed to delineate further stable terrain for accurate and precise coregistration of DEMs and detection of changes.....25

Figure 22. A stable terrain mask was generated in the Python environment. The mask identifies unstable regions (black areas) and stable terrain (white areas) based on the above mentioned masks.26

Figure 23. Histogram of elevation differences (before and after correction). The blue histogram captures the differences in elevations before coregistration and bias correction, while the green histogram represents the differences post-coregistration. The median elevation difference and NMAD values are presented for both cases, showing the improvement achieved after coregistration.26

Figure 24. Total pond areas over time (2017–2024) for Baralmos glacier.27

Figure 25. Total estimated pond volumes over time (2017–2024) for Baralmos glacier based on a formula from Watson et al., 2017.28

Figure 26. Total pond areas on Baralmos Glacier from 2017 to 2024, plotted by the day of the year. Each line represents a different year28

Figure 27. Total pond areas over time (2017).29

Figure 28. Total estimated volume over time (2021) based on a formula from Watson et al., 2017.29

Figure 29. Total pond areas over time (2022).30

Figure 30. Sequence of NDWI and true-color imagery illustrating the 2022 drainage event on Baralmos Glacier. The images show that the pond areas have decreased, especially in the main pond. Pixel resolution: 3x3 meters per pixel.30

Figure 31. Total pond areas over time (2023).31

Figure 32. Sequence of NDWI and true-color imagery illustrating the 2023 drainage event on Baralmos Glacier. The images show how the pond areas changed between July 19 and July 22, 2023. The NDWI imagery shows a noticeable decrease in these ponds' area by July 22. Pixel resolution: 3x3 meters per pixel.31

Figure 33. Total pond volumes over time (2024) based on a formula from Watson et al., 2017.32

Figure 34. Lake-frequency map across the Baralmos glacier (2017-2024) with locations of further analyzed ponds ([1], [2], [3], and [4]). On leeward slopes, a few outlier pixels resemble windblown snow, which, however, don't make a difference.32

Figure 35. Lake-frequency maps across the Baralmos glacier for 2017 and 2024.33

Figure 36. Long-term evolution of supraglacial pond areas on Baralmos glacier based on Landsat and PlanetScope data.34

Figure 37. Baralmos glacier before **(1 and 2)** and after **(3)** the surge. The surge event lead to significant drainage and disappearance of main water bodies by September 1998. Pixel resolution: 30x30 meters per pixel.34

Figure 38. Sequence of NDWI imagery illustrating the 2023 drainage event, Kyzylsu glacier. The main supraglacial pond can be detected on the 11th of June, but it disappears by June 19. Pixel resolution: 3x3 meters per pixel.35

Figure 39. Separate pond areas and total pond area over time (2021). The black line represents the total area.37

Figure 40. Separate pond areas and total pond area over time (2022). The black line represents the total area.38

Figure 41. Elevation difference picture obtained after DEM-correction, based on Pleiades DEMs for 2022-2023. **(1)** main drainage channel from pond [1]; **(2)** channel further down the valley, where we can see elevation differences39

Figure 42. Elevation differences along the drainage channel down the valley between 2022 and 2023, showing areas of erosion (blue) and deposition (red) derived from DEM analysis.39

Figure 43. PlanetScope satellite images in pseudo-colors before (22.07.2022) and after (26.07.2022) the outburst event.40

Figure 44. PlanetScope satellite images in pseudo-colors before (19.07.2023) and after (22.07.2023) the outburst event. (1) Flooded mudflow cone and new material deposition; (2) flooded Surkhob River.	40
Figure 45. Debris flow deposition area (Baralmos Field Report, 2023), which can also be identified on satellite images.	41
Figure 46. PlanetScope satellite images in pseudo-colors before (27.06.2024) and after (03.07.2024) the outburst event. (1) An increased water flow through the channel.	42
Figure 47. PlanetScope satellite images (natural colors) in 2017 and 2024. (1) and (2) channel slopes erosion; (3) sediment deposition	42
Figure 48. PlanetScope satellite images (natural colors) in 2017 and 2024. (1) channel slope erosion; (2) sediment deposition.	43
Figure 49. Total pond volumes over time (2017) based on a formula from Watson et al., 2017.	63
Figure 50. Total pond areas over time (2018)	64
Figure 51. Total pond volumes over time (2018) based on a formula from Watson et al., 2017.	64
Figure 52. Total pond areas over time (2019)	64
Figure 53. Total pond volumes over time (2019) based on a formula from Watson et al., 2017.	65
Figure 54. Total pond areas over time (2020)	65
Figure 55. Total pond volumes over time (2020) based on a formula from Watson et al., 2017.	65
Figure 56. Total pond areas over time (2021)	66
Figure 57. Total pond volumes over time (2022) based on a formula from Watson et al., 2017.	66
Figure 58. Total pond volumes over time (2023) based on a formula from Watson et al., 2017.	66
Figure 59. Total pond areas over time (2024)	67

List of Tables

Table 1. Satellite data summary	19
Table 2. Total area and volume estimates for supraglacial ponds on Baralmos glacier (2017-2024).....	59
Table 3. Total area and volume estimates for supraglacial ponds on Kyzylsu glacier (2023-2024).....	62
Table 4. Area estimates for supraglacial ponds on Baralmos glacier for historical period	63

1. Introduction

1.1. Research context and relevance

Global climate change has a significant impact on the highlands and contributes to the increasing frequency and intensity of the most dangerous natural processes (Bajracharya and Mool, 2009; Hock et al., 2022). One of the clearest signs of this is the worldwide retreating of glaciers, which is regarded as a direct result of increased temperatures (Huggel et al., 2020). Active degradation of mountain glaciation is currently observed in Central Asia (Barandun et al., 2020; Hock et al., 2022). This leads to a violation of the stability of moraine-glacial complexes and is one of the leading factors contributing to the formation of glacial genesis debris flows (Bolch et al., 2008; Zaginaev et al., 2019). Furthermore, climate change and the concomitant retreat of glaciers have caused the development and growth of glacial lakes in mountainous regions of the world (Bolch et al., 2012; Zheng et al., 2019). A study by Furian et al. (2021) suggests that the majority of future lakes in High Mountain Asia (HMA) will form in the still heavily glaciated regions of the Pamir, Tien Shan, and Karakoram.

Lake outbursts are difficult to predict, yet they can lead to significant destruction, as debris flows have the potential to cause extensive damage further down the valleys. This is particularly concerning, given that, about 10% (671 million people) of the world's population lived in high-altitude regions in 2010. By 2050, this number is expected to grow even further, with estimates ranging between 736 and 844 million people (Frey et al., 2010). This population growth highlights the growing risk posed by natural disasters caused by climate change to human settlements and infrastructure in mountainous areas.

About 90% of Tajikistan's territory is mountainous, with elevations ranging from a few hundred meters to 6000 to 7000 meters above sea level. The country suffers significantly from natural disasters such as landslides, earthquakes, debris flows, and avalanches (Zafar and Uchimura, 2023). Among all of these, debris flows are one of the most disastrous and costly. Every year, they cause extensive damage to miles of highways, bridges, buildings, and other infrastructure in a very short period. As of 2003, Tajikistan has 1,449 lakes with a total area of 716 km². Approximately 80% of them are located in mountainous regions at elevations of 2,500 to 5,000 meters above sea level (Shafiev, 2018).

Baralmos Glacier in Tajikistan has repeatedly triggered outburst floods in recent years, resulting in significant damage to essential transportation infrastructure. Unlike typical discharge events

caused by a large proglacial lake, these floods originate from water stored within the glacier itself (englacial) and from supraglacial ponds on the glacier's surface (Miles et al., 2018a; Narama et al., 2018, 2017). Although these ponds are small, they can develop quickly over a few weeks or months as seasonal snow melts, posing a considerable risk despite their size. Even though glacier outburst floods originating from supraglacial and englacial sources are smaller in magnitude than those from subglacial lakes, they can still cause significant damage to infrastructure (Rounce et al., 2017).

1.2. Objectives

The objective of this Master's Thesis is to investigate the recent history and dynamics of outburst floods originating from the Baralmos Glacier. Due to the small size and rapid evolution of the Baralmos ponds, monitoring and early hazard identification are particularly challenging using traditional satellite methods. To address these limitations, this study emphasizes the need for analyzing high-resolution satellite imagery, ideally supplemented with in situ observations, to better understand the recent evolution of these systems and the processes leading to outburst floods.

In accordance with the objective of this thesis, it aims to answer the following research questions:

1. What is the frequency and size of pond drainages observed in satellite imagery during the recent period (2017–2024)?
2. How do the recent surface water storage areas compare to those from the historical period (1990-present)?
3. Are there clear signs of geomorphological changes linked to pond drainage events?
4. Are changes in pond water areas for major events interconnected, or do they occur independently of one another?

By answering these questions, this research aims to contribute valuable insights into the dynamics of glacial lake outburst floods, enhancing both scientific understanding and practical approaches to hazard management.

2. Scientific background

2.1. GLOFs characteristics and lake types

Glacial lake outburst floods (GLOFs) are sudden and rapid releases of significant volumes of water from different glacier lake types (Carrivick and Tweed, 2016; Emmer et al., 2022b; Mergili et al., 2011). Glacial lakes are more sensitive to climate change and more prone to outburst floods than larger lakes or lakes further away from glaciers (Zhang et al., 2015). Ultimately, the nature and impact of a GLOF depend on various elements, such as the volume of the lake, the type of dam that holds it, as well as the nature of the drainage route.

The volume of water released during the GLOF, the direction the flood disperses to, and the population around that vicinity determine the level of damage the glacier lake outburst floods can cause (Nie et al., 2018). Lake outbursts occur rapidly, with the entire event unfolding within a very short time (Mergili and Schneider, 2011). However, other cases have demonstrated that the glacial lakes can take multiple days if not weeks, to drain completely (Daiyrov and Narama, 2021). The volume of water in the lakes, the stability of the dam, and the characteristics of the drainage pathway all determine how long a GLOF will last. For instance, slower drainage may occur when the outflow is moderated by partially blocked channels or gradual dam erosion, whereas rapid drainage is more common in cases of sudden dam failure.

A universal standard for the classification of glacial lakes does not currently exist globally (Yao et al., 2018). Different researchers or organizations have created classification systems oriented toward their research context. In the Inventory of Glaciers, Glacial Lakes and Glacial Lake Outburst Floods (Mool, 2002) it is indicated that a glacial lake is a body of water that exists in sufficient quantity and extends with a free surface inside, under, next to, and/or in front of a glacier and arises as a result of the process of glacier retreat. Glacial lakes can be situated in various positions relative to a glacier: beneath (subglacial), alongside, in front (proglacial), within (englacial), or on the surface (supraglacial) (Figure 1) (Allen et al., 2022). Typically, these lakes are held back by natural dams composed of ice, moraine (glacial debris), or bedrock. Depending on the type of dam, glacial lakes are classified into three main categories: moraine-dammed, ice-dammed, and bedrock-dammed lakes (Huggel et al., 2004). Bedrock-dammed lakes are the most stable, whereas moraine- and ice-dammed lakes are generally more susceptible to failure (Huggel et al., 2004; Jakob and Hungr, 2005).



Figure 1. Supraglacial ponds on Baralmos glacier, August 2024 (photo by Evan S. Miles).

GLOFs can evolve in different ways (Mergili et al., 2011) (Figure 2). Ice-dammed lakes can drain through various mechanisms, including the flotation of the ice dam followed by subglacial discharge, the erosion of an overflow channel on the dam's surface, ice-marginal drainage where the glacier meets the valley wall, or through the mechanical failure of the dam itself (Richardson and Reynolds, 2000). Many ice-dammed lakes follow seasonal cycles of filling and outburst with Lake Merzbacher in Tian Shan (Kyrgyzstan) being one of the most well-known examples (Xie et al., 2013).

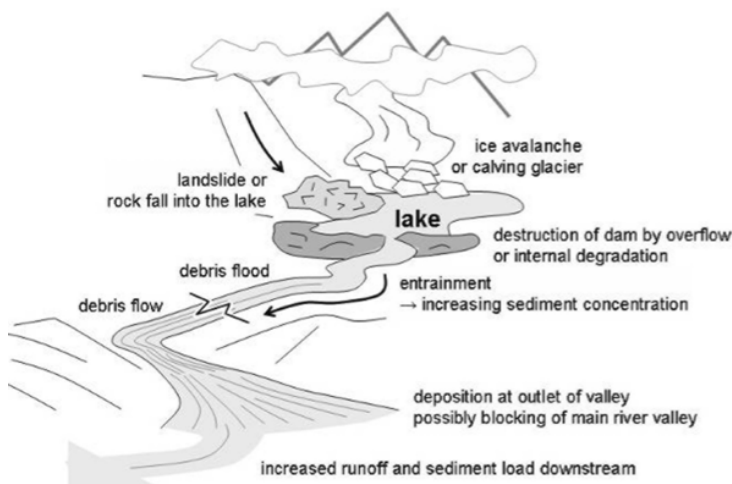


Figure 2. Representation of a glacial lake outburst flood and its downstream impacts (Adopted from Mergili et al., 2011).

Outbursts from moraine-dammed lakes (Figure 3) usually happen when the lake water overflows and erodes the moraine dam, resulting in catastrophic failure once the hydrostatic pressure surpasses the restraining lithostatic pressure (Richardson and Reynolds, 2000). Outbursts through moraine dams usually lead to floods of higher intensity (Costa and Schuster, 1987).

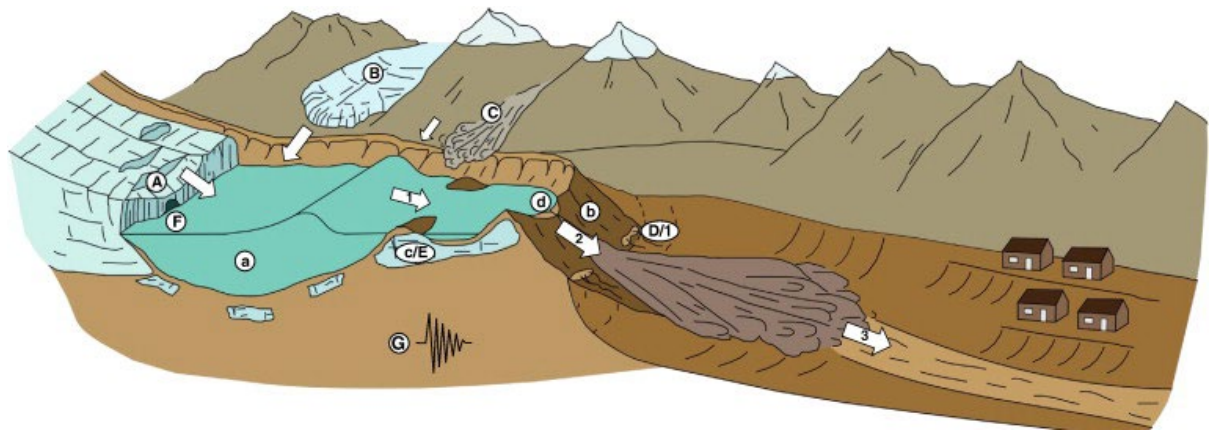


Figure 3. Schematic representation of a hazardous moraine-dammed glacial lake, illustrating potential triggers, conditioning factors, and key stages of a GLOF event. Stages of GLOF include: (1) displacement or seiche waves propagating in the lake and/or piping through the dam; (2) breach creation and commencement; and (3) the propagation of the resulting flood wave or waves down-valley (Adopted from Westoby et al., 2014).

Outburst events can also happen in bedrock-dammed lakes, where water is held above an impermeable bedrock layer. Although these lakes are considered the most stable among different types due to their resistance to dam failure, they remain vulnerable to GLOFs triggered by mass movements, such as various types of avalanches and landslides, entering the lake (Huggel et al., 2004).

We can also identify short-lived or non-stationary lakes (Erokhin et al., 2018), which form quickly and can trigger dangerous debris flows. These lakes typically develop in depressions within ice-cored moraine complexes at the glacier front (Daiyrov and Narama, 2021). Their drainage occurs through an ice tunnel or subsurface channel within the moraine complex (Narama et al., 2018), which can lead to sudden and destructive outflows.

This thesis focuses on the dynamics of water stored within supraglacial ponds. These ponds can form rapidly, often within a few weeks or months during seasonal snowmelt. They nonetheless stay small in size, limited by the local glacier surface morphology and hydrological conditions.

GLOFs can be initiated by a range of factors, often acting in combination. Different aspects concerning the ice and moraine dam stability and failure mechanisms in different areas have been discussed in many papers (Huggel et al., 2004; Richardson and Reynolds, 2000). For instance, in the Himalayas, 53% of lake outbursts were the consequence of ice avalanches whereas 8% were caused by rock avalanches, 12% were due to water infiltration of moraines that resulted in their collapse, and 4% were due to the thawing of the moraines' ice core. In comparison, the causes of 23% of outbursts remain unknown (Richardson and Reynolds, 2000). Furthermore, outbursts can be caused by extreme heat and/or liquid precipitation, the collapse of a moraine's inner slope into

the lake, changes in the subglacial and englacial drainage systems, and surface overflow across the ice.

GLOFs do not immediately turn into debris flows, since there is rarely a sufficient amount of destructible material near the riverbed (Cui et al., 2010). Specifically, poorly sorted coarse-grained sediments from moraine are rarely enough to convert the entire runoff into a debris flow. Factors that enhance the development of debris flow include steep slopes, highly dissected terrain, and the presence of abundant loose sediment in the riverbed and along valley slopes (Cui et al., 2010). In most cases these are mixtures of fine-grained material and larger debris, providing the necessary composition for debris flow mobilization (Iverson, 2012; Jakob and Hungr, 2005). Glacial and proluvial deposits are more active in debris flow formation, as they contain more dust and clay fractions, while alluvial and fluvio-glacial deposits are much more inert (Erokhin and Zaginaev, 2017). In the origin zone of most glacial debris flows in the Pamirs, vegetation is practically absent due to the high absolute heights, which also positively affects the mobility of the loose sediment cover (Huggel et al., 2004).

A geomorphological response to high-magnitude floods can include both erosion of riverbanks and the riverbed, and deposition of sediments, as well as breached dams and pre-GLOF water level evidence (Emmer, 2023; Tomczyk et al., 2020). In some cases, these floods may penetrate deeper into the valley, reshaping the landscape and creating new geomorphological features. For example, the Kedarnath catastrophe in India in 2013, in which the floodwaters followed multiple steep channels (Figure 4), demonstrated significant erosional impacts (Allen et al., 2016). The impacts of this event extended 20 km downstream along the Mandakini River.



Figure 4. Post-disaster landscape and flow pathways, Kedarnath catastrophe (2013). (1) The main component turned south to follow the Mandakini River directly towards Kedarnath; (2) A second large component (Allen et al., 2016).

2.2. Factors influencing glacial lake formation

Glacial lakes are complex dynamic elements of the glacial landscapes of Central Asia. The development of lake basins and their evolution through time is controlled by a variety of factors. Glacial lakes are deeply entangled with weather and climate, meltwater and sediment flows, and glacier and ice sheet dynamics (Carrivick and Tweed, 2013). The retreat of glaciers, mainly caused by global climate change, is one of the most significant factors contributing to glacial lake formation. An increase in air temperature stimulates a significant degradation of glaciers (Sorg et al., 2012). With increasing temperatures comes increased ice melt and glacier thinning; large over-deepened basins form and fill with meltwater (Bolch et al., 2012; Huggel et al., 2020). Seasonal variations further determine the water input into these basins, with higher meltwater discharge during the ablation season (Fujita, 2008). This has resulted in an increase in the size and number of moraine-dammed supraglacial and proglacial lake systems in recent decades (Komori, 2008; Westoby et al., 2014; Zheng et al., 2021). The study by Zheng et al. (2021) shows that the lake area in HMA has grown by 6.8% between 1990 and 2015, with moraine-dammed lakes expanding by 31.3% in the same period. It is expected that the continued growth of glacial lakes will lead to an increase in the GLOF hazard and risk (Furian et al., 2021; Zheng et al., 2021).

According to the IPCC report (Hock et al., 2022), the average surface air temperature in Central Asia has hovered at 1-2 °C for two centuries. However, the report did not contain any specific information about its temporal (for example, the time of sudden temperature changes) or spatial (for example, areas of significant increase or decrease in temperature) variations (Hu et al., 2014). In addition, spatial interpolation or extrapolation is particularly prone to errors in this region due to the small number of weather stations. Some local sources in Tajikistan report that the average annual air temperature in mountainous regions at an altitude of 1000 to 2500 meters above sea level increased by 0,3–0,5 °C, and in areas above 2500 meters above sea level, the increase was 0,2–0,4 °C (Safarov and Fazylov, 2023). Most meteorological stations in Tajikistan have recorded a positive trend in the mean annual air temperature for the period 1940–2000 (Makhmadaliev et al., 2008). In addition to rising temperatures, it is important to mention that glaciers in the HMA are more affected by the seasonality and intensity of precipitation than by changes in total annual precipitation. For instance, in regions where accumulation coincides with warming, such as in summer, rising temperatures not only accelerate melting but also increase the proportion of precipitation falling as rain rather than snow (Fujita, 2008).

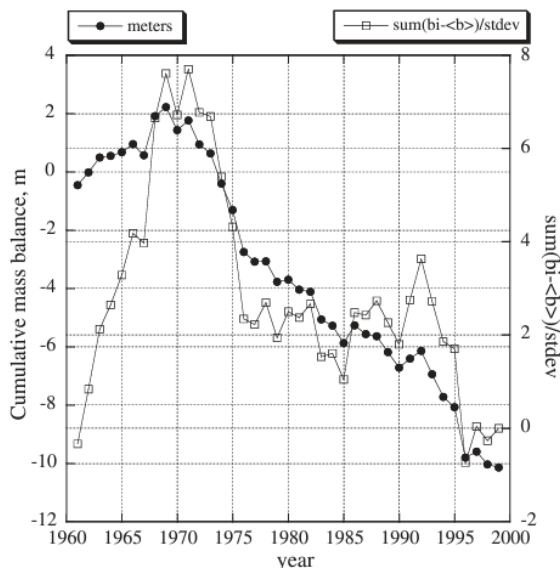


Figure 5. The mass balance trend in the Pamir region is represented as cumulative mass balance (m w.e.) and as standardized values (Khromova et al., 2006).

Several studies have documented the retreat of numerous glaciers in the Pamir region (Haritashya et al., 2009; Khromova et al., 2006). Figure 5 illustrates the mass balance trend in the Pamir region throughout 1960-2000. For the period 2000-2016, the Pamir and Pamir Alai regions exhibited a mean glacier mass balance of -0.17 m w.e. yr^{-1} (Miles et al., 2021). This glacier retreat has contributed to the formation of lakes in glacier forefields or subsiding areas on the glaciers. However, the absence of in-situ glacio-meteorological observations in various parts of the Pamir limits the ability to fully understand the regional differences in glacier mass balance and meltwater runoff patterns (Zhu et al., 2020).

2.3. Distribution and frequency of GLOFs

Mountain lake outburst floods have been documented in numerous high-altitude regions around the world, highlighting the global nature of this hazard. Events of this kind have been documented not only in the European Alps (Huggel et al., 2004, 2002) but also in the Karakoram Range (Bazai et al., 2021; Bhambri et al., 2019), the Himalayas (Nie et al., 2018; Richardson and Reynolds, 2000), and the Tian Shan mountains (Erokhin et al., 2018; Narama et al., 2018; Zaginaev et al., 2019), as well as Pamirs (Mergili et al., 2011). In North America, similar outburst floods have been recorded in the Rocky Mountains (Evans and Clague, 1994). The phenomenon is also prevalent in the Andes (Emmer et al., 2016; Mergili et al., 2020; Wilson et al., 2018), demonstrating its global reach.

Over the last decades, research activity in this area has increased (Emmer et al., 2022a), which is nicely documented by the increasing number of scientific publications. The article by Emmer (2018) proves that studies regarding the glacial lake outburst floods have acquired relevance over the past few decades (analyzed period 1979-2016) (Figure 6).

There are several studies that have investigated trends and the number of GLOFs on regional and global scales (Carrivick and Tweed, 2016; Emmer et al., 2022b; Falátková, 2016; Harrison et al., 2018; Veh et al., 2022, 2018). A study by Falátková (2016) analyzed the temporal distribution of

GLOF events in HMA and assessed their causes. The database spans a wide temporal range, from 1533 to 2012, with most recorded events occurring in the 19th and 20th centuries. A global spatial and temporal assessment of moraine-dammed GLOFs was also conducted by Harrison et al. (2018). Notably, in the Pamir and Tien Shan mountains of Central Asia, 20 events were recorded, with most occurring between the late 1960s and early 1980s. This pattern can be linked to a broader temporal trend, as from 1930 to 1970, the increased frequency of GLOFs was likely a delayed response to the warming that marked the end of the LIA (Little Ice Age) (Harrison et al., 2018).

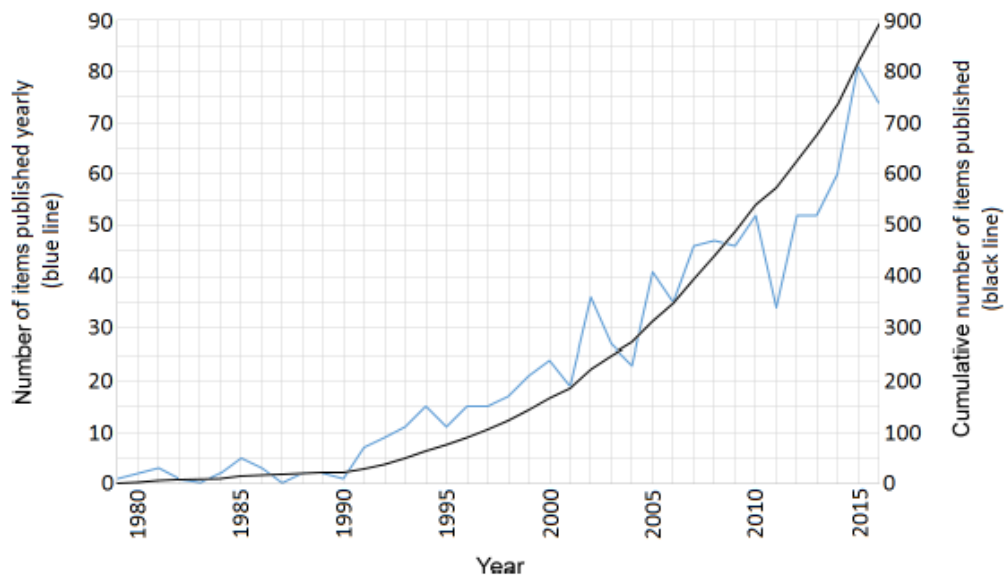


Figure 6. The annual number of articles on GLOFs published in the WOS Core Collection database (Adopted from Emmer, 2018).

High Mountain Asia, which includes some of the highest and most glaciated regions on the planet, such as the Himalayas, Karakoram, Tien Shan, and Pamir mountains, is particularly vulnerable to GLOFs. This region ranks highest globally in terms of GLOF danger (Figure 7), with ~9.3 million people exposed to potential outburst events (Taylor et al., 2023). HMA recorded the second-highest number of GLOFs events globally, surpassed only by the Pacific Northwest (Veh et al., 2022).

As mentioned earlier, Tajikistan is highly susceptible to GLOFs due to its mountainous terrain and extensive glacier coverage. The study area experiences GLOF-associated debris events each year. The consequence of these events is debris flows and flash floods that spread for tens of kilometers down the valley. For instance, in 2021, the Lyakhsh region experienced a particularly destructive debris flow caused by the outburst of a lake on the surface of the Baralmos Glacier. In 2023, five powerful debris flows were recorded: June 14, July 21, July 28, July 31, and August 7 (*Baralmos Field Report 2023*). All events were followed by the destruction of the international road in the Lyakhsh region (Figures 8 and 9).

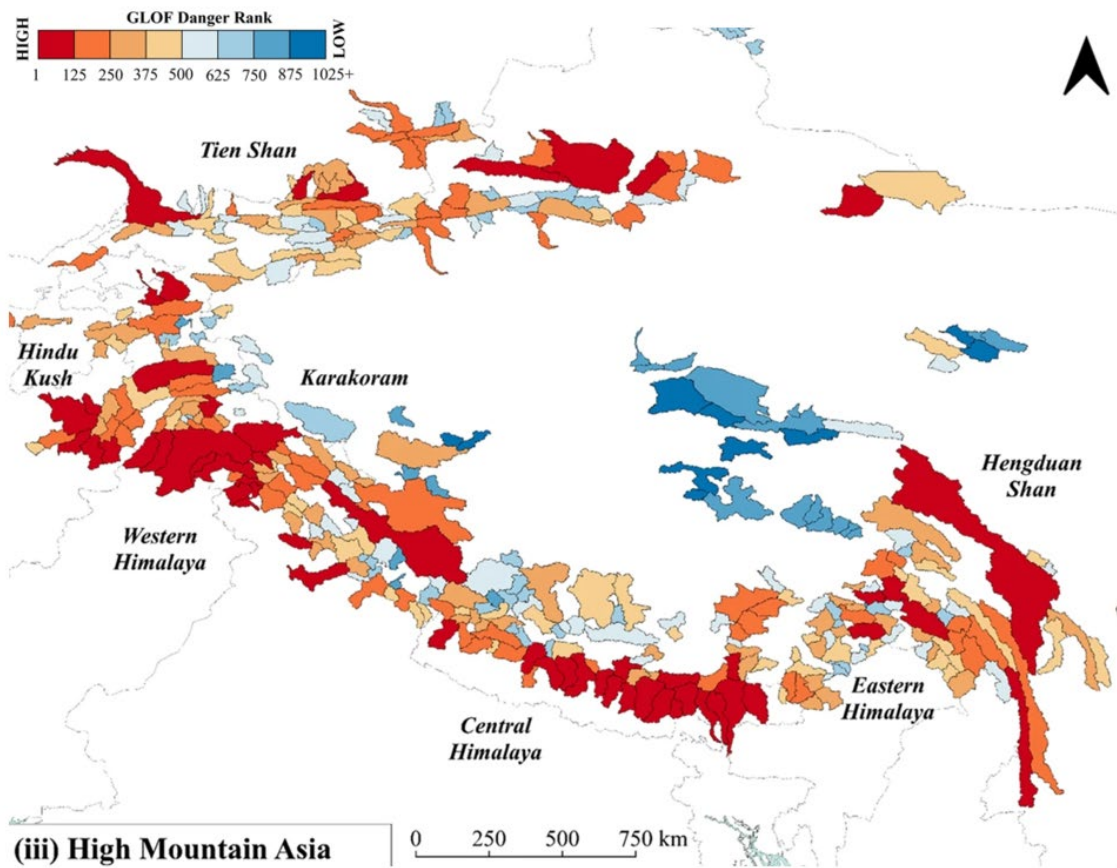


Figure 7. Spatial distribution of GLOF danger in HMA at basin scale from high (red) to low (blue) risk (Adopted from Taylor et al., 2023).



Figure 8. Consequences of an outburst flood and mudflow from Baralmos Glacier, July 2023. The image shows the geomorphological impacts downstream, including sediment deposition and flooding of the area, including automobile road.

The occurrence of these events in the Pamir region emphasizes the necessity for improved hazard assessment and monitoring of glacial lakes and the implementation of mitigation strategies to protect communities and infrastructure.



Figure 9. Closure of the Surkhob riverbed after the event (left) and the destroyed international road in the Lyakhsh region (right) (photos from Baralmos field report 2023).

2.4. Socio-economic impacts of GLOFs

In the high-mountain areas, GLOFs present significant social and economic problems by threatening lives, damaging infrastructure, and prohibiting the growth of local economies. Those communities that are situated below the glacial lakes are always in danger due to the sudden and uncertain nature of GLOFs (Ahmed, 2024). The aspect that makes GLOF the most dangerous is the fact that they are unpredictable. Among the worst GLOF disasters was the one that took place in Huaraz Peru in the year 1941, when the Lake Palcacocha outburst floods caused the death of 5,000 people and destroyed a third of the town (Carey et al., 2012). In Nepal, Dig Tsho GLOF 1985 destroyed a newly built hydroelectric power plant crucial to the local economy, resulting in widespread flooding, loss of crucial crops, destruction of houses, and loss of lives (Vuichard and Zimmermann, 1987).

Moreover, GLOFs have far-reaching impacts aside from just agriculture suffering losses, water scarcity, and depletion of infrastructure to support local trade. The end result of which is communities struggling in poverty with no aid to improve their situation. The burden often shifts to local governments which as a result stop being able to fund any future improvements.

Regular monitoring of glacial lake dynamics, with a particular emphasis on hazardous glacial lakes, is a necessary condition for preventing glacial lake failure (Wang and Zhou, 2017). Disaster risk reduction strategies include structural and engineering interventions, strategic land use and planning, community-based disaster preparedness, monitoring, and early warning systems.

Important elements of GLOF mitigation include engineering solutions such as lake-lowering projects, protection barriers, and drainage canals. For example, drainage systems that have been implemented at Lake Palcacocha in Peru have decreased its capacity and decreased the probability of future GLOFs (Carey, 2008). To reduce the amount of infrastructure development in high-risk locations, it can be beneficial to analyze probable GLOF hazard areas and create distinct hazard zones depending on various GLOF scenarios with the appropriate zoning laws and building norms (Sattar et al., 2023).

The involvement of local communities during disaster preparedness increases the efficiency of responding to GLOF incidences. For example, locals in Peru have opposed hazard-zoning laws that would have prohibited building within possible flood routes (Emmer et al., 2022a). Therefore, educational campaigns are crucial in increasing public knowledge of the risks posed by GLOFs and the value of readiness.

The entire process of preventing and lowering the risks of a GLOF disaster should involve various stakeholders, including governments at all levels, specialists, businesses, nongovernmental organizations, and citizens (Thompson et al., 2020).

3. Study area

3.1. Location and glaciation characteristics

The Petra Pervogo range (also called “Peter the First” or “Peter the Great” range) is situated in central Tajikistan, northwest of the Pamir mountain system. It extends from west to east for 180 km from the confluence of the Surkhob and Obikhingou rivers up to the Academy of Sciences ridge. The Baralmos Glacier (39.101°N, 71.387°E) (Figure 10) is located on the northern slope of the Peter I Ridge of the Surkhob River (also known as Vakhsh River) basin, covering an area of 6.3 km² and ranging between 3440 to 4420 m asl (*Catalogue of Glaciers of the USSR*, 1978; Safarov et al., 2024). The Kyzylsu Glacier (39.095°N, 71.418°E) (Figure 11) is next to the Baralmos Glacier (Figure 12).



Figure 10. Baralmos Glacier. Photo from the study site, August 2024 (photo by Evan S. Miles).



Figure 11. Kyzylsu glacier viewed from the eastern side, 2023 (photo by Jason Klimatsas).

The Obikhingou River basin contains numerous complex valley glaciers, primarily located in the highest sections of ridges, predominantly on north-facing slopes (*Catalogue of Glaciers of the USSR, 1978*). Many of these valley glaciers have limited accumulation areas as they lie entirely in narrow, deep valleys. Together with constant avalanches, a large amount of debris falls on the surface of glaciers.

What distinguishes the Pamirs is that, from all other high-mountain regions, the abundance of surging glaciers predominates there. As it was specified by Kotlyakov et al. (2021), at least ten glaciers come into that active phase of movement every year. In most cases, the time from the origin of kinematic waves propagating through a glacier to the full development of the pulsation process ranges from one to two but sometimes as long as five years. These surging glaciers pose a significant glaciological hazard by blocking proglacial water flows, which can lead to the formation of glacial lakes and increase the risk of flooding caused by GLOFs (Vale et al., 2021).

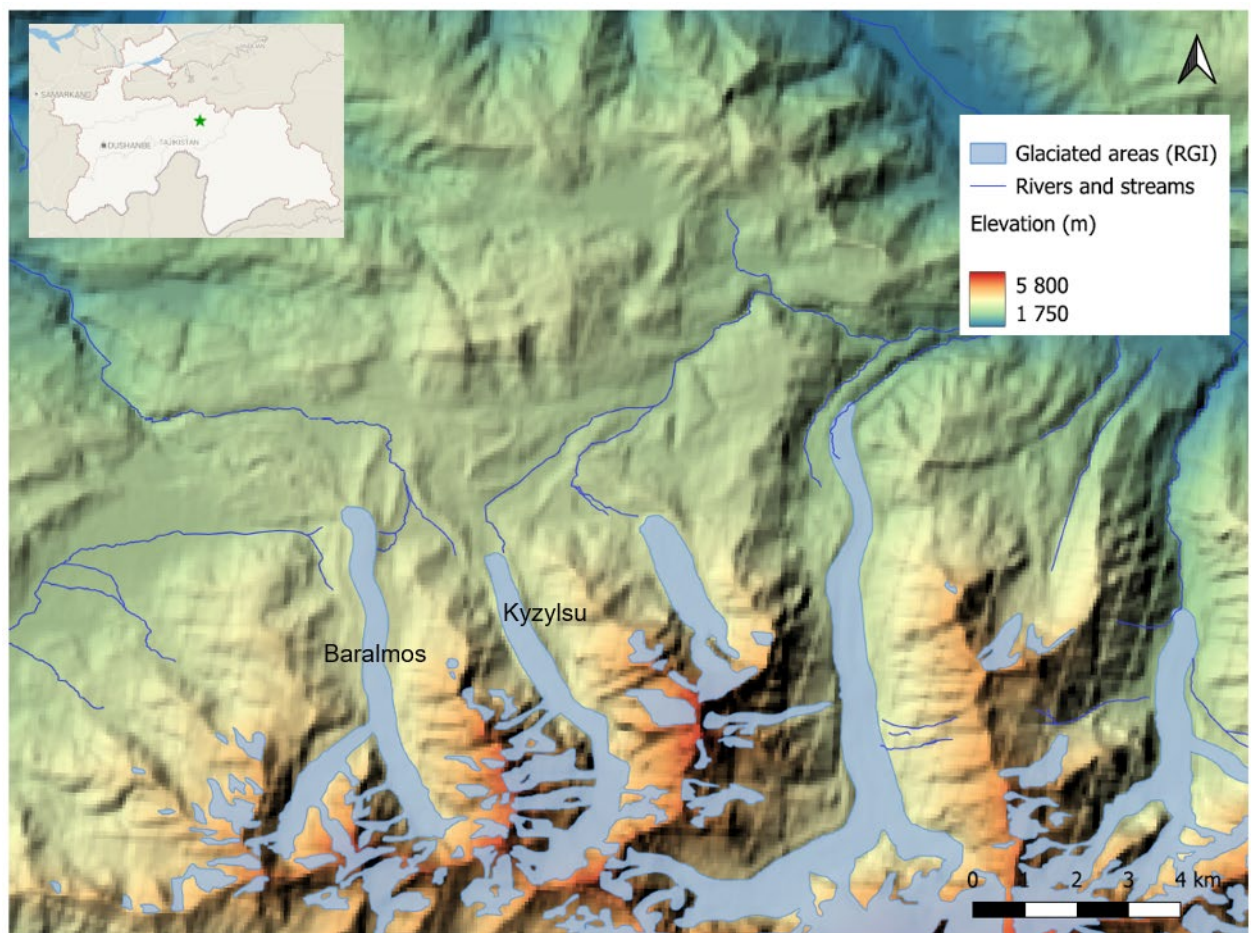


Figure 12. Map of study site in Tajikistan with the indication of Baralmos and Kyzylsu glaciers. Glaciated areas were delineated using the RGI dataset, and the background elevation data and hillshade were derived from the SRTM DEM (USGS), upper map and water objects were obtained from OpenStreetMap.

In the northwestern part of the Pamirs, surge-type glaciers are present in the Surkhob and Obikhingou river basins. Between 2015 and 2020, six glaciers in the Surkhob basin experienced surges, including one of the most well-known glaciers, the Didal Glacier (Kotlyakov et al., 2021).

The Baralmos Glacier is a surge-type, complex valley glacier, that is formed by the confluence of two almost equally large streams of ice. The accumulation area is not morphologically expressed, and the firn line aligns with the lower boundary of large avalanche cones (*Catalogue of Glaciers of the USSR*, 1978; Safarov et al., 2024). The tongue of the glacier is almost completely covered with a moraine (Figure 13). There are also a large number of lakes and crevasses on the glacier.

Currently, Baralmos Glacier is in the quiescent phase of its surge cycle, meaning the glacier's terminus is gradually melting without the supply of new ice. This downwasting, especially around surface ponds, is a notable characteristic during this stage of the glacier's development (Thompson et al., 2012). Two key processes are associated with this: first, the production of excess local meltwater during the ablation season (Miles et al., 2018b), the second one is the enhanced water retention potential in the glacier's terminus area (King et al., 2020). As a result, while outburst floods are related to seasonal variations in stored surface water, it is crucial to take into account the general trends and the time series when examining the variations in surface water storage.



Figure 13. Moraine-covered tongue area of Baralmos glacier. Photo from the study site, August 2024 (Evan S. Miles).

3.2. Weather and climate

The Pamirs have a continental, arid climate, characterized by frigid winters and warm, relatively dry summers (Encyclopedia Britannica, 2024). In general, the area is dominated by westerly winds, Siberian cyclones, and a weakening southwest Indian monsoon (Zhang and Kang, 2017).

Among these, the westerly wind has the most dominating effect on the Pamirs, combining to bring very scarce precipitation. In the western Pamirs, annual precipitation averages 600 mm, mostly occurring in winter and spring, whereas in the eastern Pamirs, it reaches only 100 mm, with most rainfall happening in spring and summer (Khromova et al., 2006). According to the Global Permafrost Map, permafrost in the Pamirs is discontinuous because of varied altitudes and climatic conditions in the region (Obu et al., 2019). In particular, permafrost occurs within those areas where temperatures in the ground fluctuate above and below freezing.

Key climatic information for the area can be obtained from two meteorological stations (for the period of 1879 – 2003), one at Rasht/Garm (1316 m; 39.02° N, 70.37° E), located in the Surkhob Valley and the other at Lyairun (2008 m; 38.89° N, 70.93° E), situated over the Obikhingou River (Williams and Konovalov, 2008). However, it should be pointed out that both stations are situated at a considerable distance from the Baralmos glaciers and as such, the climate data provided would be quite unsuitable for the conditions prevailing in the glacier portion of the environment.

In June 2021, a monitoring network was established in the Jirgatal district of Tajikistan through a collaboration between researchers from the Swiss Federal Research Institute WSL and the Center for the Research of Glaciers of the Tajik Academy of Sciences (CRG). The network includes several stations (Automatic Weather Station (AWS), pluviometer station, and several meteorological stations) strategically positioned near the Kyzylsu Glacier to capture detailed climatic data. Hourly multi-variable downscaled and bias-corrected meteorological data (prepared by Achille Jouberton) for a station located in the Kyzylsu catchment, were used to gain valuable information about the local climatic conditions.

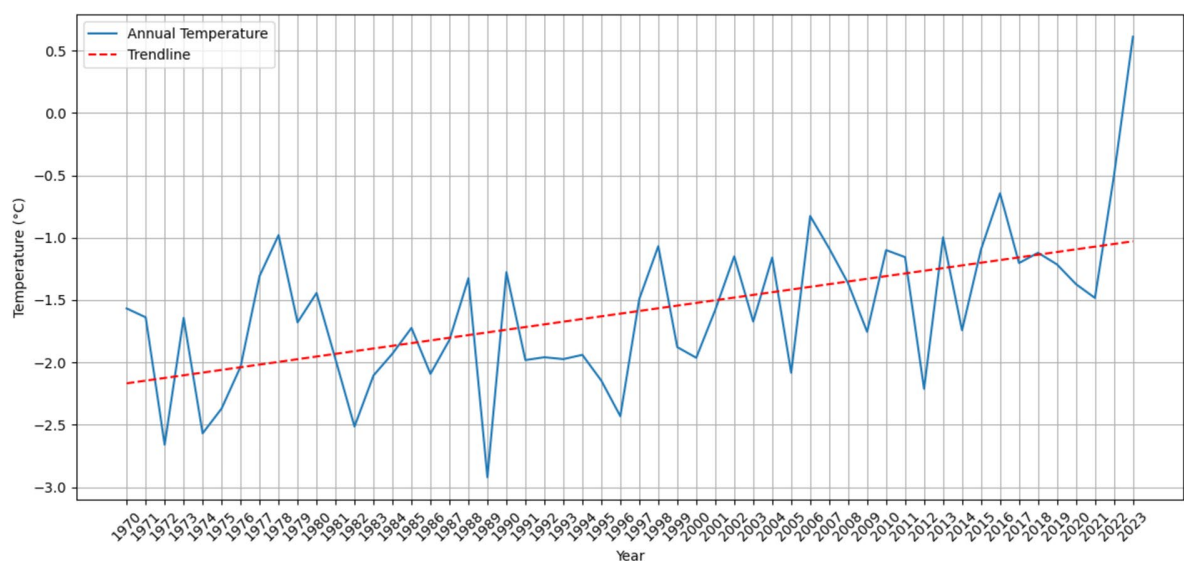


Figure 14. Change in the average annual temperature (1970-2023) in the study area based on hourly multi-variable downscaled and bias-corrected meteorological data

Based on the data provided, a graph was obtained (Figure 14), which illustrates the change in the average annual temperature in the study area from 1970 to 2023. The general trend indicates a steady increase in average temperatures, which is consistent with broader trends in climate change.

In the Pamir region, the effects of temperature and precipitation on cryospheric changes have been extensively researched (Pohl et al., 2014; Safarov et al., 2024). There are notable fluctuations in the temperature and monthly precipitation in the Baralmos glacier. For example, from 2002 to 2022, the research area had an increase in July temperatures ($1.34^{\circ}\text{C}/\text{decade}$; $p < 0.05$) and a decrease in December precipitation ($-1.19 \text{ mm}/\text{decade}$) (Safarov et al., 2024). Higher July temperatures promote surface melting during the ablation season, which increases meltwater production and promotes the expansion and drainage of supraglacial ponds. At the same time, less precipitation in December probably means less snow accumulation in the winter, which limits the glacier's capacity to regain mass.

4. Data and Methods

4.1. Approach

The following sections in this chapter outline the analysis performed to achieve the research goals presented in the introduction.

For the first objective, which revolves around analyzing the contemporary history of outburst floods and their impacts, I focused on high-resolution multispectral images. Analysis of pond locations and their changes in sub-seasonal periods was done to establish the timing and scale of large drainage events. The methodological steps for image processing and pond mapping are specified in Section 4.3. Then, applying an area-volume scaling approach (Section 4.4) that had been determined for these types of supraglacial water bodies, I estimated water volume changes for individual ponds and the entire pond system which can be used for further flood magnitude estimations.

Towards objective 2, which seeks to compare the recent ponding activity to historical activity, I integrated the historical (1990s-2015) Landsat Imagery with the recent PlanetScope Imagery used in previous sections. This permitted a long-term assessment of changes in surface water storage that occurred on the glacier, as well as capturing key transitions such as the effects of the 1998 glacier surge on pond dynamics and subsequent recovery of water storage. The data used for these analyses are further described in Section 4.2.1, and the methodological steps for image processing can also be found in Sections 4.3 and 4.4.

Objective 3 aims to investigate whether there are clear signs of geomorphological changes linked to pond drainage events. In order to do this, I used high-resolution Pleiades stereo imagery taken between 2021-2023 for the study area. The methods for this part are discussed in Section 4.6.

Finally, fulfilling objective 4, which is to focus on the relationships of changes in pond areas, I performed an analysis of separate pond areas extracted from NDWI-based masks. With the help of these analyses, I could investigate relationships between the ponds and possible hydrologic connections, and determine whether draining one pond affected the activities of other ponds.

4.2. Remote sensing data

4.2.1. Satellite images

The dynamics of the ponds on the Baralmos Glacier were examined in this research based on remote sensing data.

The primary data source was PlanetScope imagery (2017–2024), which offers high spatial resolution (3 meters) across four spectral bands: blue, green, red, and near-infrared (NIR). These high-resolution images were key for detecting small water bodies and analyzing their spatial and temporal dynamics in detail. For the Baralmos Glacier, 171 PlanetScope images were used together with additional 2023-2024 ones for Kyzylsu Glacier for similar pattern analysis. It is important to mention that the early snowmelt period (May-June) faced a high cloud and snow coverage, which affected some satellite images acquisition.

In addition, this study also utilized Landsat imagery from Landsat 4, 5, and 7 to provide a historical context. Although Landsat imagery has a lower resolution than PlanetScope, it helped analyze long-term variations in glacial lake changes at Baralmos Glacier. The combination of high-resolution recent datasets with historical datasets enabled an all-around evaluation of both recent fluctuations as well as long-time tendencies.

Table 1 gives an overview of this study's satellite data, including their spatial resolution, temporal coverage, and sources.

Table 1. *Satellite data summary*

Satellite image type	Dates	Resolution (m)	Source
PlanetScope (for Baralmos)	2017 – 2024	3	European Space Agency (ESA) PlanetScope Archive
PlanetScope (for Kyzylsu)	2023 – 2024	3	European Space Agency (ESA) PlanetScope Archive
Landsat 4/5/7 (for Baralmos)	20.08.1993; 21.09.1993; 23.08.1994; 02.10.1997; 02.08.1998; 03.09.1998; 05.08.2002; 13.08.2008; 04.09.2010; 26.07.2013; 16.07.2015.	30	U.S. Geological Survey Earth Resources Observation and Science – earthexplorer.usgs.gov

4.2.2. DEM

This work also used high-resolution Pleiades stereo imagery (Shean et al., 2020) acquired for the Baralmos and Kyzylsu glaciers during 2021-2023. As part of the PAMIR project, datasets for 2022 and 2023 were processed into DEMs (Digital Elevation Models) and orthoimages, which allowed detailed analysis of surface topography and glacial lake geometries. The high spatial resolution of Pleiades imagery made it possible to capture supraglacial ponds, moraine structures, and erosion channels. One limitation factor is that DEMs, especially those derived from satellite imagery like the Pleiades, can contain striping artifacts or systematic patterns caused during data acquisition and processing.

4.3. NDWI

The NDWI (Normalised Difference Water Index) is one of the most common methods used in remote sensing for distinguishing water bodies from satellite images through the reflection properties of water in certain spectral ranges (Guo et al., 2017). High absorption of near-infrared (NIR) radiation and strong reflectance of green light by the water surfaces make this index effective in separating water from adjacent terrain, vegetation, and other land features. The NDWI is calculated using the formula:

$$\text{NDWI} = \frac{X_{\text{green}} - X_{\text{nir}}}{X_{\text{green}} + X_{\text{nir}}} \text{ (McFeeters, 1996).}$$

The NDWI is a zero-centered index with a value range of $[-1, 1]$. Water strongly absorbs NIR wavelengths but reflects green light, so positive values (>0) indicate the presence of water. Non-water surfaces like vegetation or soil usually have negative values because their reflectance properties in such spectral bands differ.

NDWI has been commonly used in monitoring the supraglacial lakes, glacial melt ponds, and proglacial water body dynamics in high-mountain environments (Jha and Khare, 2017; Miles et al., 2018a; Wangchuk and Bolch, 2020; Zhang et al., 2022). Its ability to detect subtle water body changes is critical for areas like Baralmos Glacier where ponds develop rapidly during the ablation period.

The NDWI was calculated for each scene using the green and NIR bands of PlanetScope imagery. To automate and improve this procedure, a customized Python workflow that integrated advanced geospatial libraries including *rasterio*, *numpy*, *geopandas*, and *matplotlib* was created (Figure 15).



Figure 15. Workflow for NDWI calculations. This diagram illustrates the step-by-step process for extracting water bodies from satellite imagery.

The Python code executed a systematic workflow for NDWI computation and water body detection. The initial step involved loading and *rasterio* pre-processing of satellite imagery in order to cut and mask data to the study area boundary based on the glacier *shapefile*. After that, the formula for NDWI was applied. Figure 16 shows how all the index calculation steps were visualized. The histogram shows the distribution of NDWI values.

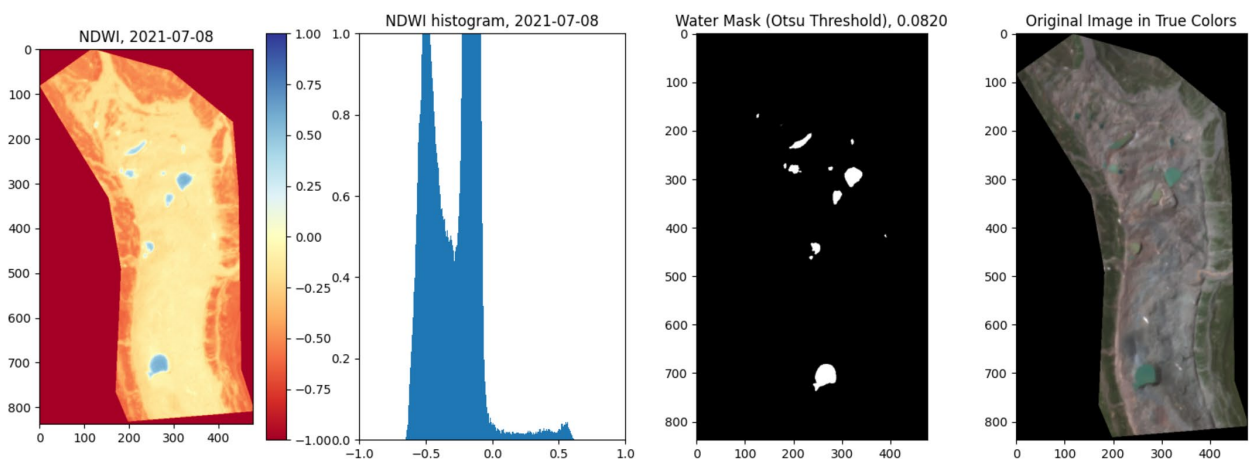


Figure 16. Results of NDWI analysis on Baralmos Glacier (8th of July 2021). From left to right: (1) NDWI values, (2) NDWI histogram, (3) binary water mask generated by Otsu's threshold, and (4) the original image in true colors.

The computed NDWI values were subjected to Otsu's thresholding method using Python libraries such as *scikit-image* for accuracy enhancement. This histogram-based adaptive technique, introduced by Otsu (1979), identifies an optimal threshold value that minimizes intra-class variance, effectively separating water pixels from non-water pixels (Cooley et al., 2017; Otsu, 1979). By automating the thresholding process, Otsu's method reduces the potential for subjective bias and ensures consistency across datasets. The workflow also implemented an iterative refinement procedure, which divided the NDWI image into smaller sub-regions and recalculated the threshold for each region (Figure 17). This step was particularly effective in detecting small or partially obscured water bodies. The results were manually reviewed for each date to address potential biases or misclassifications due to limitation factors like clouds and snow cover.

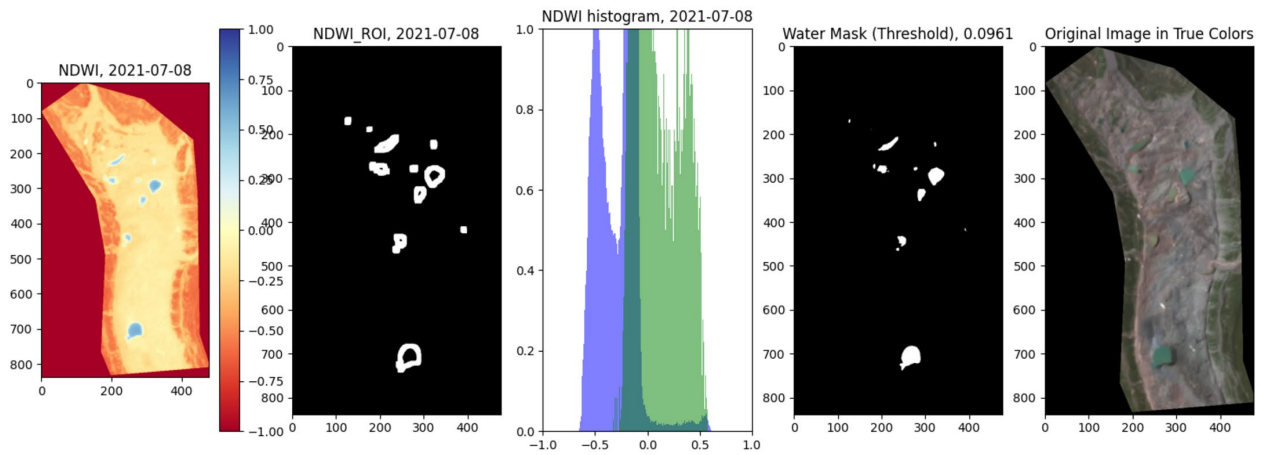


Figure 17. NDWI analysis with iterative refinement for Baralmos Glacier (8th of July 2021). Histogram (3) presents the distribution of NDWI values with the optimized threshold value.

The rasters were converted into vector polygons after classification using *rasterio.features.shapes* and the results were saved in *geopandas* as *GeoDataFrames*. Finally, the outputs were exported as Excel files for further analysis.

In addition to the primary analysis, the lake-frequency map was generated by aggregating the binary water masks over the entire time series. Using *NumPy*, the binary masks were simply summed pixel-wise, providing the number of times each pixel was classified as water. The total number of images in the dataset was then used to normalize this count, yielding a water frequency value for each pixel expressed as a percentage.

4.4. Area and volume estimations of Baralmos ponds

Determining the volume of water can be difficult in mountainous conditions, due to the inaccessibility of the lakes, the inability to use heavy equipment (boats, echo sounders), the likelihood of dangerous processes threatening the researcher's life (collapses, separation of icebergs of glaciers), the inability to fully explore the surface of the lake. In such cases, empirical formulas can be used to determine the volume of the lake. One widely applied model (Byers et al., 2013; Jain et al., 2012; Mergili and Schneider, 2011) is by Huggel et al. (2002), which provides an empirical relationship for moraine-dammed lakes. This dependence is based on a study of glacial lakes in North America, South America, the Himalayas, Iceland, and the European Alps. Watson et al. (2017) developed an improved model for supraglacial and proglacial lake volume estimation using high-altitude Himalayan lakes. This paper served as the basis for calculating the volume of ponds on the Baralmos Glacier in this study.

Water body pixels, received after NDWI calculations, were converted into vector polygons, enabling area measurements in square meters. Only polygons with an area greater than two pixels

were retained to eliminate noise and improve accuracy. To estimate pond volumes, the method utilized the empirical formula proposed by Watson et al. (2017) (Figure 18), where pond volume is approximated as: $V = 0,1535A^{1,39}$, where A is the area (m²).

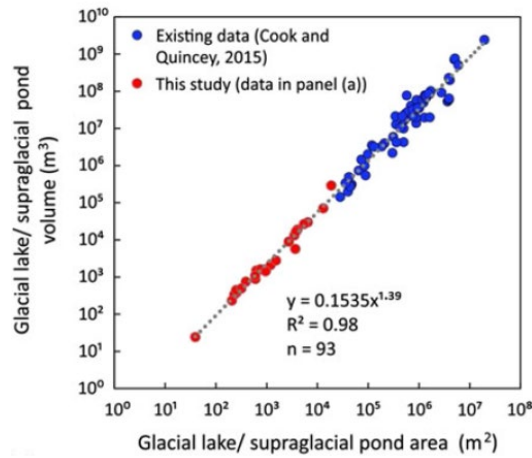


Figure 18. The data of the Watson et al. study combined with the compiled dataset of Cook and Quincey (2015). The scatter plot shows a strong correlation between pond area and volume.

Using this workflow, both the total areas and volumes of Baralmos Glacier ponds and the areas and volumes of individual ponds were calculated. For historical comparisons, data derived from 30 m resolution Landsat imagery were also analyzed. However, due to the coarse resolution, automatic NDWI-based classification was not always feasible, and manual adjustments were necessary. This may cause some estimation bias, especially for smaller ponds that could not be identified at this resolution.

4.5. Interconnectivity analysis

This part of the research focuses on the interconnectivity of the supraglacial ponds at Baralmos Glacier during notable area changes. The objective is to find out whether, during major events or processes, ponds experience changes autonomously or not. To determine the interconnections of the pond area changes, several supraglacial lakes were studied (Figure 19).

For each pond, the percentage change was calculated relative to the previous observation:

$$\text{Percentage Change} = (\text{Area at Time}_t - \text{Area at Time}_{t-1}) / \text{Area at Time}_{t-1} \times 100$$

This approach allowed for a detailed assessment of lake dynamics. The primary changes were identified and their magnitudes were estimated by comparing the area before and after major drainage events.

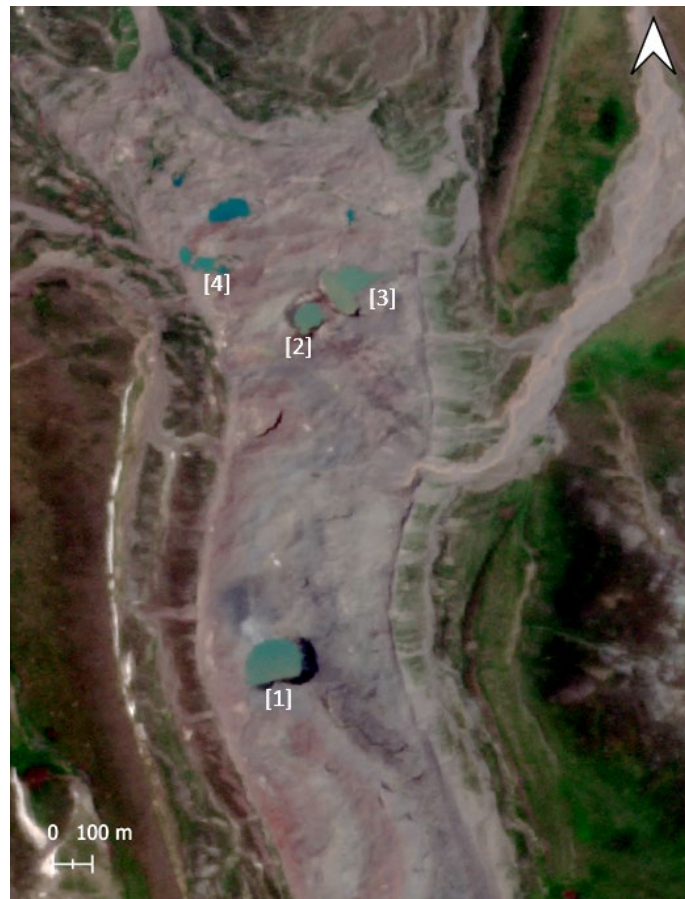


Figure 19. The satellite image shows the spatial locations of analyzed ponds ([1], [2], [3], and [4]) on Baralmos glacier, which can be also seen on the lake-frequency map (Figure 32).

4.6. DEM analysis

This study used DEM analysis to identify geomorphological changes caused by GLOFs and assess stream channel erosion and sedimentation. The workflow (Figure 20) was created in Python, using various advanced geospatial libraries such as *xdem*, *geoutils*, and *rasterio*. This code is inspired by the open-source Github (Shean et al., 2016) and adapted to the specific requirements of this study.



Figure 20. DEM Analysis Workflow. The procedure for examining Digital Elevation Models (DEMs) in order to identify elevation variations and other geomorphological changes is described in this diagram.

The raw DEM preparation process began with the reprojection to ensure alignment in spatial resolution and coordinate systems. A stable terrain mask was generated to isolate areas that exhibit minimal change over time such as bare ground (using Bare Ground 30 m mask) (Hansen et al.,

2013) and slopes below 30 degrees, while excluding dynamic features like glaciers (using RGI 7.0 glacier outlines) (RGI Consortium, 2023) and stream channels. These masks ensured that reference points for coregistration were robust and unaffected by geomorphic processes. Figure 21 illustrates the bare ground mask and slope mask, while Figure 22 shows the final stable terrain mask.

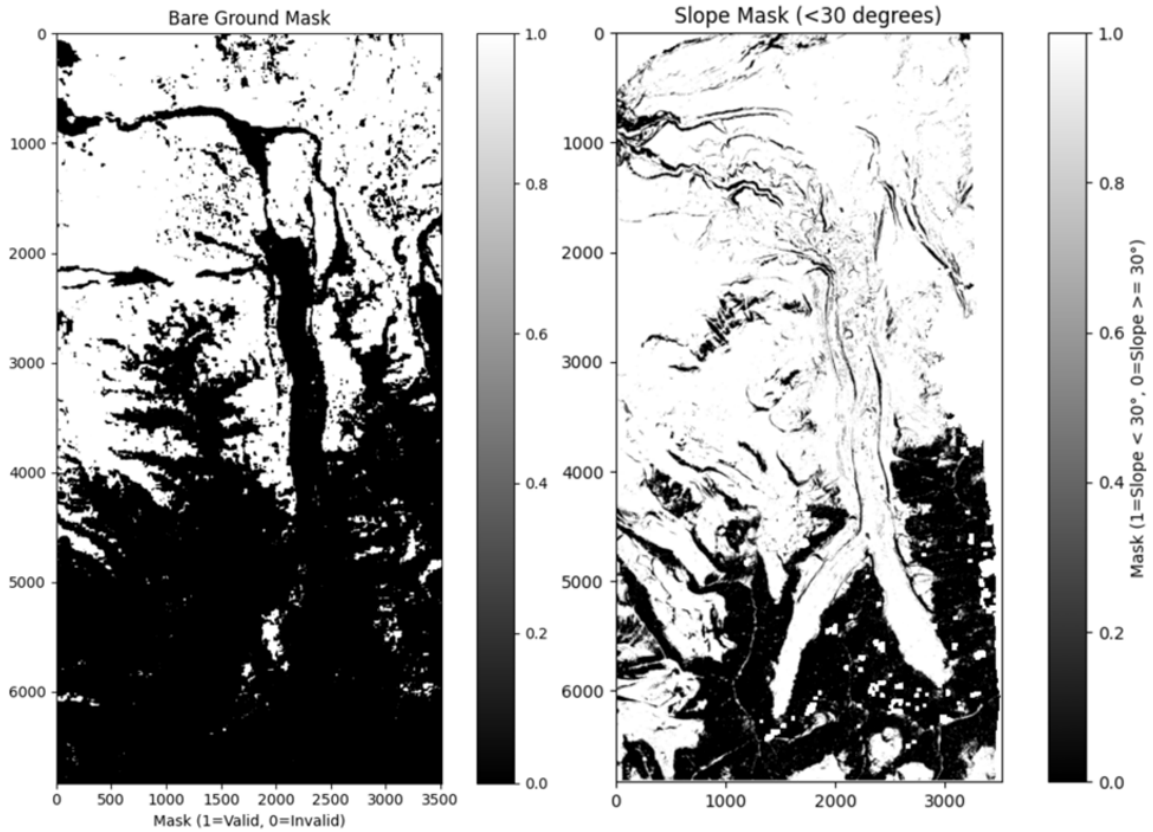


Figure 21. Bare ground (left) and slope (right) masks. The function `xdem.terrain.slope` was used to calculate the slope from the input DEM to create the slope mask. The slope mask finds areas with slopes below a specified threshold (30°) to guarantee the stability of the terrain; the bare ground mask was applied to isolate non-glacierized stable terrain. These masks were employed to delineate further stable terrain for accurate and precise coregistration of DEMs and detection of changes.

To correct for horizontal and vertical systematic offsets between DEMs resulting from acquisition and processing, the coregistration involved adopting Nuth and Käab (2011) method. The cosine equation between terrain slope, aspect, and elevation differences is solved iteratively by this method to evaluate horizontal displacement. The iteration is stopped if the maximum number of iterations is reached or if the shift's amplitude of iteration falls below the given tolerance value.

A representation of the difference in heights before and after using Nuth and Kaab's registration approach is plotted using the histogram (Figure 23). After adjusting for systematic errors, the median and normalized median absolute deviation (NMAD) values are improved. This was followed by calculating elevation differences between the two DEMs to identify erosion and deposition areas.

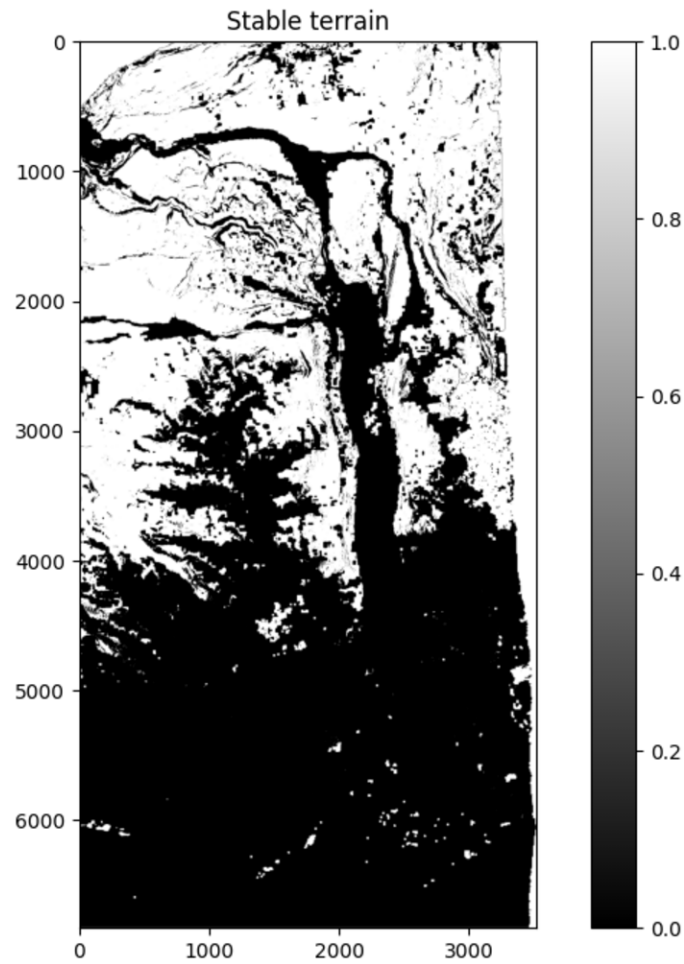


Figure 22. A stable terrain mask was generated in the Python environment. The mask identifies unstable regions (black areas) and stable terrain (white areas) based on the above mentioned masks.

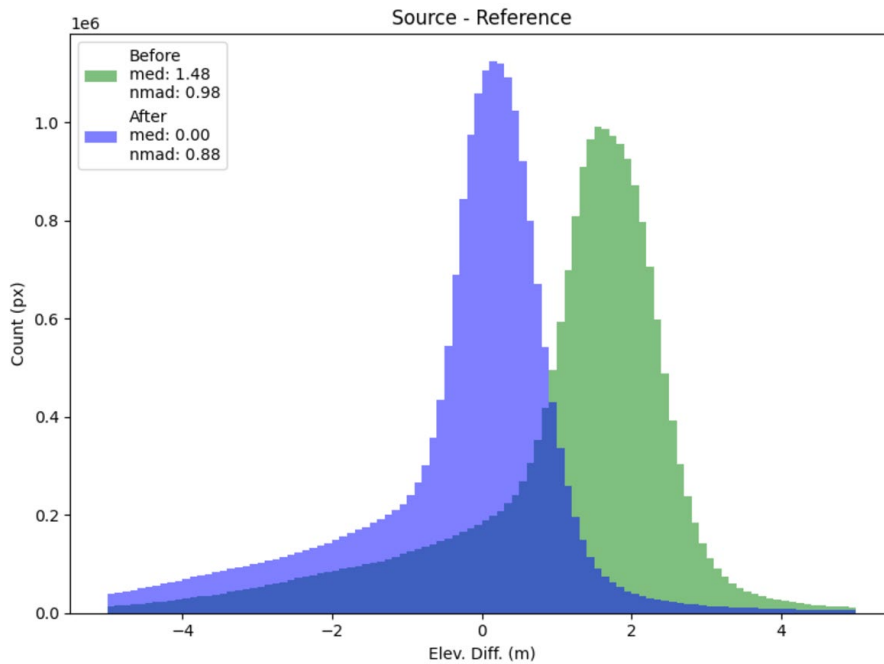


Figure 23. Histogram of elevation differences (before and after correction). The blue histogram captures the differences in elevations before coregistration and bias correction, while the green histogram represents the differences post-coregistration. The median elevation difference and NMAD values are presented for both cases, showing the improvement achieved after coregistration.

5. Results

5.1. Temporal dynamics of supraglacial ponds

5.1.1. Seasonal and multi-year dynamics for the recent period

The seasonal and multi-year trends of pond activity on the Baralmos Glacier from 2017 to 2024 are examined in this section. These results can help to comprehend the dynamics of recent changes and are supported by the techniques described in the previous chapter, such as area-volume scaling and NDWI computations. 171 satellite images for 2017-2024 were analyzed. Additionally, for 2023-2024, 24 images were analyzed for the Kyzylsu glacier, which, as mentioned earlier, is located next to the Baralmos glacier. All numerical data (volume and area) for this chapter can be found in the Appendix (Tables 2, 3, and 4) and area and volume graphs for each year if they are not shown in the chapter.

Seasonal activity trends indicate that the area and volume of ponds reach their peak in July and August. These peaks across multiple years align with the snowmelt period. This snowmelt exposes pre-existing lakes while also supplying meltwater to fill depressions, resulting in consistent annual increases in lake area and volume. By mid to late summer, the majority of years show rapid drops due to drainage events. Three big drops were recorded in July, making it the month with the most significant drainage occurrences. The lake's area and volume have increased throughout time, according to the results (Figures 24 and 25), especially in 2020 and the years that followed (2021–2024).

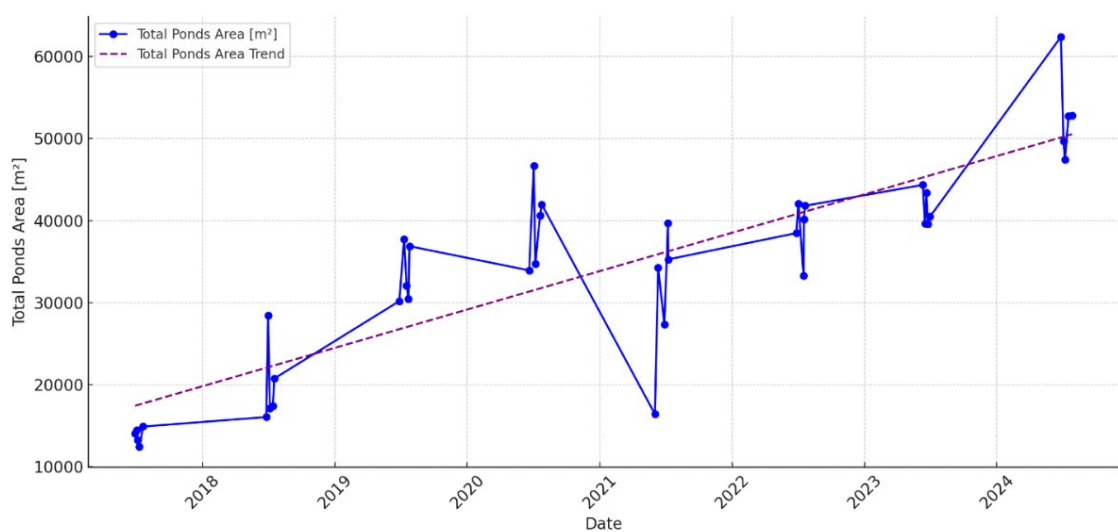


Figure 24. Total pond areas over time (2017–2024) for Baralmos glacier.

Pond area and estimated volume are generally smaller in 2017-2019 than in more recent years. The majority of pond area and volume numbers fall between 12,000 and 21,000 m² and 50,000

and 90,000 m³, respectively. Pond areas in other years, particularly 2020, 2022, 2023, and 2024 are much larger (up to ~61,000 m² in 2020).

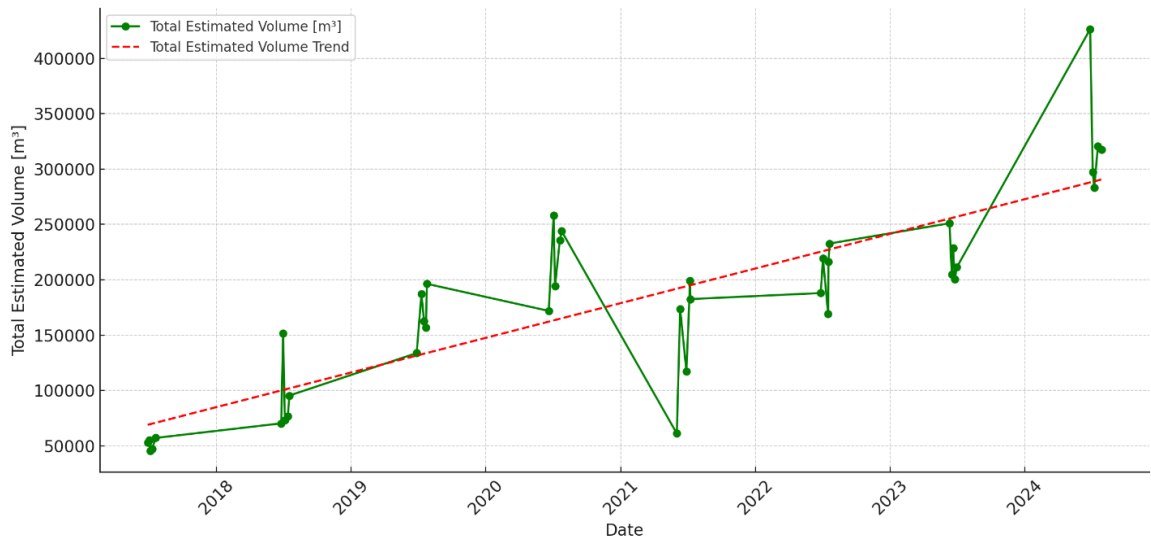


Figure 25. Total estimated pond volumes over time (2017–2024) for Baralmos glacier based on a formula from Watson et al., 2017.

There is a noticeable seasonal trend, with late June to August usually seeing the largest overall pond areas. Over several years, July typically has the highest pond coverage. However, these peak values' magnitudes differ yearly (see Figure 26). Notably, the overall pond area has grown since 2019, especially in 2020, 2022, and 2024, when the pond covering surpassed 60,000 m².

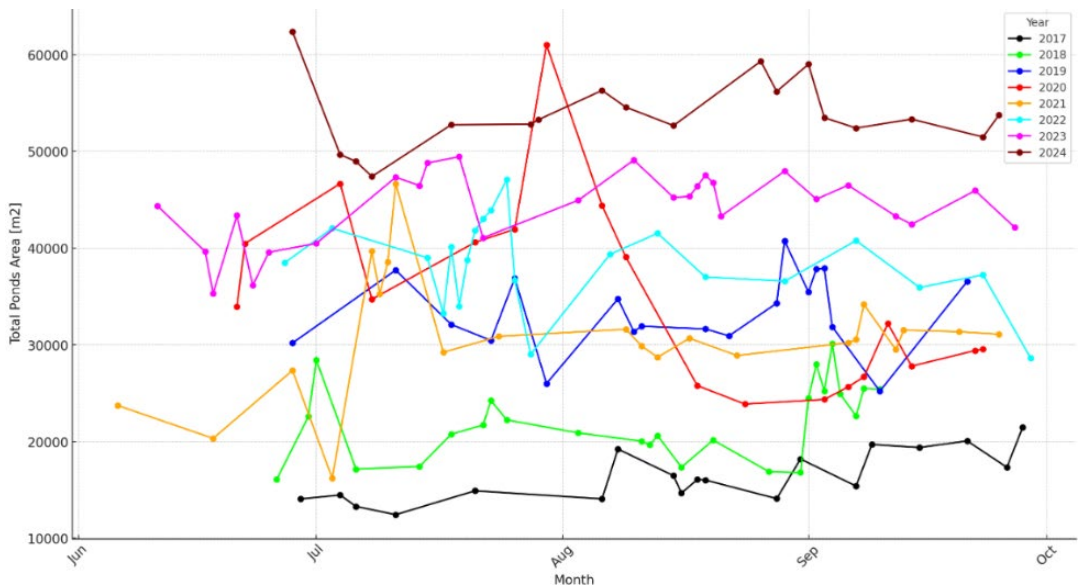


Figure 26. Total pond areas on Baralmos Glacier from 2017 to 2024, plotted by the day of the year. Each line represents a different year.

In contrast to more recent years, when we observe more noticeable peaks and falls, 2017 shows more consistent and minor variations in pond area and volume. Although there was a peak in July and August 2017, it was not as noticeable as those seen in subsequent years (Figure 27). The graph

shows that the largest drainage event for this year was between 8 and 15 August. In 2018, by contrast, a significant drainage event occurred at the beginning of July.

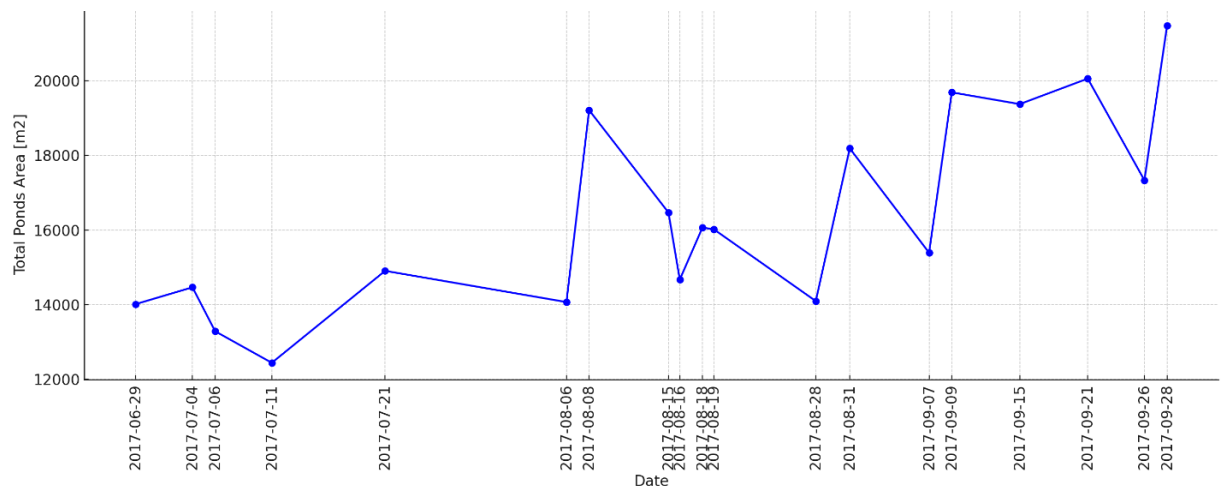


Figure 27. Total pond areas over time (2017).

In 2020, the most significant drainage event occurred between 29 July 2020 and 5 August 2020. During this period, the total pond area dropped sharply from 61,002 m² to 44,406 m², and the estimated volume decreased from 375,848 m³ to 267,621 m³. Further, the area of the lakes continued to decline, which most likely indicates a series of ongoing water discharges.

In 2021, a drainage event was observed between 11 July 2021 and 17 July 2021, when the total pond area decreased significantly from 46,655 m² to 29,223 m², while the estimated volume dropped from 268,502 m³ to 136,562 m³ (Figure 28), which caused the debris flow down the valley. After that, the volume and area values remained stable, with minimal fluctuations.

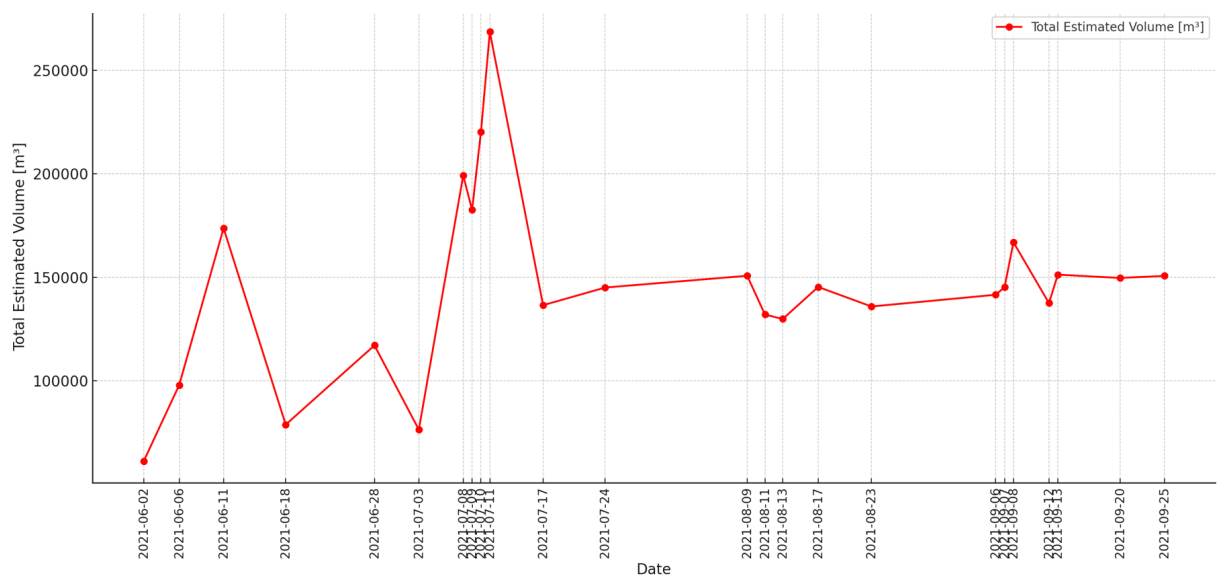


Figure 28. Total estimated volume over time (2021) based on a formula from Watson et al., 2017.

A significant drainage event in 2022 occurred from July 25 to July 28. The estimated volume of the pond dropped from 295,295 m³ to 139,712 m³, with the overall area shrank from 47,070 m² to 29,016 m² (Figures 29 and 30). It is essential to mention that the drainage of glacial lakes continued for several days, with a minimum of areas and volumes reaching on July 28.

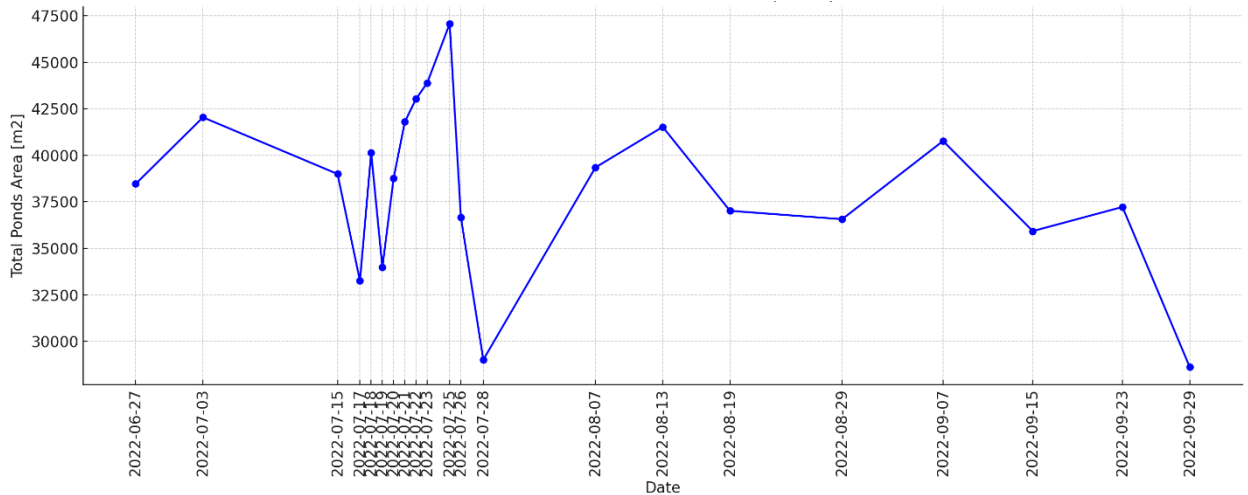


Figure 29. Total pond areas over time (2022).



Figure 30. Sequence of NDWI and true-color imagery illustrating the 2022 drainage event on Baralmos Glacier. The images show that the pond areas have decreased, especially in the main pond—pixel resolution: 3x3 meters per pixel.

In 2023, a significant drainage event was observed between 19 July 2023 and 22 July 2023 (Figure 31). The total pond area dropped from 49,437 m² to 41,058 m², and the corresponding volume decreased from 310,118 m³ to 221,050 m³. An illustration of this event can be found in Figure 32, which displays true-color satellite pictures and NDWI maps from July 19 and 22, 2023. The NDWI maps clearly depict the reduction in pond areas between these dates, evidenced by the shrinking bright blue regions that represent water bodies.

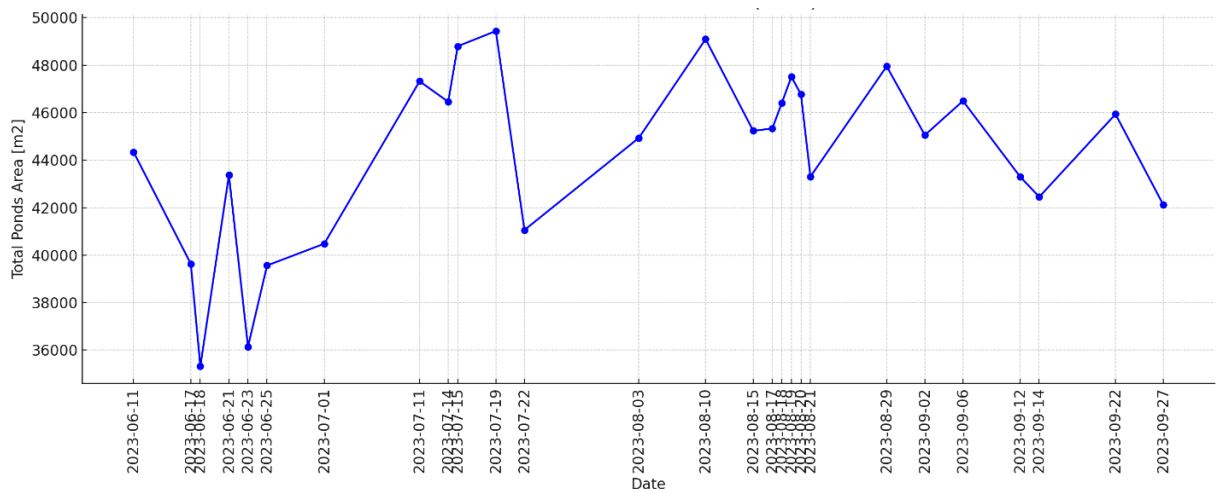


Figure 31. Total pond areas over time (2023).

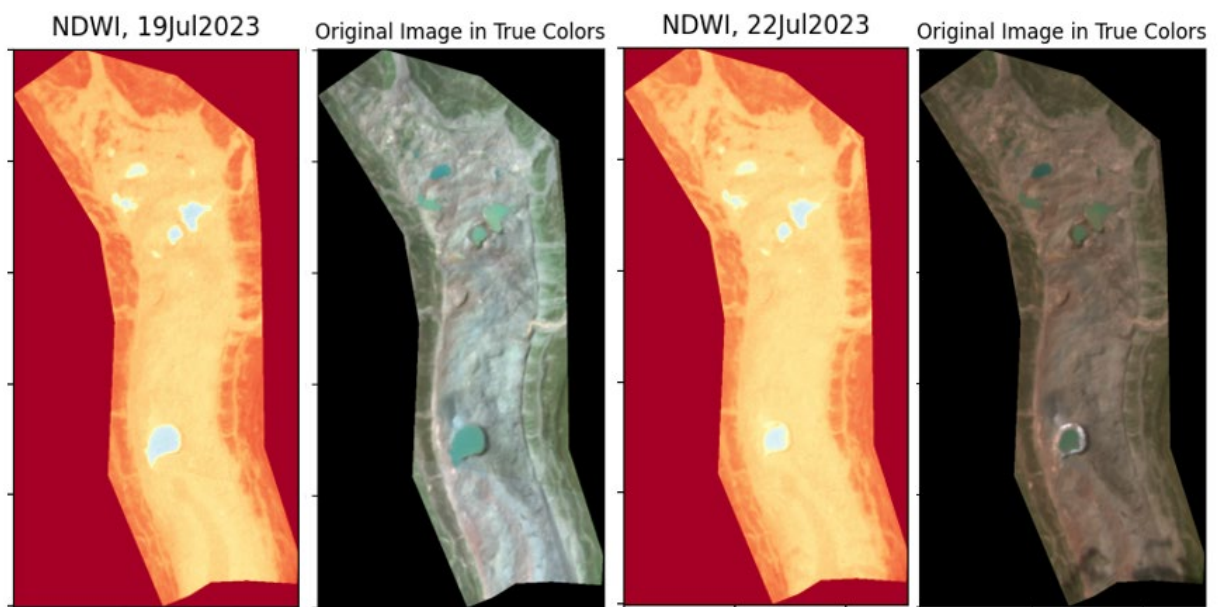


Figure 32. Sequence of NDWI and true-color imagery illustrating the 2023 drainage event on Baralmos Glacier. The images show how the pond areas changed between July 19 and July 22, 2023. The NDWI imagery shows a noticeable decrease in these ponds' area by July 22—pixel resolution: 3x3 meters per pixel.

For 2024, a major drainage event most likely took place between June 27 and July 3, with additional area loss continuing until July 7 (Figure 33). Unfortunately, earlier satellite imagery from June could not be analyzed due to extensive cloud cover, which limits our ability to observe lake growth dynamics before the event.

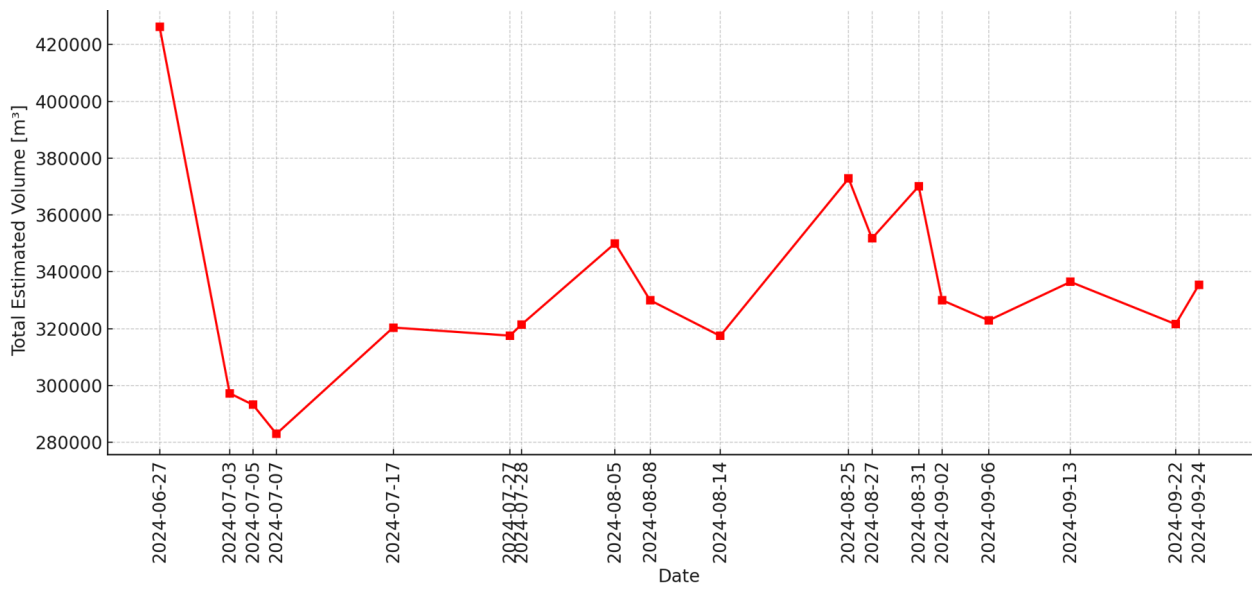


Figure 33. Total pond volumes over time (2024) based on a formula from Watson et al., 2017.

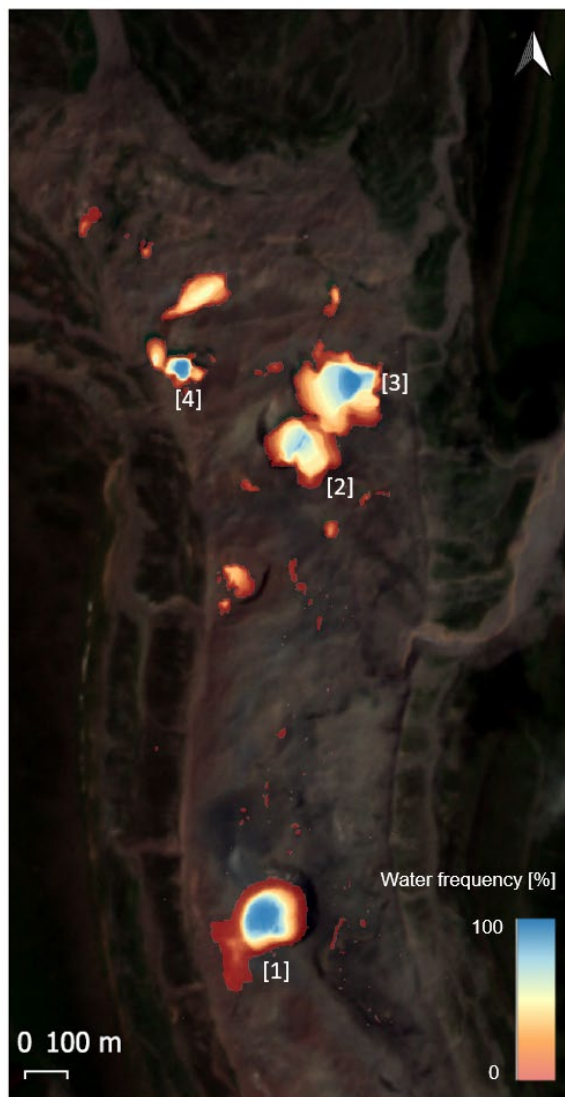


Figure 34. Lake-frequency map across the Baralmos glacier (2017-2024) with locations of further analyzed ponds ([1], [2], [3], and [4]). On leeward slopes, a few outlier pixels resemble windblown snow, which, however, don't make a difference.

The map of supraglacial pond frequency on Baralmos Glacier, which was created by analyzing NDWI from satellite images obtained between 2017 and 2024, is displayed in Figure 34. The gradient represents the proportion of the entire period in which each pixel was categorized as water. Orange and red regions represent locations with low water frequency, whereas blue regions reveal areas with a high water frequency value. The high-frequency regions line up with supraglacial ponds that, over multiple years, appear in similar locations, indicating stable depressions in the glacier surface. For instance, pond [1] appears to be consistently larger and subject to higher variability in area. We can also identify ponds [2] and [3], which in recent years (2022-2024) have begun to accumulate more water during the ablation period and therefore grow in size.

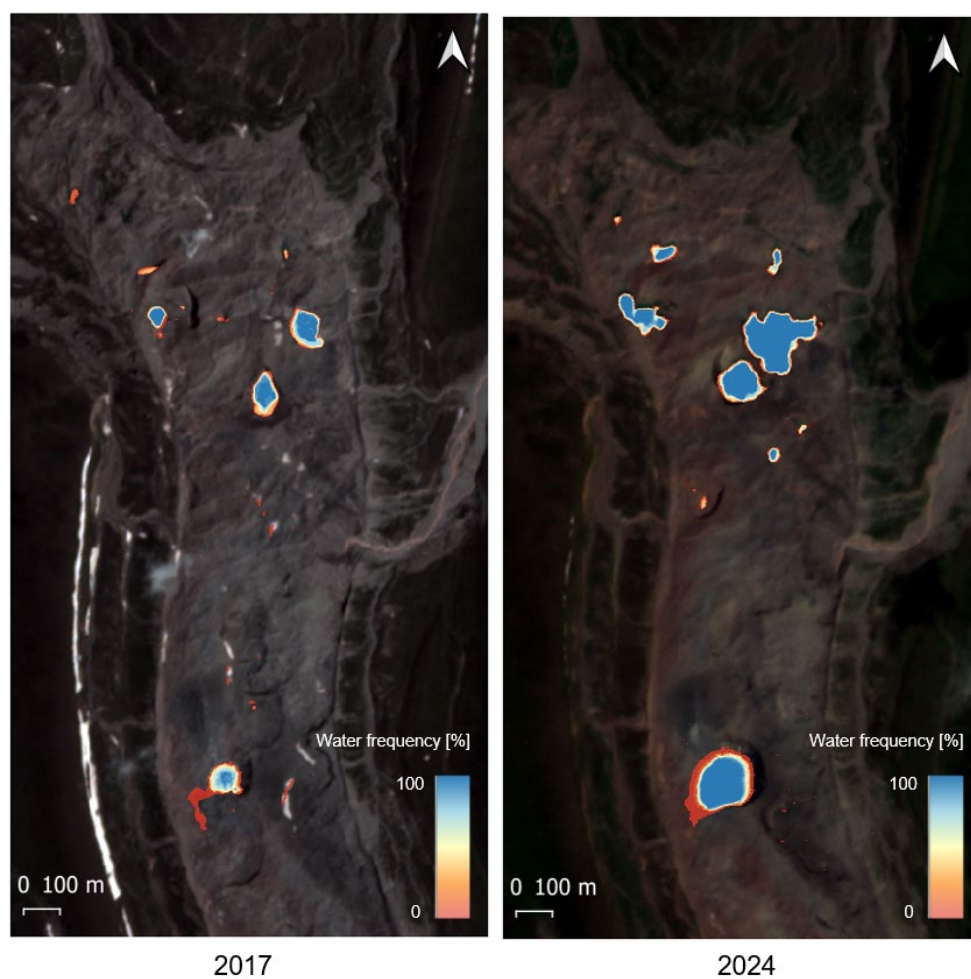


Figure 35. Lake-frequency maps across the Baralmos glacier for 2017 and 2024.

In addition to the lake-frequency map for the whole study period, comparative maps for 2017 and 2024 (Figure 35) were made, providing a visual representation of how water coverage on the glacier has evolved. 2017 water bodies were relatively small, but by 2024, the distribution and size of supraglacial ponds have changed. Pond [1], for instance, increased in area, as did the other ponds, which now appear more stable, as denoted by higher frequency indicators as their water

volume. The 2024 map shows changes in the configurations of the position of water bodies, with ponds located at different places and having a larger surface area than before.

5.1.2. Historical period

The analysis of Landsat data from the 1990s shows how the supraglacial pond areas on Baralmos Glacier have evolved over the years with respect to the 1998 surge event. Before the 1998 surge, the pond areas exceeded 150000 m² (Figures 36 and 37). However, the 1998 surge shown by the red line on the graph greatly decreased the total ponds area. This is likely because the surge disturbed the glacier surface, causing existing ponds to drain or disappear.

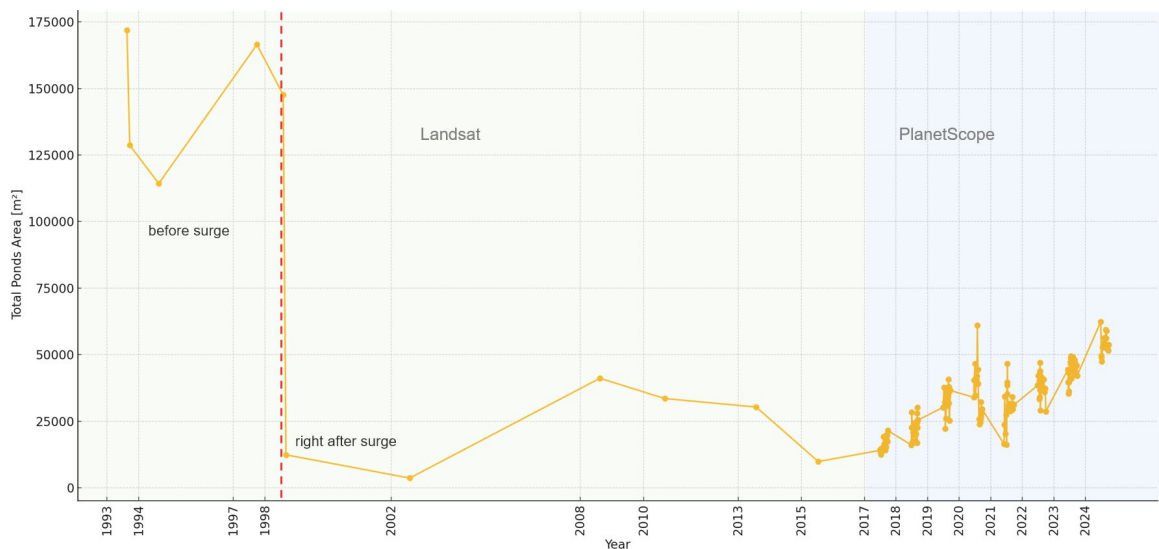


Figure 36. Long-term evolution of supraglacial pond areas on Baralmos glacier based on Landsat and PlanetScope data.

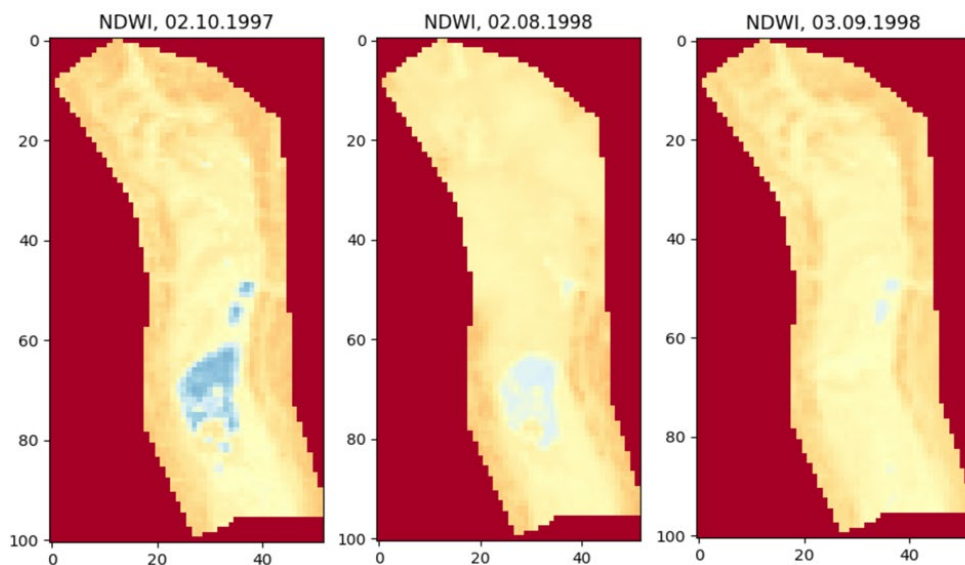


Figure 37. Baralmos glacier before (1 and 2) and after (3) the surge. The surge event leads to significant drainage and disappearance of main water bodies by September 1998—pixel resolution: 30x30 meters per pixel.

The analysis of historical data shows that the main problematic pond in recent years (Pond [1]) occupies a similar position on the glacier as the one before the 1998 surge. After the surge event, some pond areas recovered; however, they did not reach the size before the event.

5.1.3. Kyzylsu glacier

The information gathered from the analysis of satellite photos of the Kyzylsu glacier was also processed during the course of this research. Received data illustrate the spatial dynamics of supraglacial ponds, with the largest pond observable on June 11, 2023, covering an area of approximately 43,587 m². However, by June 19, the total pond area decreased dramatically to 7,146 m² (Figure 38), corresponding to an estimated volume reduction from 362,904 m³ to 19,799 m³ (see Table 3). By late June and July 2023, the total pond area further declined, reaching a minimum of just 936 m² on July 11, with an estimated volume of 2,071 m³.

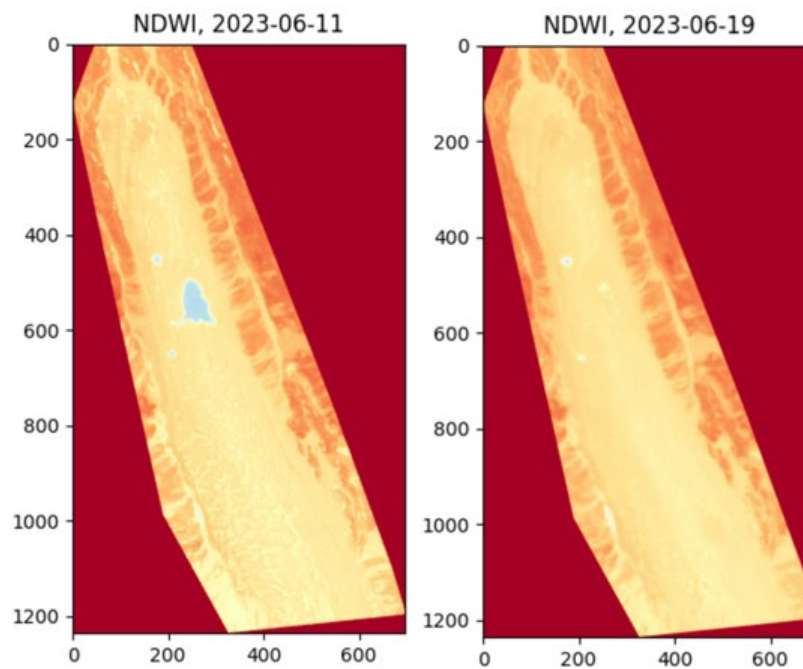


Figure 38. Sequence of NDWI imagery illustrating the 2023 drainage event, Kyzylsu glacier. The main supraglacial pond can be detected on the 11th of June, but it disappears by June 19—pixel resolution: 3x3 meters per pixel.

In the following year (2024), the total pond area for May was 24,053 m² (151,007 m³ volume), which grew to a peak of 36,684 m² by June 15 (297,583 m³). However, similar to 2023, a drainage event was observed in late June. In August and early September 2024, the total pond area stabilized at smaller extents, typically under 3,000 m², with estimated volumes remaining below 10,000 m³.

The Kyzylsu Glacier's patterns align closely with those observed at Baralmos glacier, suggesting regional-scale similarities in hydrological behavior.

5.1.4. Interconnectivity of pond areas changes

The interconnectivity of supraglacial ponds plays a crucial role in understanding their hydrological dynamics. While some ponds may act as isolated water bodies, others show signs of water redistribution, particularly during significant drainage events. This section examines the extent of interconnectivity between ponds from 2017 to 2024, assessing whether pond drainage is localized or system-wide.

The individual ponds showed variability during the study period. After quantifying the area changes for major events and producing stacked charts for visualization, it became clear that the system driver is the pond [1], which dominantly showed the greatest fluctuations. Quantitatively, 69% of major drainage events involved multiple ponds, suggesting some degree of system-wide interconnectivity. This suggests that when Pond [1] drains, it often triggers water loss in the lower ponds as well, rather than redistributing water among them.

Water redistribution from the pond [1] to the lower ponds was only observed in 2017, 2019, and weakly in 2023, while in 2020–2024, only ~18% of main drainage events showed signs of water redistribution. Recent years show a predominance of system-wide drainage rather than redistribution.

Now, I'll provide examples. In 2017-2018, it was pretty difficult to identify major drainage events, as the lake areas are quite small compared to recent years (as mentioned earlier in section 5.1.1). However, an interesting dynamic of water distribution between ponds is already present. For example, in the period from 08 August 2017 to 15 August 2017, the area of the pond [1] decreased significantly (-51%), while the area of lower ponds [2] and [3] increased (11 and 16%, respectively). This indicates that water from the upper pond may be partially redistributed to the lower ponds.

However, in 2018, during the main drainage event, there was no redistribution of water from the upper lake to the lower one. As for 2019, during the main drainage event in July, the upper pond was also unlikely to drain into the underlying ones. All the lakes have decreased in area. Interestingly, in the period 2017-2019, It was observed that water from the upper lake was often redistributed to the lower ones outside the main drains. For example, between September 1 and 2, 2019, the area of pond [1] decreased by 20 percent, while the areas of lakes [2] and [3] increased by 19 and 11, respectively.

In 2020, a major drainage event took place from July 29 to August 5, pond [1] experienced the greatest area shrinkage by 58.7%, from 14,706 m² to 6075 m². Ponds [1] and [2] experienced a shrinkage of 5.8% and 7.5%, and the pond [4] area decreased by 21%. It is important to note that further between August 8 and 17, the area of pond [1] did not change, when both ponds 2 and 3 experienced a decrease in area by 72 and 50 %, respectively.

In 2021, the pond [1] exhibited notable variability (Figure 39). The area of this lake on the 3rd of July, 2021 was 8343 m² and gradually went up to 22608 m² by the 11 July. This was followed by drainage to 10,197 m² by 17 July 2021 (percentage change of ~55%). Ponds [2] and [3] did not increase in their area, which could indicate the intake of water from pond [1], but on the contrary also drained, showing a decrease in area of 14% and 23%, respectively. Pond [4], as in 2020, showed minimal fluctuations, reinforcing its isolated nature in 2021.

Repeating the trend, in 2022, pond [1] experienced a major drainage event from 25 July to 28 July (previously also mentioned in section 5.1.1), during which the pond [1] decreased in the area from 23913 m² to 9927 m² (~58,5%) (Figure 40). During these events, ponds [2], [3], and [4] did not increase in volume, but on the contrary, also drained.

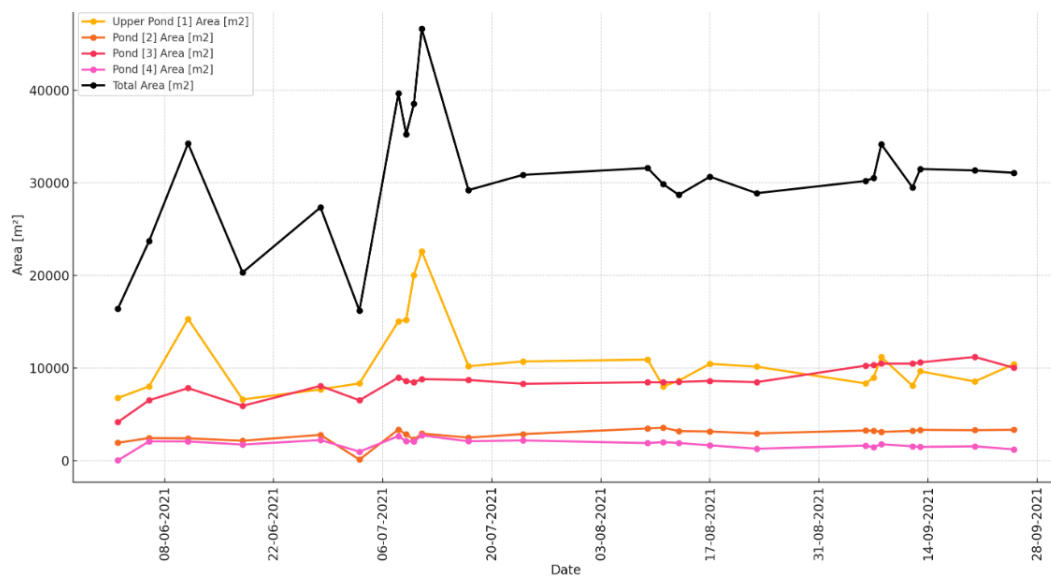


Figure 39. Separate pond areas and total pond area over time (2021). The black line represents the total area.

In 2023, there was a major drainage event in the pond [1] from 19 July to 22 July, when its area was lowered from 24,363 m² to 13,941 m², which stands for a ~ 42.8% reduction. Ponds [2] and [3] increased in area by ~5%, while pond [4] showed around a 10% area increase.

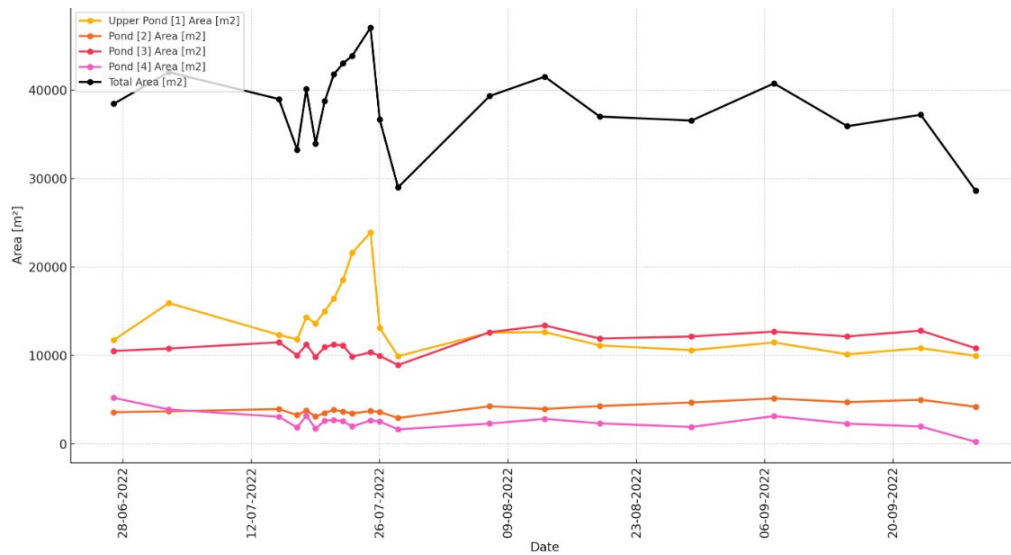


Figure 40. Separate pond areas and total pond area over time (2022). The black line represents the total area.

5.2. Drainage events and geomorphological changes

This results section examines whether there are clear signs of geomorphological changes associated with GLOF events in the study area. The analysis includes two parts: (1) an assessment of elevation differences based on DEMs and (2) a comparison study of satellite images taken before and after the major drainage events for 2022 to 2024 to look for changes in the debris flow fan and the stream channel.

The initial stage of this research objective work was related to the analysis of the DEM. After processing the DEM for 2022 and 2023, a residual elevation difference map was obtained (Figure 41).

After a close examination and analysis of the main drainage channels of the glacier for signs of erosion or accumulation of material, it was found that the main drainage channel (number 1, Figure 40) for the pond [1] shows practically no significant changes in height, which indicates the relative stability of its geomorphological structure. In contrast, the channel down the valley shows a mix of material deposition (indicated by areas of elevation gain, shown in red) and erosion (indicated by areas of elevation loss, shown in blue) (number 2, Figure 40). Erosional areas are indicative of the zones from where flowing water has eroded the sediments whereas depositional features are evidence of the sediments being transported and placed at further locations downstream. A zoomed-in view of the area was analyzed in detail to clarify the geomorphological changes in this channel (Figure 42). In this focused image, red zones show an increase in elevation, with changes up to +4 meters, and blue zones show a reduction in elevation, with changes reaching up to -4 meters.

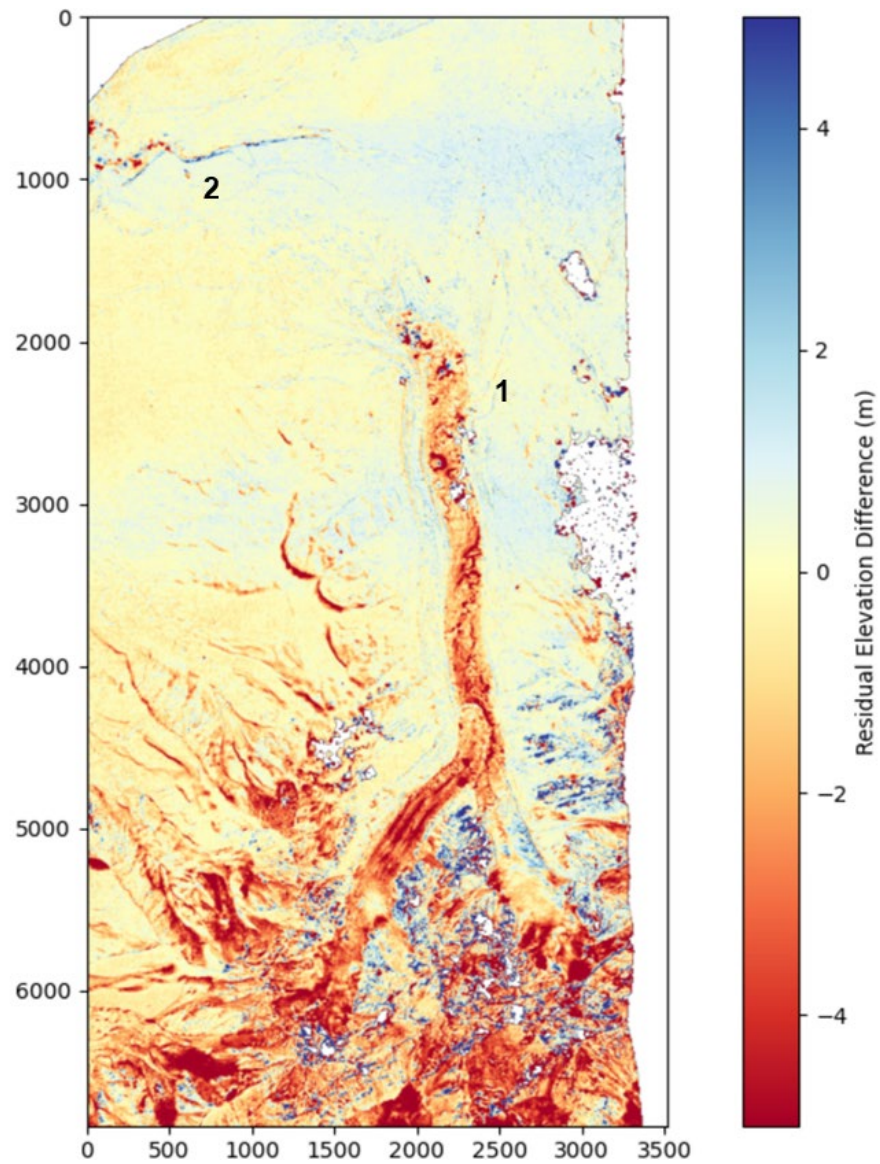


Figure 41. Elevation difference picture obtained after DEM-correction, based on Pleiades DEMs for 2022-2023. (1) main drainage channel from pond [1]; (2) channel further down the valley, where we can see elevation differences

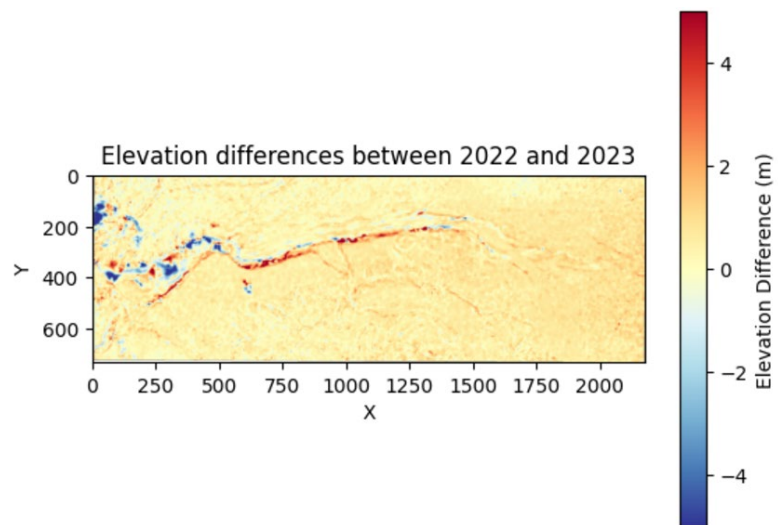


Figure 42. Elevation differences along the drainage channel down the valley between 2022 and 2023, showing areas of erosion (blue) and deposition (red) derived from DEM analysis.

The second part of the analysis for Research Objective 3 included a visual examination of high-resolution PlanetScope satellite images with a focus on signs of erosion and deposition before and after major outburst events in 2022-2024, as well as overall dynamics for the recent period.

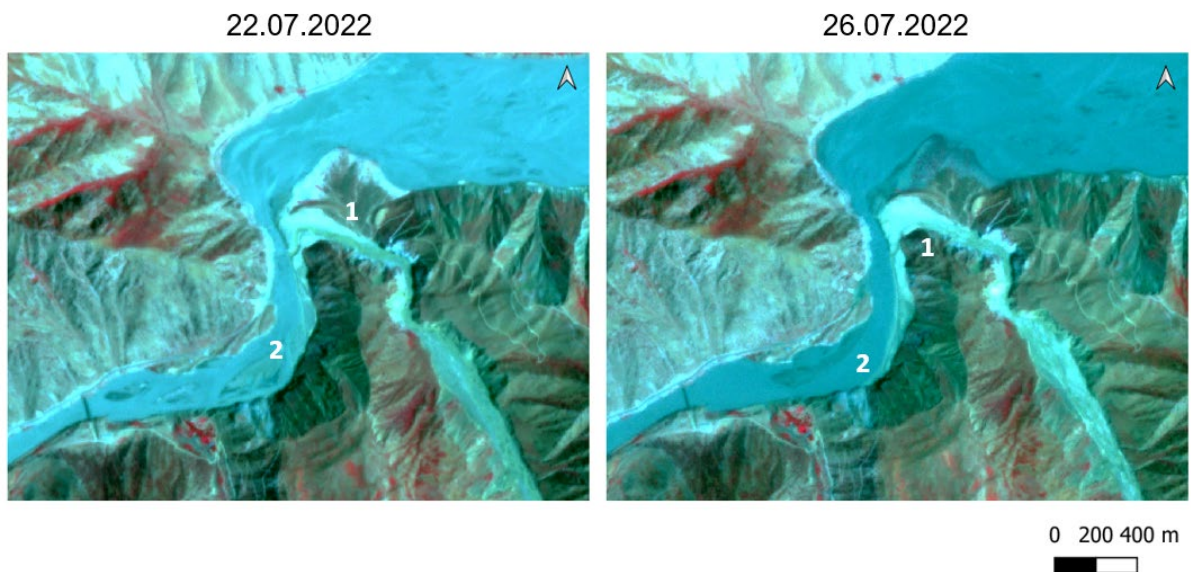


Figure 43. PlanetScope satellite images in pseudo-colors before (22.07.2022) and after (26.07.2022) the outburst event.

Most prominent changes are observed at the confluence of the river running from the Baralmos glacier into the Surkhob (Vakhsh) River. Significant changes in the landscape can be observed on the satellite images in pseudo-colors before and after the outburst events. For example, in the images for 2022 and 2023 (Figures 43 and 44), the mudflow cone at the confluence appears flooded in the post-event image, indicating the impact of increased water flow.

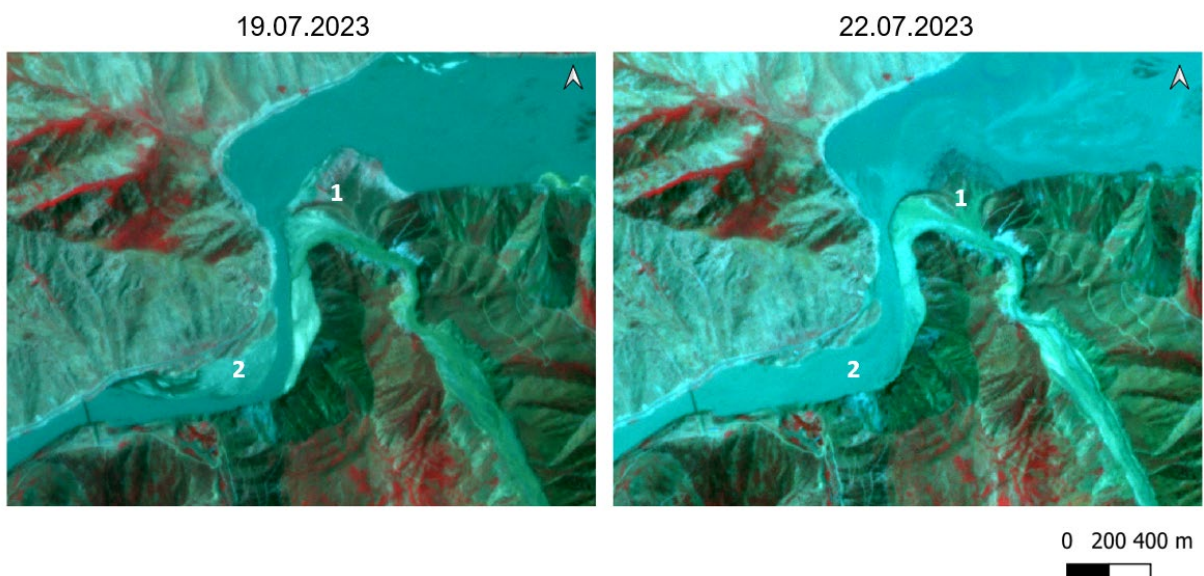


Figure 44. PlanetScope satellite images in pseudo-colors before (19.07.2023) and after (22.07.2023) the outburst event. (1) Flooded mudflow cone and new material deposition; (2) flooded Surkhob River.

In the Baralmos field report (September 2023), within the framework of the GLOFCA project, the transit and accumulation zones of the debris flow basin were studied (Figure 45). The report says that the walls of the gorge are mainly composed of loose rock, which causes instability and constant landslides. It gives solid material for the debris flow. According to the representative of the Emergency Department of the Lyakhsh district, the valley slopes have been increasingly eroding in recent years. It was pointed out that there are some areas where vegetation, including shrubs and thickets, has completely disappeared.



Figure 45. Debris flow deposition area (Baralmos Field Report, 2023), which can also be identified on satellite images.

It is important to mention that there are no notable morphological changes upstream (nearer the glacier tongue), suggesting that the area is rather stable. At the same time, within the main drainage stream channel, after outburst events, there is an observed increase in water flow (Figure 46), which can be explained by higher discharge levels caused by the outburst event.

To visually assess geomorphological transformations, satellite images from 2017 and 2024 were analyzed in regions exhibiting the most pronounced topographic changes, as identified in the DEM analysis. The visual comparison (Figures 47 and 48) highlights significant morphological alterations. Over the years, the debris flow transit channel has experienced substantial widening, with its walls receding by at least 20 meters.

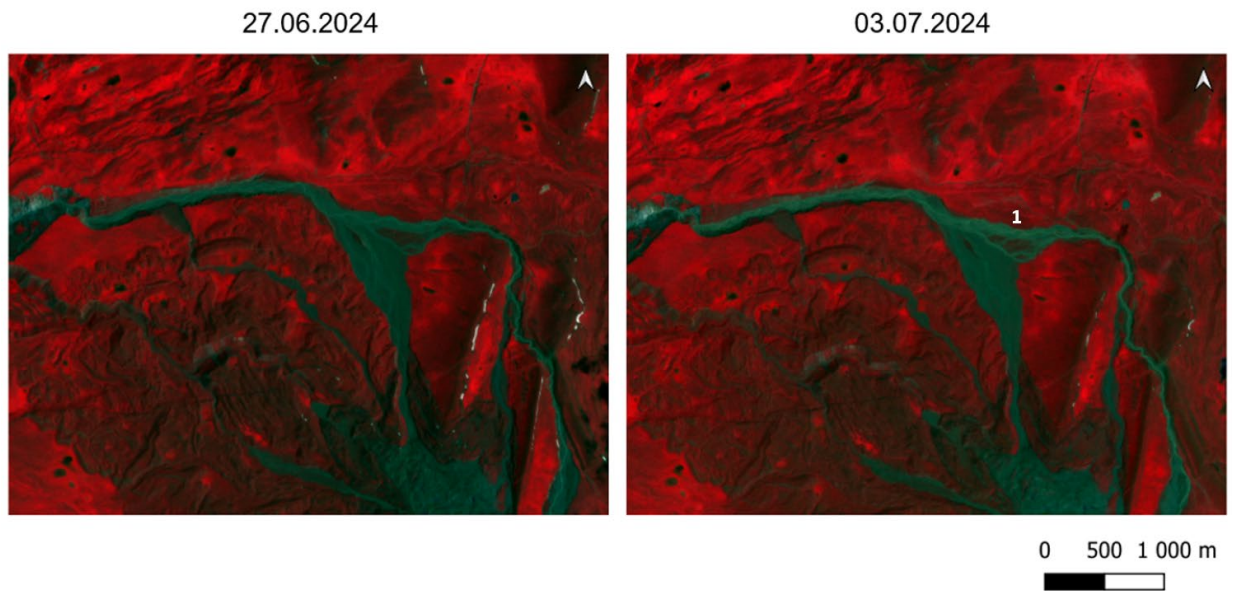


Figure 46. PlanetScope satellite images in pseudo-colors before (27.06.2024) and after (03.07.2024) the outburst event. **(1)** An increased water flow through the channel.

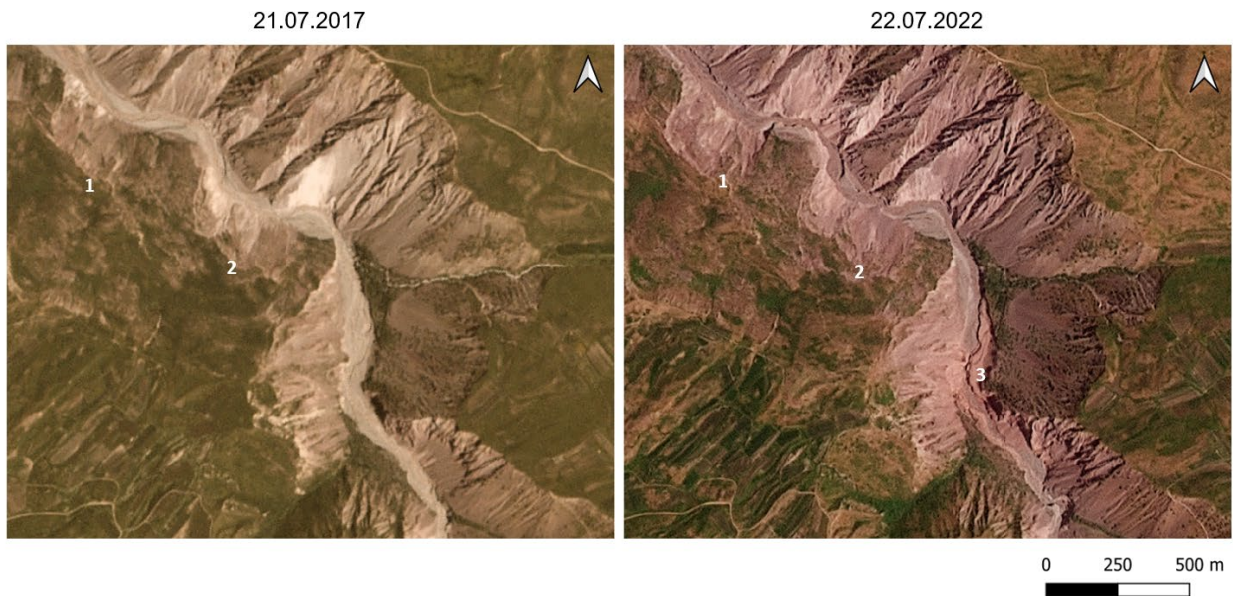


Figure 47. PlanetScope satellite images (natural colors) in 2017 and 2024. **(1)** and **(2)** channel slopes erosion; **(3)** sediment deposition

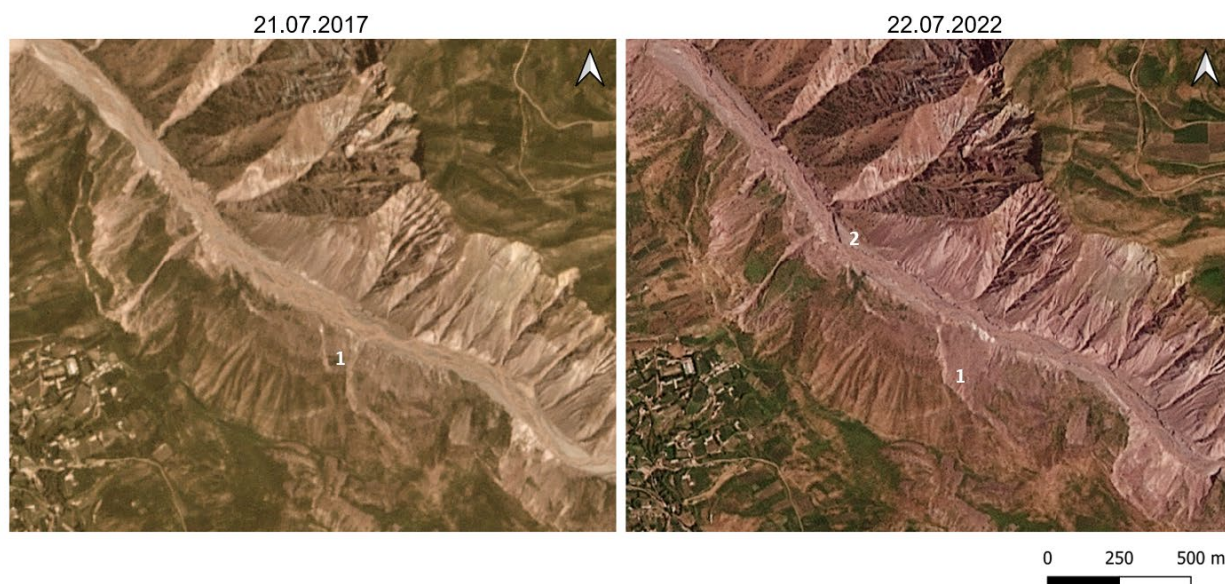


Figure 48. PlanetScope satellite images (natural colors) in 2017 and 2024. (1) channel slope erosion; (2) sediment deposition

Combined DEM and visual analysis show that major glacier lake outburst floods can cause geomorphological changes in the study area valley. While the main drainage channel from the glacier appears to be geomorphologically stable, the downstream valley consistently exhibits significant changes. This demonstrates that water from drainage events primarily affects distant, flatter areas where sediment is deposited after being mobilized from upstream.

6. Discussion

Results obtained during this work reveal important information about the Baralimos Glacier supraglacial pond's dynamic. In this chapter, I will try to discuss these findings in relation to the study's objectives, explore the limitations of the methods and data, and reflect on the broader implications of this research.

What is the frequency and size of pond drainages observed in satellite imagery during the recent period (2017–2024)? How do the recent surface water storage areas compare to those from the historical period (1990–present)?

The area and volume of the supraglacial ponds are increasing with time. The glacier's ability to store surface water has risen steadily, according to observations made between 2017 and 2024. The total supraglacial pond area increased by 42%. Estimated pond volumes rose from an average of 50,000 m³ in 2017 to approximately 90,000 m³ in recent years. This trend is consistent with previous studies that note glacial lake growth caused by increased ablation during warmer summer months and decreased December precipitation (Safarov et al., 2024).

Also, the data obtained show that the drainage of supraglacial lakes on the Baralimos glacier occurs mainly during the ablation season, with peak activity occurring in July and August. This pattern is consistent with seasonal snowmelt and temperature-dependent hydrological factors. The most significant outburst events, such as the one in 2023, caused marked reductions in pond areas and volumes. Specifically, between July 19 and July 22, 2023, the estimated volume of ponds decreased from 310,118 m³ to 221,050 m³.

The comparison of recent data (2017-2024) and historical data shows how drastically the Baralimos Glacier surface hydrology changed after the 1998 surge event. Before the surge, the pond areas were over 150,000 m² but drained and disrupted throughout the event. Over time, similar depressions on the glacier surface have been refilled with water, indicating the persistence of surface morphology despite periodic disruptions. By 2024, the volumetric and areal expanse of the ponds had greatly increased relative to the duration immediately post-surge. This may indicate the continued expansion of water storage capacity due to the retreating and thinning of glaciers.

These findings are consistent with recent studies, which highlighted the growth of glacial lakes in response to climate change across HMA (Bolch et al., 2012; Fujita and Nuimura, 2011; Shugar et al., 2020; Wang et al., 2020). The growth of certain supraglacial ponds can also be considered a self-reinforcing process of glacier movement and hydrological storage. As Kotlyakov et al. (2021)

noted, the surging behavior seems to periodically reset the surface features, while inter-surge periods enable the gradual formation of ponds. Nanni et al. (2023) provide additional context by looking at the seasonal velocity fluctuations of Pamir glaciers. Results showed that supraglacial pond drainage events directly impacted the hydrological conditions below the glacier and can be a reason for the seasonal or interannual changes in the glacier movement. As an example, the spring/summer accelerations and autumnal velocity increases on Pamir glaciers correlate with meltwater supply and drainage events, which means that supraglacial ponds are major contributors to basal sliding and hydrological pressurization. In addition, this study highlights processes of supraglacial pond drainage and its potential role in the generation of local instabilities that may travel as kinematic waves similar to surges of low magnitude.

The Baralmos Glacier case can provide an opportunity to investigate how supraglacial hydrology affects glacier movement and related risks across the Pamir.

Are changes in pond water areas for major events interconnected, or do they occur independently of one another?

Further analysis revealed that while some drainage events appear independent, others show evidence of interconnectivity between ponds. I suggest that the hydrological pathways of Baralmos glacier are complex, including surface and subsurface drainage networks. Pond [1] acts as a primary driver of water redistribution or loss, significantly influencing the hydrological behavior of the supraglacial pond network. The results show that 69% of major drainage events involved multiple ponds, indicating system-wide interconnectivity. However, rather than redistributing water among the lower ponds, pond [1] often triggered simultaneous drainage in connected ponds.

The trend of pond interconnectivity evolved over time. Water redistribution from the pond [1] to the lower ponds was only clearly observed in 2017, 2019, and weakly in 2023. In contrast, in the period from 2020 to 2024, only ~18% of significant drainage events showed evidence of water redistribution. It is important to note that the hydrological systems of debris-covered glaciers, such as the Baralmos Glacier, differ from glacier systems with pure ice, which leads to a relatively limited understanding of the flow paths (Miles et al., 2017).

Are there clear signs of geomorphological changes linked to pond drainage events?

Geomorphological analysis using DEM data from 2022 to 2023, combined with satellite imagery, revealed substantial geomorphological transformations along drainage channels. Areas of erosion and sediment deposition were identified, highlighting the impact of pond drainage events on

downstream landscapes. Outburst events tend to cause some serious changes to the riverbanks, valley slopes, and vegetation. The analysis shows that, between 2022 and 2023, elevation differences along the primary drainage channel ranged from -4 m (erosion) to +4 m (deposition). These changes are consistent with observations in glaciated regions documenting similar geomorphic responses to GLOFs (Cenderelli and Wohl, 2003; Emmer, 2023). The impact of these changes extends beyond immediate geomorphological shifts, as they can alter future flood pathways and sediment transport regimes.

Limitations

The methodology used in this study provides a detailed analysis of supraglacial pond dynamics; however, several uncertainties and limitations must be acknowledged.

Cloud or snow coverage obscured the initial stages of pond activities occurring in May and June, making it impossible to ascertain the exact time of lake drainages. This problem could be solved by obtaining additional information from loggers. Pressure transducer and water temperature datasets were collected at Baralmos Glacier in 2021 for the pond [3] and captured a major drainage event in July. However, sensors that were installed in 2023 were later washed away.

NDWI-based water body detection has a number of drawbacks, such as missing small water bodies and being sensitive to cloud cover and snow contamination. However, I addressed these challenges by implementing a structured processing workflow. Otsu's thresholding approach was applied to the calculated NDWI data to improve accuracy. Otsu's approach minimized the possibility of subjective bias and guaranteed consistency among datasets by automating the thresholding procedure. Additionally, iterative refinement techniques were developed to split the NDWI image into bounding boxes and update the NDWI value per region. This additional step greatly assisted in ensuring reliability in detecting small or partially obscured water bodies, making the final results more reliable.

Another limitation relates to the empirical methods used to estimate the volume, including scaling the area by volume. While these methods provide reasonable approximations, direct bathymetric measurements would improve accuracy. During the fieldwork in 2024, a bathymetry survey was conducted, and the results aligned well with the preliminary data. A detailed DEM-based analysis of the glacier's closed surface catchments (Miles et al., 2017) can also be performed to identify surface drainage pathways and englacial drainage points.

All DEMs inherently contain some level of horizontal and vertical geolocation error, which can introduce biases in elevation measurements and affect interpretations of geomorphological changes. It is crucial to remove relative offsets when differencing DEMs for elevation change analyses, as failing to do so may result in overestimations or underestimations of erosion and sediment deposition. I applied a co-registration correction to address this issue by aligning the DEMs with stable terrain features.

Social impacts and further work opportunities

The impact of GLOFs extends beyond hydrological and geomorphological processes, affecting infrastructure and local communities. While no villages are impacted by floods from Baralmos Glacier, a major event comparable to the 1998 surge could have severe consequences. Recent events, such as the destruction of the Surkhob River bridge and road closures in 2023, underscore the vulnerability of key transportation routes. A more extreme flood could lead to substantial sediment deposition, making transportation impossible for weeks or months. Such an event could also result in prolonged riverbed aggradation, raising the Surkhob River stage and altering downstream hydrology. These changes might increase the risk of future flooding. Economic and social disruption is another potential consequence, with frequent road closures limiting access to markets, emergency services, and essential goods. Prolonged disruptions could necessitate community relocation or contribute to regional economic decline.

This study presents opportunities for further work. The development of the Early Warning System (EWS) for the Baralmos Glacier using the data obtained during this work can help mitigate the risk of GLOFs. For example, the monitoring systems in Nepal offer a model for integrating real-time water level sensors with satellite monitoring and community-based alert mechanisms (Smith et al., 2017). A similar system adapted for the study area and similar regions could enhance local disaster preparedness. Another great chance is the possibility of better monitoring surges. Using systems for tracking velocity (for example, SAR offset-tracking methods) (Strozzi et al., 2002), together with high-resolution images, can significantly improve the understanding of surge triggers with the dynamics of supraglacial ponds. Moreover, making interregional comparisons with other surge-type glaciers of the Pamirs, like the Kyzylsu Glacier, may uncover additional features and enhance the understanding of glacier behavior in the context of climate warming.

7. Conclusion

This Master's thesis investigates the dynamics and threats of glacial lake outburst floods (GLOFs) from the Baralmos Glacier in Tajikistan. The research enables an understanding of supraglacial ponds' evolution, drainage processes, and consequential geomorphological phenomena using the PlanetScope and historical Landsat imagery together with Pleiades DEMs geomorphological analysis. The study's findings contribute to the body of knowledge regarding glacial lake dynamics and the need for better hazard mitigation planning for high mountain regions.

A historical perspective reveals that supraglacial pond coverage was significantly higher in the early 1990s, with peak values exceeding 150,000 m². However, the 1998 surge event drastically decreased stored surface water, leading to rapid drainage and a near-total disappearance of supraglacial lakes. The 1998 surge event did not permanently eliminate supraglacial pond formation. The analysis revealed significant temporal trends in pond area and volume, with notable increases observed over the recent period (2017–2024). There is a 42% increase in total supraglacial pond area between 2017 and 2024, accompanied by an estimated rise in pond volumes from 50,000 m³ in 2017 to approximately 90,000 m³ in recent years.

Crucially, this research demonstrates the increasing complexity of supraglacial pond systems, with evidence of interconnectivity between ponds during some drainage events, suggesting hydrological interactions within the glacier. While the surge initially reduced supraglacial pond areas, the long-term trend shows that pond formation resumed. This suggests that surges may act as temporary resets but do not eliminate future GLOF risks.

Analysis of Pleiades DEMs from 2022 to 2023 reveals substantial geomorphological changes along drainage pathways. The dynamic reconfiguration of the glacier's hydrological system is demonstrated by the elevation changes along the principal drainage channel, which range from -4 meters (erosion) to +4 meters (sediment deposition). Additionally, the walls of the debris flow transit channel have receded by at least 20 meters over time, indicating increasing channel degradation brought on by frequent outburst episodes. Further evidence of the movement of substantial amounts of debris is provided by sediment deposition in downstream areas, which supports the idea that GLOFs alter the shape of valley floors and raise the risk of flooding downstream.

These results are essential for comprehending the downstream effects of GLOFs, which present significant threats to residents and infrastructure. For example, the Baralmos Glacier has been connected to several damaging outburst episodes in recent years, which have caused dammed river

channels and destroyed roads. These incidents' recurrent nature emphasizes the necessity of ongoing observation and the creation of efficient early warning systems.

Along with its scientific discoveries, this thesis emphasizes the practical applications of understanding GLOF dynamics. The approaches used – such as NDWI-based water body recognition, area-volume scaling, and DEM analysis – provide a solid foundation for analyzing GLOF dangers in similar high-mountain situations. These methods can help identify areas of vulnerability and anticipate flood magnitude. Furthermore, the study emphasizes combining high-resolution remote sensing data with field-based observations to capture the fast-paced and frequently unpredictable nature of glacial lake dynamics. In terms of new measures, this research seeks to promote investment in monitoring systems and community-based disaster preparedness initiatives in GLOF-prone regions. The findings also emphasize the importance of interdisciplinary collaboration among scientists, policymakers, and local stakeholders in developing adaptive solutions to the immediate and long-term difficulties posed by GLOFs. The lessons learned from the Baralmos Glacier can be a useful guide for managing glacial dangers in other high-mountain regions worldwide as global temperatures continue to rise.

8. References

- Ahmed, R., 2024. Glacial Lake Outburst Flood (GLOF) Hazard and Risk Management Strategies: A Global Overview. *Water Resour Manage*. <https://doi.org/10.1007/s11269-024-03958-x>
- Allan, Nigel John Roger and Zakharova, Tatyana Konstantinovna. "Pamirs". *Encyclopedia Britannica*, 21 Sep. 2024, <https://www.britannica.com/place/Pamirs>. Accessed 1 October 2024., n.d.
- Allen, S.K., Rastner, P., Arora, M., Huggel, C., Stoffel, M., 2016. Lake outburst and debris flow disaster at Kedarnath, June 2013: hydrometeorological triggering and topographic predisposition. *Landslides* 13, 1479–1491. <https://doi.org/10.1007/s10346-015-0584-3>
- Allen, S.K., Sattar, A., King, O., Zhang, G., Bhattacharya, A., Yao, T., Bolch, T., 2022. Glacial lake outburst flood hazard under current and future conditions: worst-case scenarios in a transboundary Himalayan basin. *Nat. Hazards Earth Syst. Sci.* 22, 3765–3785. <https://doi.org/10.5194/nhess-22-3765-2022>
- Bajracharya, S.R., Mool, P., 2009. Glaciers, glacial lakes and glacial lake outburst floods in the Mount Everest region, Nepal. *Ann. Glaciol.* 50, 81–86. <https://doi.org/10.3189/172756410790595895>
- Baralimos Field Report, 2023. . Dushanbe, Tajikistan.
- Barandun, M., Fiddes, J., Scherler, M., Mathys, T., Saks, T., Petrakov, D., Hoelzle, M., 2020. The state and future of the cryosphere in Central Asia. *Water Security* 11, 100072. <https://doi.org/10.1016/j.wasec.2020.100072>
- Bazai, N.A., Cui, P., Carling, P.A., Wang, H., Hassan, J., Liu, D., Zhang, G., Jin, W., 2021. Increasing glacial lake outburst flood hazard in response to surge glaciers in the Karakoram. *Earth-Science Reviews* 212, 103432. <https://doi.org/10.1016/j.earscirev.2020.103432>
- Bhambri, R., Hewitt, K., Kawishwar, P., Kumar, A., Verma, A., Snehmani, Tiwari, S., Misra, A., 2019. Ice-dams, outburst floods, and movement heterogeneity of glaciers, Karakoram. *Global and Planetary Change* 180, 100–116. <https://doi.org/10.1016/j.gloplacha.2019.05.004>
- Bolch, T., Buchroithner, M.F., Peters, J., Baessler, M., Bajracharya, S., 2008. Identification of glacier motion and potentially dangerous glacial lakes in the Mt. Everest region/Nepal using spaceborne imagery. *Nat. Hazards Earth Syst. Sci.* 8, 1329–1340. <https://doi.org/10.5194/nhess-8-1329-2008>
- Bolch, T., Peters, J., Yegorov, A., Pradhan, B., Buchroithner, M., Blagoveshchensky, V., 2012. Identification of Potentially Dangerous Glacial Lakes in the Northern Tian Shan, in: Pradhan, B., Buchroithner, M. (Eds.), *Terrigenous Mass Movements*. Springer Berlin Heidelberg, Berlin, Heidelberg, pp. 369–398. https://doi.org/10.1007/978-3-642-25495-6_12
- Byers, A.C., McKinney, D.C., Somos-Valenzuela, M., Watanabe, T., Lamsal, D., 2013. Glacial lakes of the Hinku and Hongu valleys, Makalu Barun National Park, and Buffer Zone, Nepal. *Nat Hazards* 69, 115–139. <https://doi.org/10.1007/s11069-013-0689-8>
- Carey, M., 2008. Disasters, Development, and Glacial Lake Control in Twentieth-Century Peru, in: Wiegandt, E. (Ed.), *Mountains: Sources of Water, Sources of Knowledge*. Springer Netherlands, Dordrecht, pp. 181–196. https://doi.org/10.1007/978-1-4020-6748-8_11

- Carey, M., Huggel, C., Bury, J., Portocarrero, C., Haeberli, W., 2012. An integrated socio-environmental framework for glacier hazard management and climate change adaptation: lessons from Lake 513, Cordillera Blanca, Peru. *Climatic Change* 112, 733–767. <https://doi.org/10.1007/s10584-011-0249-8>
- Carrivick, J.L., Tweed, F.S., 2016. A global assessment of the societal impacts of glacier outburst floods. *Global and Planetary Change* 144, 1–16. <https://doi.org/10.1016/j.gloplacha.2016.07.001>
- Carrivick, J.L., Tweed, F.S., 2013. Proglacial lakes: character, behaviour and geological importance. *Quaternary Science Reviews* 78, 34–52. <https://doi.org/10.1016/j.quascirev.2013.07.028>
- Catalogue of Glaciers of the USSR, 1978. . Hydrometeoizdat: Leningrad.
- Cenderelli, D.A., Wohl, E.E., 2003. Flow hydraulics and geomorphic effects of glacial-lake outburst floods in the Mount Everest region, Nepal. *Earth Surf Processes Landf* 28, 385–407. <https://doi.org/10.1002/esp.448>
- Cooley, S., Smith, L., Stepan, L., Mascaro, J., 2017. Tracking Dynamic Northern Surface Water Changes with High-Frequency Planet CubeSat Imagery. *Remote Sensing* 9, 1306. <https://doi.org/10.3390/rs9121306>
- Costa, J.E., Schuster, R.L., 1987. The formation and failure of natural dams (Report No. 87–392), Open-File Report. <https://doi.org/10.3133/ofr87392>
- Cui, P., Dang, C., Cheng, Z., Scott, K.M., 2010. Debris Flows Resulting From Glacial-Lake Outburst Floods in Tibet, China. *Physical Geography* 31, 508–527. <https://doi.org/10.2747/0272-3646.31.6.508>
- Daiyrov, M., Narama, C., 2021. Formation, evolution, and drainage of short-lived glacial lakes in permafrost environments of the northern Teskey Range, Central Asia. *Nat. Hazards Earth Syst. Sci.* 21, 2245–2256. <https://doi.org/10.5194/nhess-21-2245-2021>
- Emmer, A., 2023. Vanishing evidence? On the longevity of geomorphic GLOF diagnostic features in the Tropical Andes. *Geomorphology* 422, 108552. <https://doi.org/10.1016/j.geomorph.2022.108552>
- Emmer, A., 2018. GLOFs in the WOS: bibliometrics, geographies and global trends of research on glacial lake outburst floods (Web of Science, 1979–2016). *Nat. Hazards Earth Syst. Sci.* 18, 813–827. <https://doi.org/10.5194/nhess-18-813-2018>
- Emmer, A., Allen, S.K., Carey, M., Frey, H., Huggel, C., Korup, O., Mergili, M., Sattar, A., Veh, G., Chen, T.Y., Cook, S.J., Correas-Gonzalez, M., Das, S., Diaz Moreno, A., Drenkhan, F., Fischer, M., Immerzeel, W.W., Izagirre, E., Joshi, R.C., Kougkoulos, I., Kuyakanon Knapp, R., Li, D., Majeed, U., Matti, S., Moulton, H., Nick, F., Piroton, V., Rashid, I., Reza, M., Ribeiro De Figueiredo, A., Riveros, C., Shrestha, F., Shrestha, M., Steiner, J., Walker-Crawford, N., Wood, J.L., Yde, J.C., 2022a. Progress and challenges in glacial lake outburst flood research (2017–2021): a research community perspective. *Nat. Hazards Earth Syst. Sci.* 22, 3041–3061. <https://doi.org/10.5194/nhess-22-3041-2022>

- Emmer, A., Klimeš, J., Mergili, M., Vilímek, V., Cochachin, A., 2016. 882 lakes of the Cordillera Blanca: An inventory, classification, evolution and assessment of susceptibility to outburst floods. *CATENA* 147, 269–279. <https://doi.org/10.1016/j.catena.2016.07.032>
- Emmer, A., Wood, J.L., Cook, S.J., Harrison, S., Wilson, R., Diaz-Moreno, A., Reynolds, J.M., Torres, J.C., Yarleque, C., Mergili, M., Jara, H.W., Bennett, G., Caballero, A., Glasser, N.F., Melgarejo, E., Riveros, C., Shannon, S., Turpo, E., Tinoco, T., Torres, L., Garay, D., Villafane, H., Garrido, H., Martinez, C., Apaza, N., Araujo, J., Poma, C., 2022b. 160 glacial lake outburst floods (GLOFs) across the Tropical Andes since the Little Ice Age. *Global and Planetary Change* 208, 103722. <https://doi.org/10.1016/j.gloplacha.2021.103722>
- Erokhin, S.A., Zaginaev, V.V., 2017. Lithology of Debris-Forming Deposits. *Central Asian Journal of Water Research (CAJWR)* 3, 1901.
- Erokhin, S.A., Zaginaev, V.V., Meleshko, A.A., Ruiz-Villanueva, V., Petrakov, D.A., Chernomorets, S.S., Viskhadzhieva, K.S., Tutubalina, O.V., Stoffel, M., 2018. Debris flows triggered from non-stationary glacier lake outbursts: the case of the Teztor Lake complex (Northern Tian Shan, Kyrgyzstan). *Landslides* 15, 83–98. <https://doi.org/10.1007/s10346-017-0862-3>
- Evans, S.G., Clague, J.J., 1994. Recent climatic change and catastrophic geomorphic processes in mountain environments, in: *Geomorphology and Natural Hazards*. Elsevier, pp. 107–128. <https://doi.org/10.1016/B978-0-444-82012-9.50012-8>
- Falátková, K., 2016. Temporal analysis of GLOFs in high-mountain regions of Asia and assessment of their causes. *AUC GEOGRAPHICA* 51, 145–154. <https://doi.org/10.14712/23361980.2016.12>
- Frey, H., Haeberli, W., Linsbauer, A., Huggel, C., Paul, F., 2010. A multi-level strategy for anticipating future glacier lake formation and associated hazard potentials. *Nat. Hazards Earth Syst. Sci.* 10, 339–352. <https://doi.org/10.5194/nhess-10-339-2010>
- Fujita, K., 2008. Effect of precipitation seasonality on climatic sensitivity of glacier mass balance. *Earth and Planetary Science Letters* 276, 14–19. <https://doi.org/10.1016/j.epsl.2008.08.028>
- Fujita, K., Nuimura, T., 2011. Spatially heterogeneous wastage of Himalayan glaciers. *Proc. Natl. Acad. Sci. U.S.A.* 108, 14011–14014. <https://doi.org/10.1073/pnas.1106242108>
- Furian, W., Loibl, D., Schneider, C., 2021. Future glacial lakes in High Mountain Asia: an inventory and assessment of hazard potential from surrounding slopes. *J. Glaciol.* 67, 653–670. <https://doi.org/10.1017/jog.2021.18>
- Guo, Q., Pu, R., Li, J., Cheng, J., 2017. A weighted normalized difference water index for water extraction using Landsat imagery. *International Journal of Remote Sensing* 38, 5430–5445. <https://doi.org/10.1080/01431161.2017.1341667>
- Hansen, M.C., Potapov, P.V., Moore, R., Hancher, M., Turubanova, S.A., Tyukavina, A., Thau, D., Stehman, S.V., Goetz, S.J., Loveland, T.R., Kommareddy, A., Egorov, A., Chini, L., Justice, C.O., Townshend, J.R.G., 2013. High-Resolution Global Maps of 21st-Century Forest Cover Change. *Science* 342, 850–853. <https://doi.org/10.1126/science.1244693>

- Haritashya, U.K., Bishop, M.P., Shroder, J.F., Bush, A.B.G., Bulley, H.N.N., 2009. Space-based assessment of glacier fluctuations in the Wakhan Pamir, Afghanistan. *Climatic Change* 94, 5–18. <https://doi.org/10.1007/s10584-009-9555-9>
- Harrison, S., Kargel, J.S., Huggel, C., Reynolds, J., Shugar, D.H., Betts, R.A., Emmer, A., Glasser, N., Haritashya, U.K., Klimeš, J., Reinhardt, L., Schaub, Y., Wiltshire, A., Regmi, D., Vilímek, V., 2018. Climate change and the global pattern of moraine-dammed glacial lake outburst floods. *The Cryosphere* 12, 1195–1209. <https://doi.org/10.5194/tc-12-1195-2018>
- Hock, R., Rasul, G., Adler, C., Cáceres, B., S. Gruber, Y. Hirabayashi, M. Jackson, A. Kääb, S. Kang, S. Kutuzov, Al. Milner, U. Molau, S. Morin, B. Orlove, and H. Steltzer, 2022. High Mountain Areas. In: *The Ocean and Cryosphere in a Changing Climate: Special Report of the Intergovernmental Panel on Climate Change*, 1st ed. Cambridge University Press. <https://doi.org/10.1017/9781009157964>
- Hu, Z., Zhang, C., Hu, Q., Tian, H., 2014. Temperature Changes in Central Asia from 1979 to 2011 Based on Multiple Datasets*. *Journal of Climate* 27, 1143–1167. <https://doi.org/10.1175/JCLI-D-13-00064.1>
- Huggel, C., Carey, M., Emmer, A., Frey, H., Walker-Crawford, N., Wallimann-Helmer, I., 2020. Anthropogenic climate change and glacier lake outburst flood risk: local and global drivers and responsibilities for the case of lake Palcacocha, Peru. *Nat. Hazards Earth Syst. Sci.* 20, 2175–2193. <https://doi.org/10.5194/nhess-20-2175-2020>
- Huggel, C., Haeberli, W., Kääb, A., Bieri, D., Richardson, S., 2004. An assessment procedure for glacial hazards in the Swiss Alps. *Can. Geotech. J.* 41, 1068–1083. <https://doi.org/10.1139/t04-053>
- Huggel, C., Kääb, A., Haeberli, W., Teyssiere, P., Paul, F., 2002. Remote sensing based assessment of hazards from glacier lake outbursts: a case study in the Swiss Alps. *Can. Geotech. J.* 39, 316–330. <https://doi.org/10.1139/t01-099>
- Iverson, R.M., 2012. Elementary theory of bed-sediment entrainment by debris flows and avalanches. *J. Geophys. Res.* 117, 2011JF002189. <https://doi.org/10.1029/2011JF002189>
- Jain, S.K., Lohani, A.K., Singh, R.D., Chaudhary, A., Thakural, L.N., 2012. Glacial lakes and glacial lake outburst flood in a Himalayan basin using remote sensing and GIS. *Nat Hazards* 62, 887–899. <https://doi.org/10.1007/s11069-012-0120-x>
- Jakob, M., Hungr, O., 2005. *Debris-flow Hazards and Related Phenomena*, Springer Praxis Books. Springer Berlin Heidelberg, Berlin, Heidelberg. <https://doi.org/10.1007/b138657>
- Jha, L.K., Khare, D., 2017. Detection and delineation of glacial lakes and identification of potentially dangerous lakes of Dhauliganga basin in the Himalaya by remote sensing techniques. *Nat Hazards* 85, 301–327. <https://doi.org/10.1007/s11069-016-2565-9>
- Khromova, T.E., Osipova, G.B., Tsvetkov, D.G., Dyurgerov, M.B., Barry, R.G., 2006. Changes in glacier extent in the eastern Pamir, Central Asia, determined from historical data and ASTER imagery. *Remote Sensing of Environment* 102, 24–32. <https://doi.org/10.1016/j.rse.2006.01.019>

- King, O., Turner, A.G.D., Quincey, D.J., Carrivick, J.L., 2020. Morphometric evolution of Everest region debris-covered glaciers. *Geomorphology* 371, 107422. <https://doi.org/10.1016/j.geomorph.2020.107422>
- Komori, J., 2008. Recent expansions of glacial lakes in the Bhutan Himalayas. *Quaternary International* 184, 177–186. <https://doi.org/10.1016/j.quaint.2007.09.012>
- Kotlyakov, V.M., Desinov, S.L., Desinov, L.V., Rudakov, V.A., 2021. Surges of the Pamir glaciers in 2020. *Ice and Snow* 61, 471–480. <https://doi.org/10.31857/S2076673421030102>
- Makhmadaliev, B., Kayumov, A., Novikov, V., Mustaeva, N., Rajabov, I., 2008. The Second National Communication of the Republic of Tajikistan under the United Nations Framework Convention on Climate Change. State Agency for Hydrometeorology, Dushanbe, Tajikistan.
- McFeeters, S.K., 1996. The use of the Normalized Difference Water Index (NDWI) in the delineation of open water features. *International Journal of Remote Sensing* 17, 1425–1432. <https://doi.org/10.1080/01431169608948714>
- Mergili, M., Pudasaini, S.P., Emmer, A., Fischer, J.-T., Cochachin, A., Frey, H., 2020. Reconstruction of the 1941 GLOF process chain at Lake Palcacocha (Cordillera Blanca, Peru). *Hydrol. Earth Syst. Sci.* 24, 93–114. <https://doi.org/10.5194/hess-24-93-2020>
- Mergili, M., Schneider, D., Worni, R., Schneider, J.F., 2011. Glacial Lake Outburst Floods in the Pamir of Tajikistan: challenges in prediction and modelling. *Italian Journal of Engineering Geology and Environment* 973–982. <https://doi.org/10.4408/IJEGE.2011-03.B-106>
- Mergili, M., Schneider, J.F., 2011. Regional-scale analysis of lake outburst hazards in the southwestern Pamir, Tajikistan, based on remote sensing and GIS. *Nat. Hazards Earth Syst. Sci.* 11, 1447–1462. <https://doi.org/10.5194/nhess-11-1447-2011>
- Miles, E., McCarthy, M., Dehecq, A., Kneib, M., Fugger, S., Pellicciotti, F., 2021. Health and sustainability of glaciers in High Mountain Asia. *Nat Commun* 12, 2868. <https://doi.org/10.1038/s41467-021-23073-4>
- Miles, E.S., Steiner, J., Willis, I., Buri, P., Immerzeel, W.W., Chesnokova, A., Pellicciotti, F., 2017. Pond Dynamics and Supraglacial-Englacial Connectivity on Debris-Covered Lirung Glacier, Nepal. *Front. Earth Sci.* 5, 69. <https://doi.org/10.3389/feart.2017.00069>
- Miles, E.S., Watson, C.S., Brun, F., Berthier, E., Esteves, M., Quincey, D.J., Miles, K.E., Hubbard, B., Wagnon, P., 2018a. Glacial and geomorphic effects of a supraglacial lake drainage and outburst event, Everest region, Nepal Himalaya. *The Cryosphere* 12, 3891–3905. <https://doi.org/10.5194/tc-12-3891-2018>
- Miles, E.S., Willis, I., Buri, P., Steiner, J.F., Arnold, N.S., Pellicciotti, F., 2018b. Surface Pond Energy Absorption Across Four Himalayan Glaciers Accounts for 1/8 of Total Catchment Ice Loss. *Geophysical Research Letters* 45. <https://doi.org/10.1029/2018GL079678>
- Mool, P., 2002. Inventory of glaciers, glacial lakes, and glacial lake outburst floods: monitoring and early warning systems in the Hindu Kush-Himalayan Region, Bhutan. International Centre for Integrated

- Mountain Development, Mountain Environment and Natural Resources' Information Systems, Kathmandu, Nepal.
- Nanni, U., Scherler, D., Ayoub, F., Millan, R., Herman, F., Avouac, J.-P., 2023. Climatic control on seasonal variations in mountain glacier surface velocity. *The Cryosphere* 17, 1567–1583. <https://doi.org/10.5194/tc-17-1567-2023>
- Narama, C., Daiyrov, M., Duishonakunov, M., Tadono, T., Sato, H., Kääb, A., Ukita, J., Abdrakhmatov, K., 2018. Large drainages from short-lived glacial lakes in the Teskey Range, Tien Shan Mountains, Central Asia. *Nat. Hazards Earth Syst. Sci.* 18, 983–995. <https://doi.org/10.5194/nhess-18-983-2018>
- Narama, C., Daiyrov, M., Tadono, T., Yamamoto, M., Kääb, A., Morita, R., Ukita, J., 2017. Seasonal drainage of supraglacial lakes on debris-covered glaciers in the Tien Shan Mountains, Central Asia. *Geomorphology* 286, 133–142. <https://doi.org/10.1016/j.geomorph.2017.03.002>
- Nie, Y., Liu, Q., Wang, J., Zhang, Y., Sheng, Y., Liu, S., 2018. An inventory of historical glacial lake outburst floods in the Himalayas based on remote sensing observations and geomorphological analysis. *Geomorphology* 308, 91–106. <https://doi.org/10.1016/j.geomorph.2018.02.002>
- Nuth, C., Kääb, A., 2011. Co-registration and bias corrections of satellite elevation data sets for quantifying glacier thickness change. *The Cryosphere* 5, 271–290. <https://doi.org/10.5194/tc-5-271-2011>
- Otsu, N., 1979. A Threshold Selection Method from Gray-Level Histograms. *IEEE Trans. Syst., Man, Cybern.* 9, 62–66. <https://doi.org/10.1109/TSMC.1979.4310076>
- Pohl, E., Knoche, M., Gloaguen, R., Andermann, C., Krause, P., 2014. The hydrological cycle in the high Pamir Mountains: how temperature and seasonal precipitation distribution influence stream flow in the Gunt catchment, Tajikistan. <https://doi.org/10.5194/esurfd-2-1155-2014>
- RGI Consortium, 2023. Randolph Glacier Inventory - A Dataset of Global Glacier Outlines, Version 7. <https://doi.org/10.5067/F6JMOVY5NAVZ>
- Richardson, S.D., Reynolds, J.M., 2000. An overview of glacial hazards in the Himalayas. *Quaternary International* 65–66, 31–47. [https://doi.org/10.1016/S1040-6182\(99\)00035-X](https://doi.org/10.1016/S1040-6182(99)00035-X)
- Rounce, D.R., Byers, A.C., Byers, E.A., McKinney, D.C., 2017. Brief communication: Observations of a glacier outburst flood from Lhotse Glacier, Everest area, Nepal. *The Cryosphere* 11, 443–449. <https://doi.org/10.5194/tc-11-443-2017>
- Safarov, M., Kang, S., Fazylov, A., Gulayozov, M., Banerjee, A., Navruzshoev, H., Chen, P., Xue, Y., Murodov, M., 2024. Estimating glacier dynamics and supraglacial lakes together with associated regional hazards using high-resolution datasets in Pamir. *J. Mt. Sci.* <https://doi.org/10.1007/s11629-024-8936-x>
- Safarov, M.S., Fazylov, A.R., 2023. Remote sensing and monitoring of mudflow-prone areas in the mountainous territories of Tajikistan. Promexpo, Dushanbe, Tajikistan.
- Sattar, A., Allen, S., Mergili, M., Haeberli, W., Frey, H., Kulkarni, A.V., Haritashya, U.K., Huggel, C., Goswami, A., Ramsankaran, R., 2023. Modeling Potential Glacial Lake Outburst Flood Process

- Chains and Effects From Artificial Lake-Level Lowering at Gepang Gath Lake, Indian Himalaya. *JGR Earth Surface* 128, e2022JF006826. <https://doi.org/10.1029/2022JF006826>
- Shafiev, G.V., 2018. Analysis of the state of outburst lakes along the Gunt River valley in the South-Western Pamirs. *Debris Flows: Disasters, Risk, Forecast, Protection*.
- Shean, D.E., Alexandrov, O., Moratto, Z.M., Smith, B.E., Joughin, I.R., Porter, C., Morin, P., 2016. An automated, open-source pipeline for mass production of digital elevation models (DEMs) from very-high-resolution commercial stereo satellite imagery. *ISPRS Journal of Photogrammetry and Remote Sensing* 116, 101–117. <https://doi.org/10.1016/j.isprsjprs.2016.03.012>
- Shean, D.E., Bhushan, S., Montesano, P., Rounce, D.R., Arendt, A., Osmanoglu, B., 2020. A Systematic, Regional Assessment of High Mountain Asia Glacier Mass Balance. *Front. Earth Sci.* 7, 363. <https://doi.org/10.3389/feart.2019.00363>
- Shugar, D.H., Burr, A., Haritashya, U.K., Kargel, J.S., Watson, C.S., Kennedy, M.C., Bevington, A.R., Betts, R.A., Harrison, S., Strattman, K., 2020. Rapid worldwide growth of glacial lakes since 1990. *Nat. Clim. Chang.* 10, 939–945. <https://doi.org/10.1038/s41558-020-0855-4>
- Smith, P.J., Brown, S., Dugar, S., 2017. Community-based early warning systems for flood risk mitigation in Nepal. *Nat. Hazards Earth Syst. Sci.* 17, 423–437. <https://doi.org/10.5194/nhess-17-423-2017>
- Strozzi, T., Luckman, A., Murray, T., Wegmuller, U., Werner, C.L., 2002. Glacier motion estimation using SAR offset-tracking procedures. *IEEE Trans. Geosci. Remote Sensing* 40, 2384–2391. <https://doi.org/10.1109/TGRS.2002.805079>
- Taylor, C., Robinson, T.R., Dunning, S., Rachel Carr, J., Westoby, M., 2023. Glacial lake outburst floods threaten millions globally. *Nat Commun* 14, 487. <https://doi.org/10.1038/s41467-023-36033-x>
- Thompson, I., Shrestha, M., Chhetri, N., Agusdinata, D.B., 2020. An institutional analysis of glacial floods and disaster risk management in the Nepal Himalaya. *International Journal of Disaster Risk Reduction* 47, 101567. <https://doi.org/10.1016/j.ijdrr.2020.101567>
- Thompson, S.S., Benn, D.I., Dennis, K., Luckman, A., 2012. A rapidly growing moraine-dammed glacial lake on Ngozumpa Glacier, Nepal. *Geomorphology* 145–146, 1–11. <https://doi.org/10.1016/j.geomorph.2011.08.015>
- Tomczyk, A.M., Ewertowski, M.W., Carrivick, J.L., 2020. Geomorphological impacts of a glacier lake outburst flood in the high arctic Zackenberg River, NE Greenland. *Journal of Hydrology* 591, 125300. <https://doi.org/10.1016/j.jhydrol.2020.125300>
- Vale, A.B., Arnold, N.S., Rees, W.G., Lea, J.M., 2021. Remote Detection of Surge-Related Glacier Terminus Change across High Mountain Asia. *Remote Sensing* 13, 1309. <https://doi.org/10.3390/rs13071309>
- Veh, G., Korup, O., Roessner, S., Walz, A., 2018. Detecting Himalayan glacial lake outburst floods from Landsat time series. *Remote Sensing of Environment* 207, 84–97. <https://doi.org/10.1016/j.rse.2017.12.025>

- Veh, G., Lützow, N., Kharlamova, V., Petrakov, D., Hugonnet, R., Korup, O., 2022. Trends, Breaks, and Biases in the Frequency of Reported Glacier Lake Outburst Floods. *Earth's Future* 10, e2021EF002426. <https://doi.org/10.1029/2021EF002426>
- Vuichard, D., Zimmermann, M., 1987. The 1985 Catastrophic Drainage of a Moraine-Dammed Lake, Khumbu Himal, Nepal: Cause and Consequences. *Mountain Research and Development* 7, 91. <https://doi.org/10.2307/3673305>
- Wang, S., Zhou, L., 2017. Glacial Lake Outburst Flood Disasters and Integrated Risk Management in China. *Int J Disaster Risk Sci* 8, 493–497. <https://doi.org/10.1007/s13753-017-0152-7>
- Wang, X., Guo, X., Yang, C., Liu, Q., Wei, J., Zhang, Yong, Liu, S., Zhang, Yanlin, Jiang, Z., Tang, Z., 2020. Glacial lake inventory of high-mountain Asia in 1990 and 2018 derived from Landsat images. *Earth Syst. Sci. Data* 12, 2169–2182. <https://doi.org/10.5194/essd-12-2169-2020>
- Wangchuk, S., Bolch, T., 2020. Mapping of glacial lakes using Sentinel-1 and Sentinel-2 data and a random forest classifier: Strengths and challenges. *Science of Remote Sensing* 2, 100008. <https://doi.org/10.1016/j.srs.2020.100008>
- Watson, C.S., Quincey, D.J., Carrivick, J.L., Smith, M.W., Rowan, A.V., Richardson, R., 2017. Heterogeneous water storage and thermal regime of supraglacial ponds on debris-covered glaciers. *Earth Surf Processes Landf* 43, 229–241. <https://doi.org/10.1002/esp.4236>
- Westoby, M.J., Glasser, N.F., Brasington, J., Hambrey, M.J., Quincey, D.J., Reynolds, J.M., 2014. Modelling outburst floods from moraine-dammed glacial lakes. *Earth-Science Reviews* 134, 137–159. <https://doi.org/10.1016/j.earscirev.2014.03.009>
- Williams, M.W., Konovalov, V.G., 2008. Central Asia Temperature and Precipitation Data, 1879-2003, Version 1. <https://doi.org/10.7265/N5NK3BZ8>
- Wilson, R., Glasser, N.F., Reynolds, J.M., Harrison, S., Anaconda, P.I., Schaefer, M., Shannon, S., 2018. Glacial lakes of the Central and Patagonian Andes. *Global and Planetary Change* 162, 275–291. <https://doi.org/10.1016/j.gloplacha.2018.01.004>
- Xie, Z., ShangGuan, D., Zhang, S., Ding, Y., Liu, S., 2013. Index for hazard of Glacier Lake Outburst flood of Lake Merzbacher by satellite-based monitoring of lake area and ice cover. *Global and Planetary Change* 107, 229–237. <https://doi.org/10.1016/j.gloplacha.2012.05.025>
- Yao, X., Liu, S., Han, L., Sun, M., Zhao, L., 2018. Definition and classification system of glacial lake for inventory and hazards study. *J. Geogr. Sci.* 28, 193–205. <https://doi.org/10.1007/s11442-018-1467-z>
- Zafar, A., Uchimura, T., 2023. The July 2015 Debris flow in Barsem, Western Pamir (GBAO) Tajikistan: Description and causes. *E3S Web of Conf.* 415, 03003. <https://doi.org/10.1051/e3sconf/202341503003>
- Zaginaev, V., Petrakov, D., Erokhin, S., Meleshko, A., Stoffel, M., Ballesteros-Cánovas, J.A., 2019. Geomorphic control on regional glacier lake outburst flood and debris flow activity over northern Tien Shan. *Global and Planetary Change* 176, 50–59. <https://doi.org/10.1016/j.gloplacha.2019.03.003>

- Zhang, G., Yao, T., Xie, H., Wang, W., Yang, W., 2015. An inventory of glacial lakes in the Third Pole region and their changes in response to global warming. *Global and Planetary Change* 131, 148–157. <https://doi.org/10.1016/j.gloplacha.2015.05.013>
- Zhang, M., Chen, F., Guo, H., Yi, L., Zeng, J., Li, B., 2022. Glacial Lake Area Changes in High Mountain Asia during 1990–2020 Using Satellite Remote Sensing. *Research* 2022, 2022/9821275. <https://doi.org/10.34133/2022/9821275>
- Zhang, Q., Kang, S., 2017. Glacier snowline altitude variations in the Pamirs, Tajikistan, 1998-2013: insights from remote sensing images. *Remote Sensing Letters* 8, 1220–1229. <https://doi.org/10.1080/2150704X.2017.1375611>
- Zheng, G., Allen, S.K., Bao, A., Ballesteros-Cánovas, J.A., Huss, M., Zhang, G., Li, J., Yuan, Y., Jiang, L., Yu, T., Chen, W., Stoffel, M., 2021. Increasing risk of glacial lake outburst floods from future Third Pole deglaciation. *Nat. Clim. Chang.* 11, 411–417. <https://doi.org/10.1038/s41558-021-01028-3>
- Zheng, G., Bao, A., Li, J., Zhang, G., Xie, H., Guo, H., Jiang, L., Chen, T., Chang, C., Chen, W., 2019. Sustained growth of high mountain lakes in the headwaters of the Syr Darya River, Central Asia. *Global and Planetary Change* 176, 84–99. <https://doi.org/10.1016/j.gloplacha.2019.03.004>
- Zhu, M., Yao, T., Xie, Y., Xu, B., Yang, W., Yang, S., 2020. Mass balance of Muji Glacier, northeastern Pamir, and its controlling climate factors. *Journal of Hydrology* 590, 125447. <https://doi.org/10.1016/j.jhydrol.2020.125447>

9. Appendices

9.1. Main raw data

Table 2. Total area and volume estimates for supraglacial ponds on Baralmos glacier (2017-2024)

Date	Total ponds area [m ²]	Total estimated volume [m ³]
29.06.2017	14058,00	53072,675
04.07.2017	14463,00	55106,261
06.07.2017	13284,00	45515,353
11.07.2017	12438,00	47465,770
21.07.2017	14904,00	57276,731
06.08.2017	14067,00	53289,339
08.08.2017	19215,00	74991,276
15.08.2017	16470,00	66186,349
16.08.2017	14670,00	58186,698
18.08.2017	16065,00	64200,619
19.08.2017	16020,00	63771,871
28.08.2017	14094,00	55124,532
31.08.2017	18189,00	76756,939
07.09.2017	15390,00	60474,724
09.09.2017	19692,00	84936,371
15.09.2017	19377,00	80696,407
21.09.2017	20061,00	85641,947
26.09.2017	17334,00	68803,407
28.09.2017	21483,00	88511,376
26.06.2018	16065,00	70414,472
30.06.2018	22581,00	107945,225
01.07.2018	28413,00	151585,039
06.07.2018	17145,00	73467,652
14.07.2018	17415,00	76634,703
18.07.2018	20754,00	95521,535
22.07.2018	21699,00	101285,153
23.07.2018	24237,00	118890,899
25.07.2018	22230,00	104743,656
03.08.2018	20889,00	94748,555
11.08.2018	20034,00	91134,057
12.08.2018	19656,00	89866,010
13.08.2018	20601,00	92849,679
16.08.2018	17343,00	74747,921
20.08.2018	20142,00	91065,636
27.08.2018	16893,00	71008,223
31.08.2018	16785,00	68924,372
01.09.2018	24489,00	116903,521
02.09.2018	27972,00	140615,500
03.09.2018	25200,00	125633,340
04.09.2018	30123,00	156033,319
05.09.2018	24912,00	119271,091

07.09.2018	22644,00	107926,492
08.09.2018	25479,00	125130,984
10.09.2018	25398,00	118202,405
28.06.2019	30186,00	133838,392
11.07.2019	37719,00	187405,988
18.07.2019	32094,00	162614,010
23.07.2019	30447,00	156812,070
26.07.2019	36873,00	196342,782
30.07.2019	25992,00	132153,260
08.08.2019	34740,00	187192,937
10.08.2019	31365,00	166208,165
11.08.2019	31923,00	166331,593
19.08.2019	31635,00	168610,887
22.08.2019	30924,00	163743,735
28.08.2019	34299,00	188929,793
29.08.2019	40725,00	235840,348
01.09.2019	35460,00	201581,782
02.09.2019	37827,00	207489,988
03.09.2019	37917,00	206672,983
04.09.2019	31860,00	168776,344
10.09.2019	25200,00	123733,942
21.09.2019	36549,00	200456,665
20.06.2020	33930,00	171927,212
21.06.2020	40464,00	227443,573
03.07.2020	46656,00	257929,999
07.07.2020	34704,00	194508,563
20.07.2020	40590,00	235762,545
25.07.2020	41949,00	243823,178
29.07.2020	61002,00	375847,942
05.08.2020	44406,00	267621,081
08.08.2020	39060,00	227932,520
17.08.2020	25776,00	109224,681
23.08.2020	23868,00	104557,842
02.09.2020	24345,00	105626,804
05.09.2020	25641,00	114586,785
07.09.2020	26685,00	121979,817
10.09.2020	32202,00	151117,407
13.09.2020	27792,00	119976,859
21.09.2020	29403,00	134722,003
22.09.2020	29556,00	136198,493
02.06.2021	16425,00	61258,165
06.06.2021	23715,00	98040,879
11.06.2021	34254,00	173725,708
18.06.2021	20322,00	78898,353
28.06.2021	27351,00	117156,772
03.07.2021	16200,00	76464,161
08.07.2021	39663,00	199145,690
09.07.2021	35271,00	182592,186

10.07.2021	38547,00	220277,701
11.07.2021	46655,00	268501,722
17.07.2021	29223,00	136561,609
24.07.2021	30870,00	145077,361
09.08.2021	31608,00	150760,627
11.08.2021	29862,00	132038,967
13.08.2021	28710,00	129897,253
17.08.2021	30672,00	145366,432
23.08.2021	28890,00	135928,746
06.09.2021	30213,00	141595,202
07.09.2021	30537,00	145267,993
08.09.2021	34164,00	166937,175
12.09.2021	29511,00	137575,417
13.09.2021	31509,00	151308,199
20.09.2021	31347,00	149700,072
25.09.2021	31095,00	150696,903
27.06.2022	38466,00	188041,430
03.07.2022	42039,00	219343,993
15.07.2022	38997,00	202788,559
17.07.2022	33255,00	169116,600
18.07.2022	40140,00	216328,864
19.07.2022	33975,00	179332,580
20.07.2022	38763,00	212294,443
21.07.2022	41796,00	232736,618
22.07.2022	43029,00	249364,412
23.07.2022	43893,00	264042,762
25.07.2022	47070,00	295295,096
26.07.2022	36675,00	189137,573
28.07.2022	29016,00	139712,143
07.08.2022	39348,00	209181,063
13.08.2022	41526,00	221954,398
19.08.2022	37017,00	191038,410
29.08.2022	36567,00	188342,665
07.09.2022	40770,00	213699,321
15.09.2022	35928,00	184155,896
23.09.2022	37224,00	195148,547
29.09.2022	28620,00	145116,521
11.06.2023	44343,00	251042,218
17.06.2023	39636,00	204780,050
18.06.2023	35316,00	178393,557
21.06.2023	43371,00	228648,615
23.06.2023	36144,00	182370,616
25.06.2023	39564,00	200652,161
01.07.2023	40482,00	211498,534
11.07.2023	47322,00	262481,959
14.07.2023	46458,00	267671,269
15.07.2023	48797,00	297428,680
19.07.2023	49437,00	310117,609

22.07.2023	41058,00	221050,444
03.08.2023	44937,00	253767,614
10.08.2023	49095,00	285642,254
15.08.2023	45234,00	258925,989
17.08.2023	45333,00	260660,626
18.08.2023	46413,00	264473,189
19.08.2023	47511,00	271881,915
20.08.2023	46773,00	274246,703
21.08.2023	43308,00	248143,235
29.08.2023	47952,00	273924,850
02.09.2023	45054,00	263194,365
06.09.2023	46494,00	275641,504
12.09.2023	43299,00	258859,249
14.09.2023	42453,00	251705,627
22.09.2023	45936,00	276837,133
27.09.2023	42129,00	245600,567
27.06.2024	62370,00	426222,610
03.07.2024	49653,00	297280,200
05.07.2024	48951,00	293200,850
07.07.2024	47394,00	282984,090
17.07.2024	52749,00	320411,360
27.07.2024	52803,00	317556,720
28.07.2024	53280,00	321496,800
05.08.2024	56295,00	350035,640
08.08.2024	54567,00	330013,080
14.08.2024	52659,00	317456,420
25.08.2024	59310,00	372858,820
27.08.2024	56187,00	351764,110
31.08.2024	59004,00	370105,040
02.09.2024	53478,00	330045,300
06.09.2024	52407,00	322918,710
13.09.2024	53325,00	336467,170
22.09.2024	51480,00	321590,120
24.09.2024	53748,00	335499,740

Table 3. Total area and volume estimates for supraglacial ponds on Kyzylsu glacier (2023-2024)

Date	Total ponds area [m ²]	Total estimated volume [m ³]
06.11.2023	43587,0	362904,393
19.06.2023	7146,0	19799,389
21.06.2023	7911,0	26726,457
27.06.2023	7884,0	26726,457
11.07.2023	936,0	2071,008
19.07.2023	2484,0	5127,820
15.08.2023	1080,0	1477,422
21.08.2023	360,0	548,743
22.05.2024	24053,3	151007,197

13.06.2024	30636,0	253431,550
15.06.2024	36684,0	297583,094
25.06.2024	7710,9	29657,684
28.07.2024	4536,0	14439,149
08.08.2024	2475,0	8001,620
26.08.2024	2592,0	8532,200
30.08.2024	2889,0	9737,160
03.09.2024	2826,0	9621,387

Table 4. Area estimates for supraglacial ponds on Baralmos glacier for historical period

Date	Total ponds area [m ²]
20.08.1993	171900,00
21.09.1993	128700,00
23.08.1994	114300,00
02.10.1997	166500,00
02.08.1998	147600,00
03.09.1998	12359,72
05.08.2002	3628,81
13.08.2008	41123,00
04.09.2010	33506,00
26.07.2013	30321,00
16.07.2015	9825,78

For every year, the following charts—which were not included in the main text—will be shown.

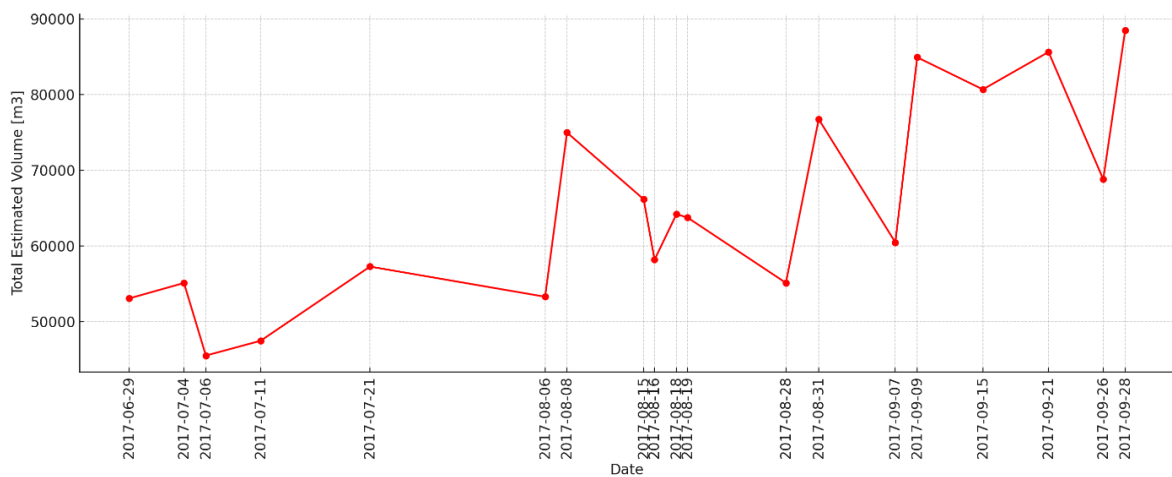


Figure 49. Total pond volumes over time (2017) based on a formula from Watson et al., 2017.

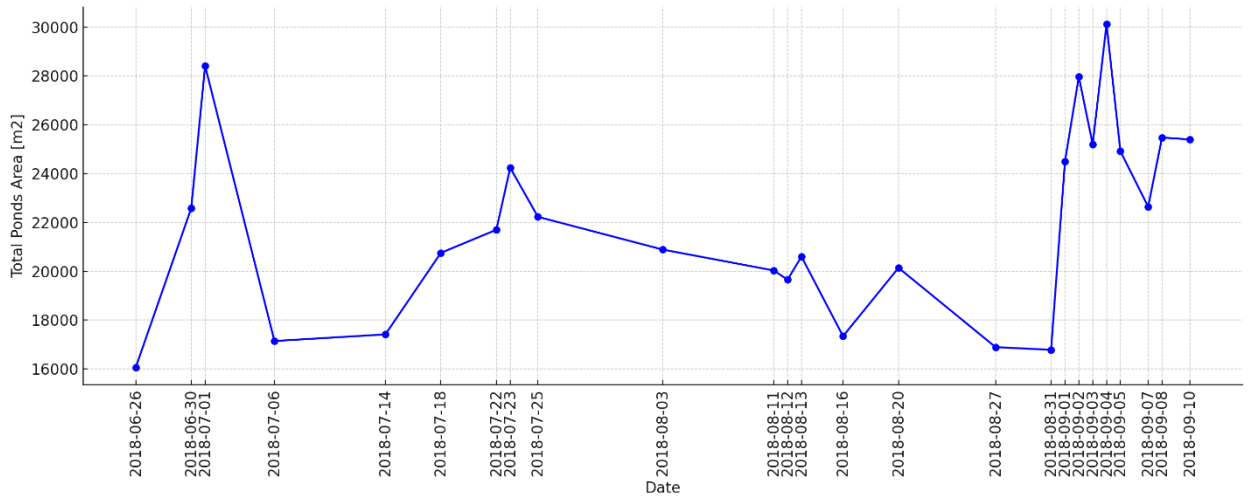


Figure 50. Total pond areas over time (2018).

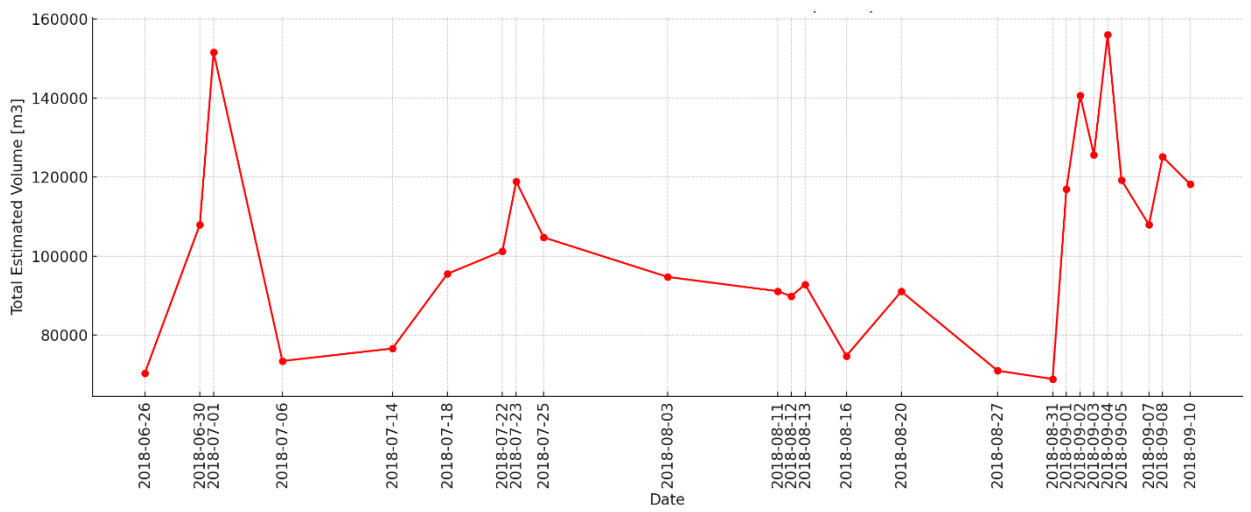


Figure 51. Total pond volumes over time (2018) based on a formula from Watson et al., 2017.

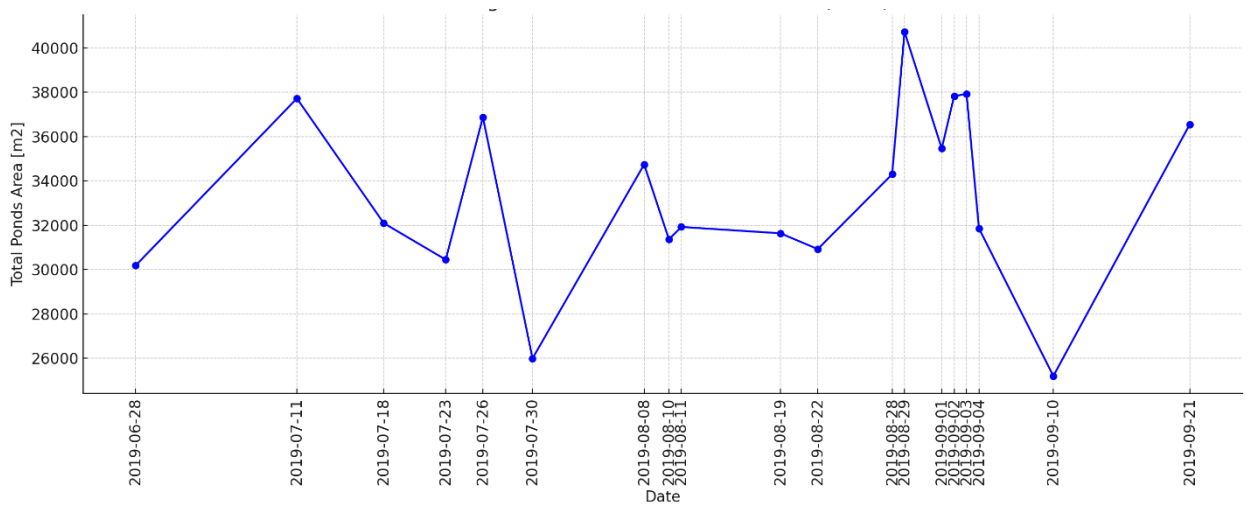


Figure 52. Total pond areas over time (2019).

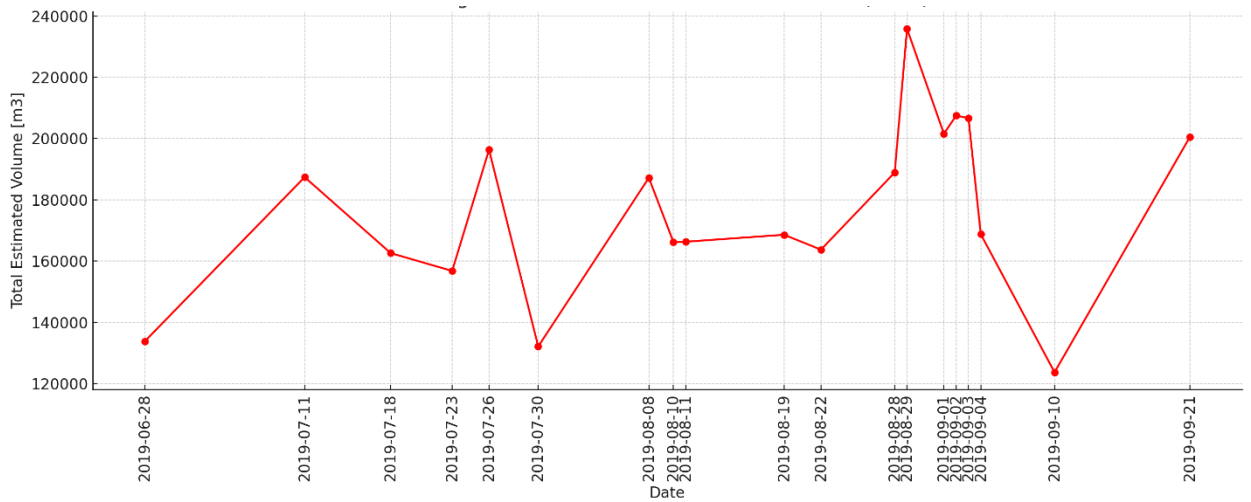


Figure 53. Total pond volumes over time (2019) based on a formula from Watson et al., 2017.

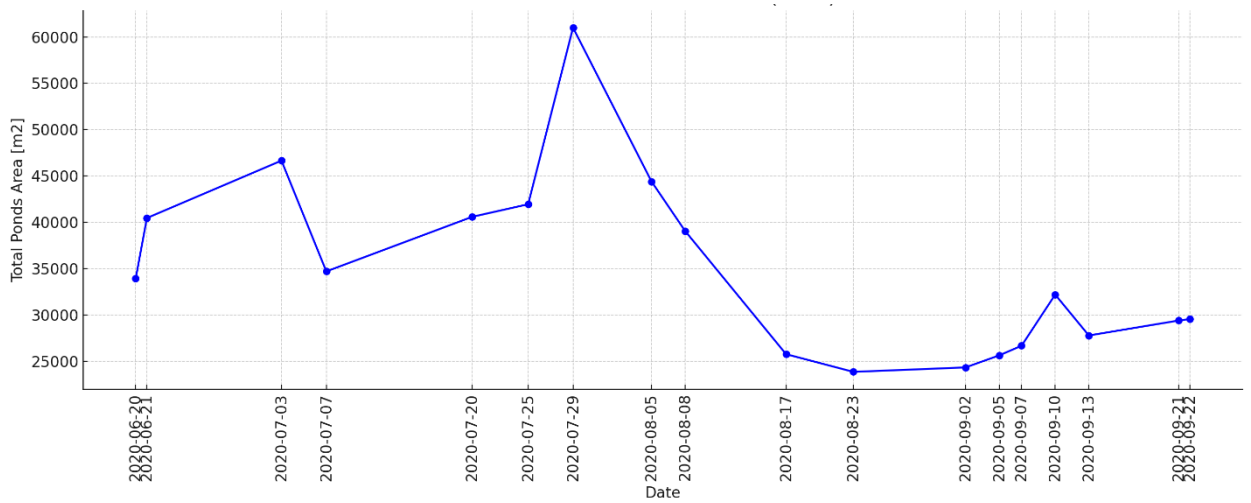


Figure 54. Total pond areas over time (2020).

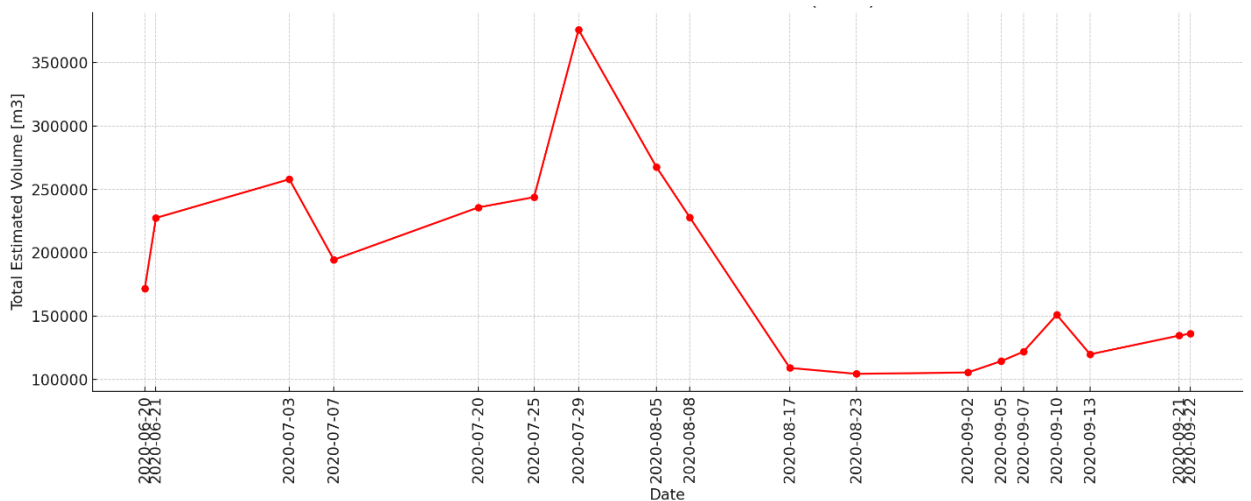


Figure 55. Total pond volumes over time (2020) based on a formula from Watson et al., 2017.

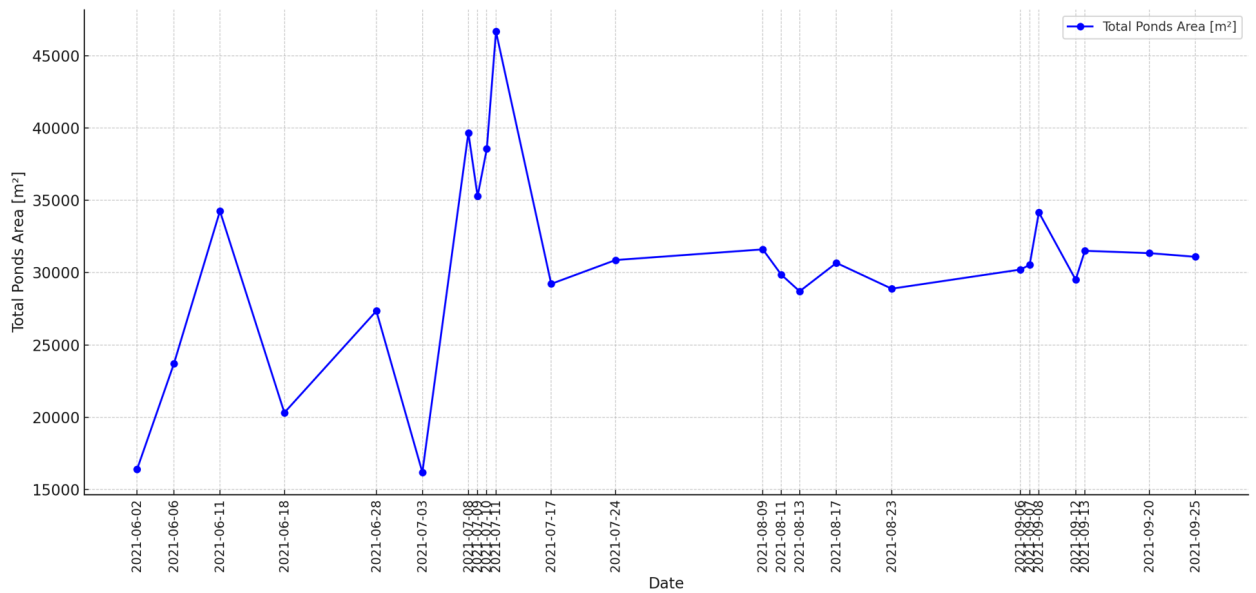


Figure 56. Total pond areas over time (2021).

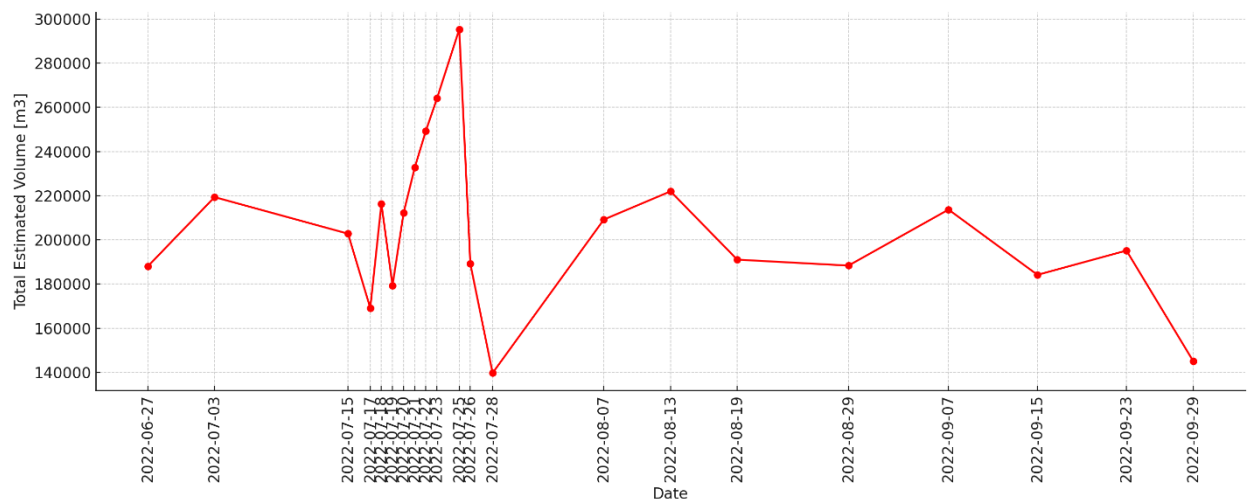


Figure 57. Total pond volumes over time (2022) based on a formula from Watson et al., 2017.

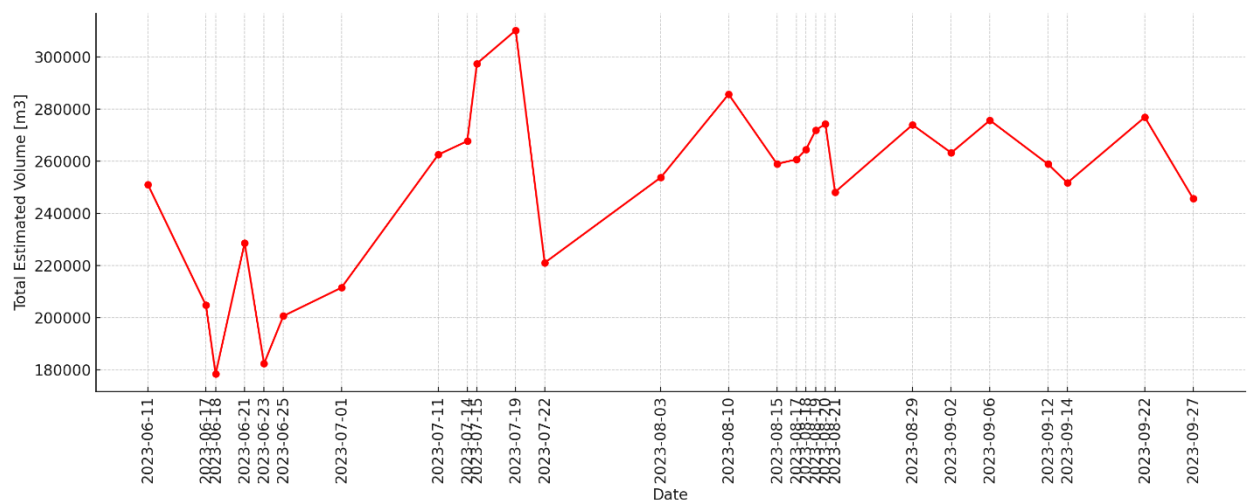


Figure 58. Total pond volumes over time (2023) based on a formula from Watson et al., 2017.

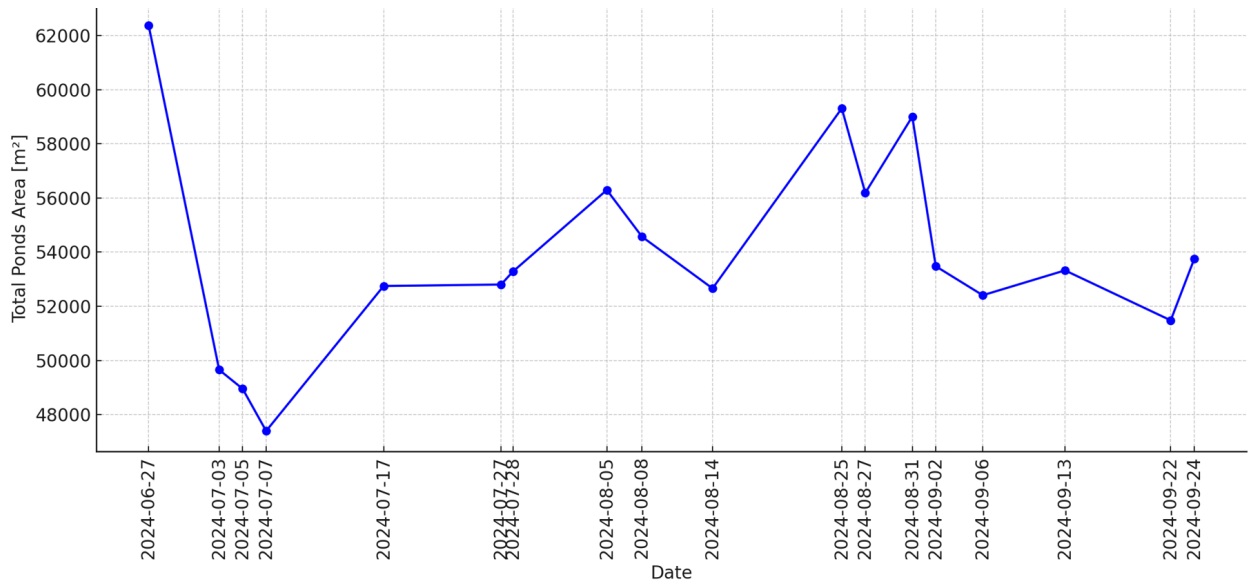


Figure 59. Total pond areas over time (2024).

Personal declaration

I hereby declare that the submitted thesis is the result of my own, independent work. All external sources are explicitly acknowledged in the thesis.

Zurich, 31st of January 2025

A handwritten signature in blue ink, appearing to read 'B. Kapur', is written over a faint, light blue rectangular stamp.